Imperial College, Department of Bioengineering
Neural Coding Laboratory

Two-photon minimal inertia scanning patterns for fast acquisition of calcium dynamics

Renaud Schuck

Submitted in part fulfilment of the requirements for the degree of
Doctor of Philosophy in Bioengineering and
the Diploma of Imperial College, January 2017

Declaration

I herewith certify that all the material in this thesis is my own work, except for quotations from published and unpublished sources which are clearly indicated and acknowledged as such. The source of any picture, diagram or other figure that is not my own work is also indicated. The copyright of this thesis rests with the author and is made available under a Creative Commons Attribution Non-Commercial No Derivatives licence. Researchers are free to copy, distribute or transmit the thesis on the condition that they attribute it, that they do not use it for commercial purposes and that they do not alter, transform or build upon it. For any reuse or redistribution, researchers must make clear to others the licence terms of this work.

Renaud Schuck

January 2017

Abstract

Development of optical technologies aiming to reverse engineer neural circuits has been flourishing over the past two decades. Multi-Photon Laser Scanning Microscopy (MPLMS) together with the development of fast kinetic fluorescent calcium dyes has revolutionised the world of modern neuroscience. This technology enables mesoscale functional imaging in deep scattering brain tissues of large two (2D) and three dimensional (3D) neural networks. With single cell sensitivity *in vitro* as well as *in vivo*, it is one of the main contenders for deciphering higher brain functions. My approach in this thesis is to develop and test new scanning techniques for fast functional calcium imaging aiming to enhance the temporal precision of the acquisition. To avoid the slow and sequential "point" raster scanning nature of these Galvanometric Scanners (GSs) based microscopes, I developed new 2D and 3D scanning algorithms. These algorithms were developed in MATLAB with a simulation platform that models the main mechanical elements of the MPLSM. Both my 2D Adaptive Spiral Scanning (SSA) algorithm and my 3D Orbital Scanning Trajectory (OST) algorithm were developed to minimize the inertial slowdowns of the GSs and Electrical Tunable Lens (ETL) and therefore increase the temporal resolution of the acquisition. In 2D, I tested the SSA algorithm on *in vitro* hippocampal brain slices loaded with the synthetic calcium dye Cal520. To assess the performance of the scanning technique, I used the Cramér-Rao Bound (CRB) as a metric for signal quality. The CRB estimates the time of occurrence of an Action Potential (AP) from the calcium imaging data, taking into account the sampling frequency and the SNR of the acquisition. In this thesis, I show that the use of scanning strategies enables sampling rates one order of magnitude higher than traditional frame scanning in functional calcium imaging. I also show that frame scanning needs considerably higher SNR values than scanning strategies to reach the same temporal precision. In 3D, I implemented the scanning algorithms into the software and hardware of the MPLSM and recorded the trajectory of the focal point with a high-speed camera as a proof of principle. More analyses regarding the precision of the paths needs to be carried out in 3D for functional calcium imaging *in vitro* or *in vivo*. These software-based scanning strategies are attractive as they are inexpensive, easily transferable from one setup to another and enable fast functional calcium imaging with standard commercial MPSLMs. Finally, through this implementation of scanning strategies, I recorded multiple data sets of spontaneous and evoked activity in populations of Dentate

Granular Cells (DGCs). This lead to the new beginning of a larger *in vitro* investigation at the microcircuit level on the functionality of the DG.

Acknowledgements

First, I would like to thank my supervisor Simon Schultz for giving me the opportunity of doing a PhD in his Lab. I would like to thanks him also for his help, support and confidence in me.

A special thank goes to Stefania Garasto for all her support and kindness. Stefania, you are truly a wonderful person - I would like to thank you for all your help, for all the good conversations we had and for being an amazing friend and a very comprehensive flatmate.

Thanks to Luca Annecchino for introducing me to all the tricks of the Scientifica scope. I would also like to thank him for his friendship and for always reminding me that we need to go to Oktoberfest.

Thanks to Osh Agabi for teaching me how to do brain slices and how to use the "Jedi" rig.

Thanks Peter Quicke for his sharpness and all his help in optics.

Thanks to Ann Go for being so patient and spending long hours helping me and teaching me the patch clamp technique.

Thanks to Amanda Foust for her guidance and knowledge and for always taking time to listen to the many questions and problems that a PhD student can encounter.

Thanks to Caroline Copeland for her supervision and her help on any animal issues.

Thanks to S. Chakraborty, M. Tolkiehn, S. Mitolo, T. Muzzu and all the people in the Schultz, Claupath and Chadderton Labs for building a wonderful atmosphere.

A spacial thanks goes to all the NETT fellows for being such a friendly team.

Last, but not least, I would like to thank my family, my mother Pascale my father Peter my brother Alex , and my close friends for all they did for me.

Dedication

I would like to dedicate this theses to my parents.

‘Genius is one percent inspiration, ninety nine percent perspiration.’

Thomas Edison

Contents

Page

Contents **i**

Abstract **iii**

Acknowledgements **v**

List of Tables **xiii**

List of Figures **xvi**

List of Abbreviations **xvii**

1 Introduction **1**

1.1 Motivation 1

1.2 Introduction to two-photon microscopy 4

1.3 Scanning neural circuits with a commercial two photon microscope 6

1.3.1 Galvanometric scanner for MPLSM 6

1.3.2 Raster scanning 7

1.3.3 Two-dimensional scanning strategies 10

1.3.4 Three-dimensional scanning with MPLSM 11

1.4 Fast functional calcium imaging and its limitation 12

1.4.1 Calcium dyes for MPLSM functional imaging 13

1.4.2 Fast functional calcium imaging in slices 15

1.4.3 Limitations of Calcium imaging 17

1.4.4 Recent progress with customised two-photon microscopes 18

1.5 Cell culture micro-environment design 19

1.6 Introduction to the dentate gyrus 20

1.6.1 Structure of the dentate gyrus 21

1.6.2 Functionalities of the dentate gyrus 23

1.7 Publications 28

2 Simulation platform for 2D scanning strategies: the SSA algorithm 29

2.1 Abstract 29
2.2 Introduction 30
2.3 Material and methods 31
2.3.1 GS mechanical model 31
2.3.2 Simulation of populations of neuronal calcium signals 34
2.4 Results 34
2.4.1 The SSA algorithm 36
2.4.2 Signal Acquisition 38
2.5 Discussion 39
2.6 Acknowledgements 39
2.7 Future work 40

3 Fast functional calcium imaging with 2D scanning strategies 41

3.1 Abstract 41
3.2 Introduction 42
3.3 Material and methods 44
3.3.1 Path generation for targeted scanning strategies 44
3.3.2 In-vitro cell loading of hippocampal slices with calcium indicator dyes 47
3.3.3 Two-photon imaging and electrophysiology 48
3.3.4 Assessing the quality of scanned signals 48
3.4 RESULTS 50
3.4.1 Minimal inertia scanning paths enable fast and precise functional calcium imaging 50
3.4.2 Signal quality 55
3.5 Discussion 62
3.6 Appendix 1: Cramer Rao bound for spike detection from calcium imaging data 64
3.6.1 Signal model 64
3.6.2 Cramer-Rao bound calculation 65

4 Introduction to 3D scanning strategies 67

4.1 Abstract 67
4.2 Introduction 68
4.3 Materials and methods 68
4.3.1 ETL Model 68

4.3.2 Scanning and neural population model 70
4.4 Results 71
4.4.1 SSA algorithm extension for 3D scanning 72
4.4.2 Sampling frequency and calcium transient acquisition 74
4.5 Discussion 76
4.6 Acknowledgement 76
4.7 Future work: 3D scanning strategies experimental validation 77

5 Functional calcium imaging of dentate granular cells in slices 82
5.1 Spontaneous activity of hippocampal granular cells 83
5.1.1 Juvenile wild type mice 83
5.1.2 Adult wild type mice 84
5.2 Pattern separations in hippocampal granular cells 87
5.3 Appendix: Hydrogel photolithography with MPLSM 91
5.3.1 Photo-patterning effect 92
5.3.2 Photo-degradation effect 94

6 Conclusion and future directions 99
6.1 Summary of thesis achievements 99
6.2 Future directions 100

Bibliography 103

List of Tables

2.1 Estimated galvanometer parameters 33

4.1 Fitted parameters for our model of the ETL step response function 69

List of Figures

1.1 Patch clamp technique 2
1.2 Fluorescent microscopes 3
1.3 Two-photon technique 5
1.4 Galvanometric Scanners 6215H Cambridge technology 7
1.5 Raster Scanning with Galvanometric MPLSM 8
1.6 Schematic and positioning of the hippocampus in the mouse brain 21
1.7 Structure of the Dentate Gyrus 24
1.8 Structural MPLSM images of GCs 25

2.1 Mechanical characterization of the GS 32
2.2 Step response of the Cambridge Technology Model 6215H Galvanometric Scanners 33
2.3 The GS model block diagram 34
2.4 Neural ensemble simulation underlying the system model 35
2.5 Improved fit of spiral trajectories through a pseudo-random population of neurons 35
2.6 Sampling frequencies and useful signal ratio α achieved by the SSA algorithm 36
2.7 Acquisition matrix for a 5 neuron population 38
2.8 Recorded fluorescence ($\Delta F/F$) from a simulated excitatory neuron 38

3.1 Spiral scanning yields lower cellular miss rates, but travelling salesperson scanning higher SNRs, for the same somatic locations. 51
3.2 Sampling frequency and dwell time achievable for the TSS and SSA algorithms. 53
3.3 Scanning patterns for fast acquisition of calcium signals. 54
3.4 High sampling rates in TSS lead to ROI dropping. 56
3.5 Photon collection with TSS. 57

3.6 Simultaneous functional calcium imaging and ground truth electrophysiology recordings for raster scanning and scanning strategies 60
3.7 Uncertainty in timing of reconstructed action potentials depends on both SNR and sampling frequency 61

4.1 ETL linear axial shift 69
4.2 ETL step response fitting model 70
4.3 An example beam path from our SSA algorithm applied to GFP labelled neurons 71
4.4 3D Scanning model block diagram 72
4.5 Two examples of 3D MPLSM scanning strategies on pseudo-random population of neurons 72
4.6 3D SSA allows the sampling of high number of neurons 75
4.7 Two-photon focal spot in fluorescein 78
4.8 3D two-photon focal spot imaging 79
4.9 3D cylinder scanning strategy position assessment 80
4.10 3D orbital scanning strategy position assessment 81

5.1 Horizontal hippocampal mouse brain slice schematic 83
5.2 Spontaneous activity of DG granular cells in juvenile wild-type mice 85
5.3 Spontaneous activity of Dentate Gyrus granular cells in adult wild-type mice . 88
5.4 Evoked activity of Dentate Gyrus granular cells in Juvenile wild-type mice . 89
5.5 Hydrogel two-photon photo-patterning process 93
5.6 Horizontal photo-patterning profile in hydrogel obtained with an MPLSM . . 94
5.7 MPLSM hydrogel photo-degradation process 96
5.8 Hydrogel MPLSM time dependent photo-degradation process 97
5.9 Arbitrary line MPLSM photo-degradation process 98

List of Abbreviations

ACSF Artificial Cerebro-Spinal Fluid

AOD Acousto-Optical-Deflectors

AP Action Potential

CA1 Cornu Ammonis 1

CA3 Cornu Ammonis 3

CLSM Confocal Laser Scanning Microscopy

CRB Cramer Rao Bound

CSF Cellular Sampling Frequency

CST Cylindrical Scanning Trajectory

DG Dentate Gyrus

DGCs Dentate Granular Cells

EAP Electrical Action Potential

ETL Electrical Tunable Lens

FOV Field Of View

GCs Granular Cells

GECI Genetically Encoded Calcium Indicator

GFP Green Fluorescent Protein

GS Galvanometric Scanner

HOPS Heuristically Optimal Path Scanning

LFP Local Field Potential

MEA Multi Electrode Array

ML Molecular Layer

MPLSM Multi-Photon Laser Scanning Microscopy

NA Numerical Aperture

ODE Ordinary Differential Equation

OST Orbital Scanning Trajectory

PEG Polyethylene Glycol

PMT Photo-Multiplier Tube

PND Post Natal Day

PP Perforant Path

PSF Point Spread Function

RGS Resonant Galvanometric Scanner

ROIs Region Of Interests

SNR Signal to Noise Ratio

SOI Segment Of Interest

SSA Adaptive Spiral Scanning

TPS Targeted Path Scanning

TSA Travelling Salesman Algorithm

XGS X axis Galvanometric Scanner

YGS Y axis Galvanometric Scanner

Chapter 1

Introduction

1.1 Motivation

After two years studying for a Masters in Bioengineering in PHELMA in France, I decided to specialize in Neuroscience. Hence, I finished my engineering degree abroad in Germany at the Technical University in Munich where I took specific lectures that gave me an overview of the challenges in different research areas in Neuroscience. Trained as an engineer, my interest went towards the tools that can help us understand how the brain works. In the field of technology available to record and stimulate neural networks, the main criteria that defines the performances of a technique are: How invasive the procedure is, the number of simultaneously recorded/stimulated cells, the signal to noise ratio of the acquisition and the spatial and temporal resolution of the acquisition/stimulation. In modern neuroscience, the precise acquisitions of spike trains, composed of Action Potentials (APs), in single neuron and neuron populations were mainly made using the following techniques: Patch clamp, Multielectrode array/Optrodes, confocal and multiphoton microscopy.

The patch clamp technique utilizes a glass micro-pipette, a microelectrode and a solution, the composition of which can be modified depending upon intended use. Two main modes are available: the 'cell-attached' mode (containing recovery Artificial Cerebro-Spinal

Fluid (rACSF)) and the 'whole cell' mode (containing a solution matching the intracellular ion composition of a neuron) see Fig.1.1 *A* and *B*. The first one applies a suction force at the tip of the glass micropipette to seal to the cell membrane, and is mostly used to enable the recording of single ion channel currents from the membrane over which the seal is formed. The 'whole cell' recording technique penetrates the cell by applying more suction and enables the user to monitor and control every change in the membrane voltage of the patched cell with high temporal resolution. However, it only permits the user to record or stimulate one cell at a time in the entire network. The number of achievable simultaneous cell patchings has risen over the years (current record: 8 neurons) due to advancements in both hardware and software [Wang et al., 2015].

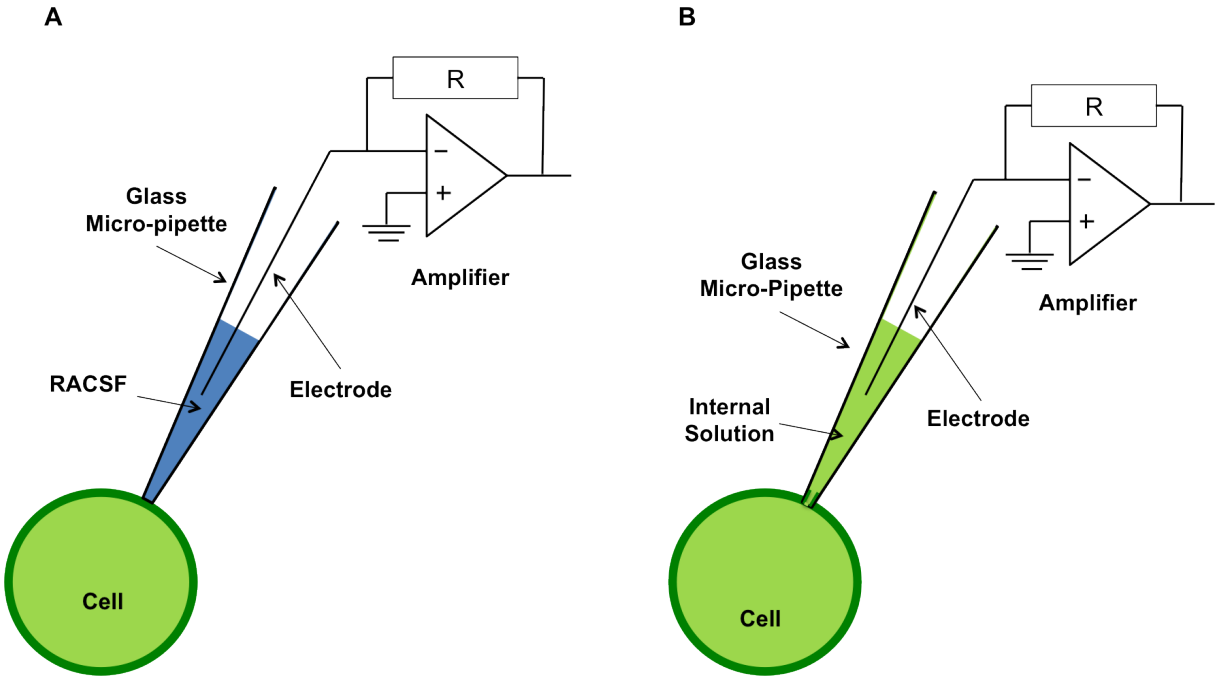


Figure 1.1: Patch clamp technique. *A* The cell-attached method. The glass micro-pipette is sealed to the cell membrane. *B* The whole cell patch clamp. The glass micro-pipette penetrates the cell.

The possibility of recording from and stimulating neural cells at a microscopic level from a large population of neurons can be achieved with Micro-Electrode Arrays (MEAs) [Obien et al., 2014] and the more recent optrode technology combining optogenetic and multi-site microelectrodes [Son et al., 2015, Welkenhuysen et al., 2016]. Both techniques

enable local neural stimulation and the recordings of Local Field Potentials (LFPs) and single neuron Electrical Action Potentials (EAPs) (with the use of spike sorting algorithms). The two major improvements to the optrode over a simple MEA is that the spatial resolution of the stimulation is considerably increased and that there is no electrical artifact (whilst stimulating) in the neural signal acquisition.

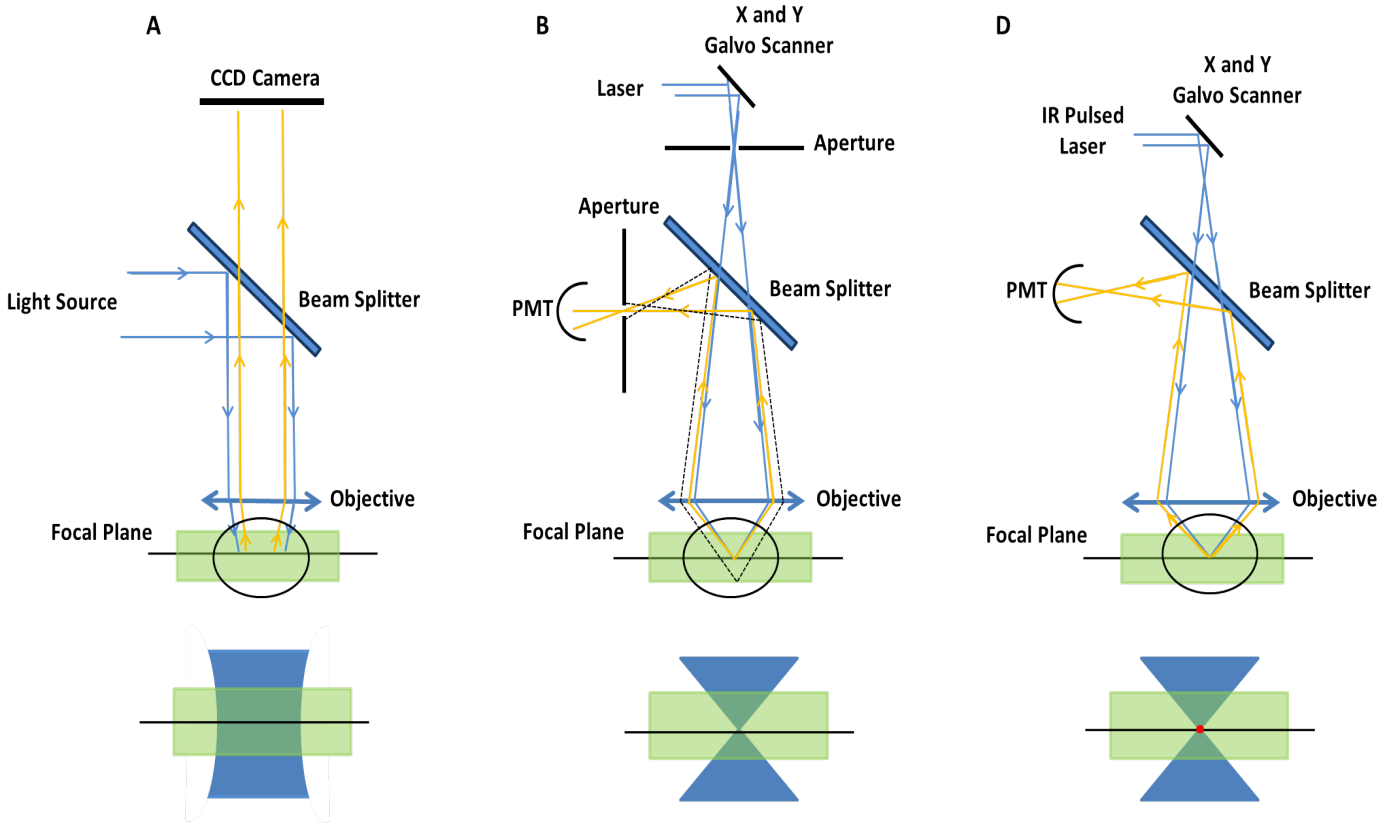


Figure 1.2: Fluorescent microscopes. *A*: A widefield fluorescent microscope. Most of the sample is illuminated by the light source. *B*: A confocal laser scanning microscope. The out of focus light is spatially filtered by conjugated apertures. *C*: A two-photon laser scanning microscope. Improved optical sectioning is achieved due to the two-photon absorption effect.

To obtain good EAPs with the previously described technology, the electrode tip needs to be relatively close to the neurons from which recordings are to be made (less than 100 μm [Obien et al., 2014]) making these techniques invasive. Moreover, recordings of single APs with MEAs and optrodes does not provide clear cellular spatial information.

To circumvent these problems, fluorescent markers can be introduced to biological tissues to enable light absorption and emission for functional imaging of neural networks. To achieve cellular resolution, widefield microscopy illuminating the entire sample of interest and ac-

quiring the resulted emitted photons (see Fig. 1.2 *A*) has been replaced with laser scanning confocal microscopy. The latter one-photon excitation point scanning technique improved the lateral and axial Point Spread Function (PSF) of the acquisition due to two conjugated apertures acting as spatial filters for the out of focus background light (see Fig. 1.2 *B*). More recently, non linear multi-photon excitation laser scanning extended the possibilities of functional imaging in neuroscience. This technique uses a high intensity near infrared short (around 100 fs) pulsed laser (around 80 MHz) to trigger the excitation of fluorophores confined to the objective lens focal volume (see Fig. 1.2). Hence, Multi-Photon Laser Scanning Microscopy (MPLSM) has multiple benefits over Confocal Laser Scanning Microscopy (CLSM) including higher imaging depth, less scattering, reduced photo-bleaching and improved cell viability. To acquire two dimensional images of neural circuits, both previous described laser scanning methods steer the laser beam in a raster manner via Galvanometric Scanners (GSs) over the sample. If these methods are directed to achieve sub-cellular resolution, the achievable temporal fidelity is reduced. The temporal resolution is further diminished as scanned cell number increases.

This short overview on neural stimulation and recording tools shows the need to develop new methods in two-photon microscopy enabling simultaneous acquisition of a large number of neurons. This engineering challenge constitutes the core of my PhD.

1.2 Introduction to two-photon microscopy

The principle of two-photon microscopy relies on the absorption of two photons having both half of the energy of a single photon [Göppert-Mayer, 1931] (see Fig. 1.3 A). This can be achieved experimentally by using a high power pulsed laser being strongly focused in very small focal volume (around $1\,\mu\text{m}^3$ see Fig. 1.3 B) [Denk et al., 1990]. This way, the probability of two-photon excitation is relatively high and the average energy deposited in the biological tissue remains low. The two-photon excitation process only happens at the focal

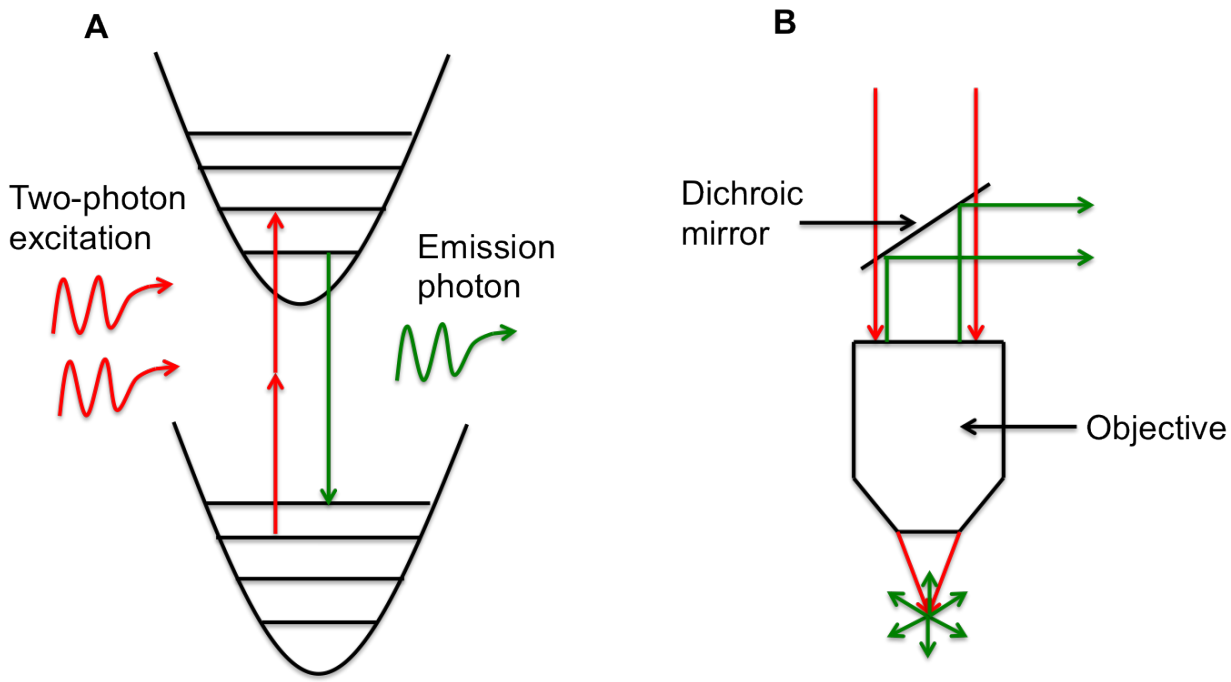


Figure 1.3: Two-photon technique. *A* Two photon are absorbed bye the fluorescent dye. This enables the dye to reach an excited state and reemit a photon upon its relaxation process. *B* Schematic of the two-photon process applied to an MPLSM.

point of the objective enabling an unprecedented axial optical sectioning (see Fig. 1.2 C). The use of calcium sensitive fluorescent dyes (for the entire panel of available dyes see section 1.4.1) together with an MPLSM enables functional calcium imaging in large neural networks with high spatial resolution. In our study, the mouse brain slices are filled (all the cells and neuropil up until 50 μm deep) with the synthetic calcium dye Cal-520. This way, two photons excitation processes will occur at the focal point of the objective by using approximatively twice the excitation wavelength of the fluorescent dye. These excited dyes in the tissue are then emitting photons at a different wavelength (see Fig. 1.3). These photons are emitted in every direction and only a fraction of them will go back through the objective (see Fig. 1.3 B). This process enables the acquisition of the background fluorescence of the dye and allows, thanks to raster scanning, to distinguish the structure of the tissue. Furthermore, the synthetic calcium dye Cal-520 is calcium sensitive. Therefore, the dye will perform intramolecular conformational changes upon binding to a calcium ion. This conformational change leads to an increase of more then 100 times the amount of emitted photons and enables to see a characteristic change in fluorescence in activated neurons.

Two main physical aspect are however limiting the capabilities of the MPLSM technique. First, the depth at which functional calcium imaging can be performed in brain tissues is limited to about -800 μm under the surface [Pilz et al., 2016] due to the mie scattering effect. Second, to avoid bleaching of the dye and damaging the tissue through heating, the amount of power delivered at the specimen should not be higher then about 15 mW.

1.3 Scanning neural circuits with a commercial two photon microscope

An established way to acquire two dimensional structural and functional images of neural circuits with MPLSM is to control the laser beam position with two GSs. This way, the focus of the laser beam can be led in a raster manner over cells loaded with calcium sensitive fluorophores linking each cells position to their spiking activity. However, the slow sequential nature of raster scanning does not scale well with calcium imaging of larger neural networks. To improve the temporal resolution of the acquisition, the voltage signal applied to the GSs can be optimized so that the path of the laser minimizes the mechanical strengths applied to the system whilst maximizing the time spent on collecting photons from neural somas (or any other kind of selected Region Of Interests (ROIs) from the structural image). These new scanning strategies allow the user to perform functional calcium imaging at higher sampling rates, pushing the boundaries of the number of cells scanned to around 1000 with a standard 'low cost' commercial MPLSM.

1.3.1 Galvanometric scanner for MPLSM

All oscillating high performance GSs used for the purpose of microscopy are built with the same main components: a mirror deflecting the laser beam, a magnet torque motor enabling the mirror to rotate, and an optical position transducer (See Fig.1.4 *A*). Each GS

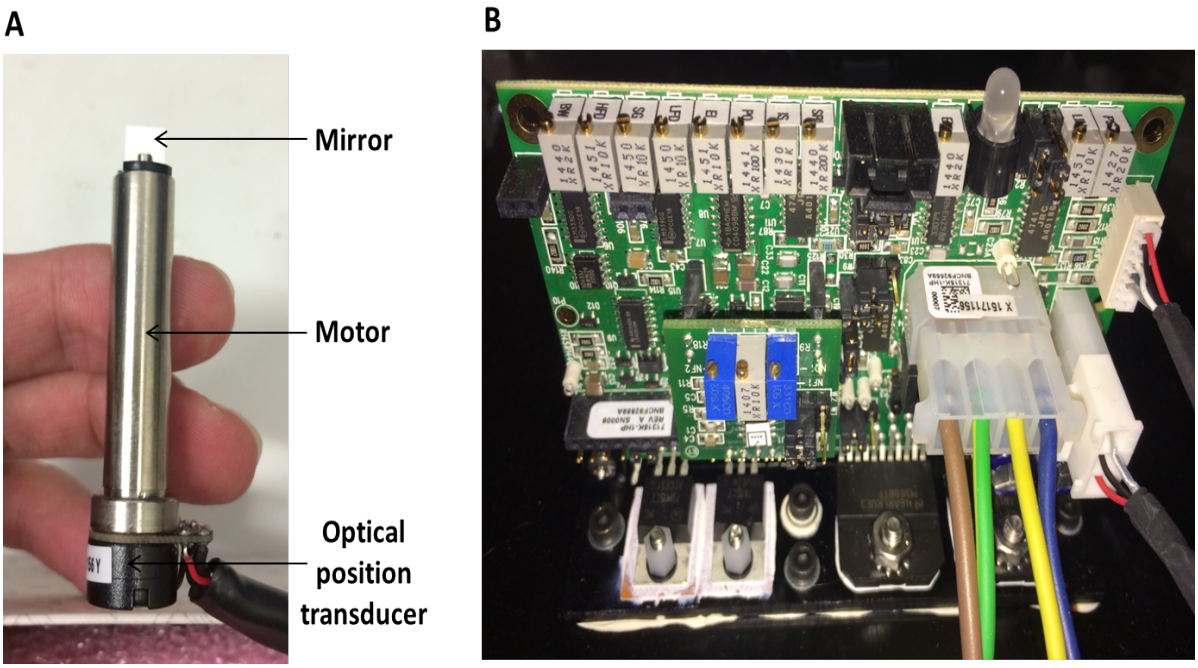


Figure 1.4: Galvanometric Scanners 6215H Cambridge technology. *A* GS showing 3 mm mirrors, a magnet torque motor and an optical position transducer. *B* Servo driver amplifier model Micromax 671XX.

is also using its own servo amplifier position closed loop feedback controller to maintain a high scanning accuracy (See Fig1.4 *B*) [Gerald F. Marshall, 2012]. In our lab, we used a pair of GS model 8315KL with a set of 3 mm XY mirrors and a dual axis analogue high power servo driver amplifier model MicroMax 671XX (all products from Cambridge Technology). Standard GSs can be driven with any kind of voltage waveforms within a range of amplitudes and frequencies whereas Resonant GSs (RGSs) can only be driven with a sine wave at their resonance frequency, which is generally between 4 and 12 kHz .

1.3.2 Raster scanning

Raster scanning (also known as frame scanning) is the most common way to acquire two dimensional structural and functional images with standard commercial MPLSMs (See Fig.1.5 *A* and *D*). Two GSs are required to steer the laser beam into sequential straight parallel lines over a square Field Of View (FOV). The 'X axis' GS (XGS) is responsible for the acquisition of fast horizontal lines whereas the 'Y axis' GS (YGS) moves slowly and ensures

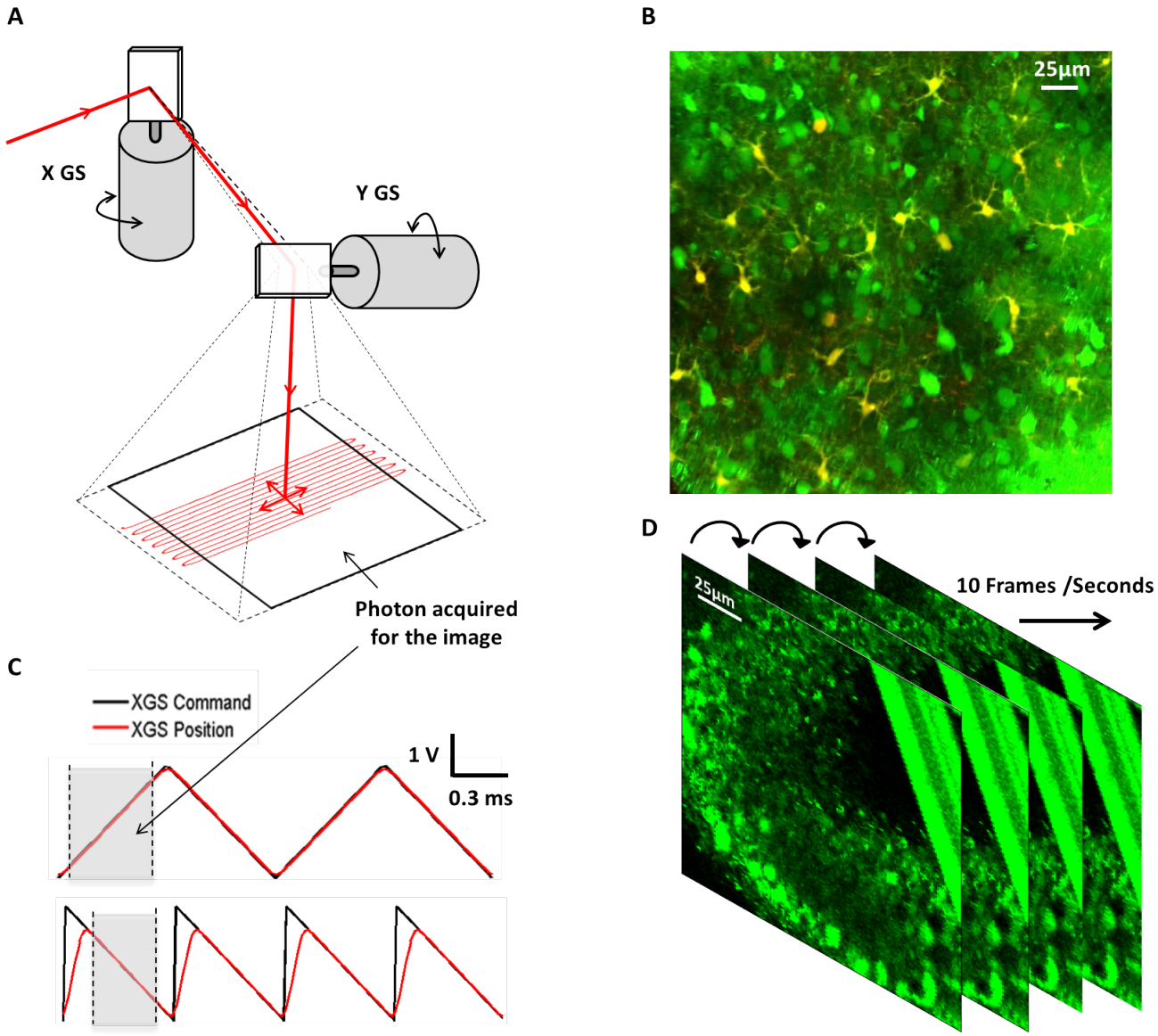


Figure 1.5: Raster Scanning with Galvanometric MPLSM. *A*: Schematic of GSs performing raster scanning with an MPLSM. *B*: Structural high resolution images ($300 \times 300\,\mu m^2$) of cortical neurons (green - loaded with the dye Cal520-AM) and astrocytes (yellow - loaded with the dye SR101 and Cal520-AM) from layer 2/3 of the visual cortex (see bath loading technique 3.3.2) acquired with the raster scanning technique. *C*: Triangular and sawtooth voltage commands (in black) applied to the XGS and actual position of the XGS (in red). *D* Example of functional calcium imaging of the Dentate Granular Cells (DGCs) at 10 Hz

tight equal spacing between the horizontal lines (See Fig. 1.5 *A* and *C*).

The acquisition of this separate horizontal lines can be done by either applying a 'saw-tooth' or a 'triangular' driving signal to the XGS. However, the critical moment of the acquisition is at the stage when the XGS has to turn around to scan a new line. There, both driving signals are non-linear and contain high frequency components inducing heat in the GS motor and servo controller as well as delay and drifting of the mirror position when compared with the original driving signal (See Fig.1.5 *C*) [Pologruto et al., 2003]. As a result of this effect, only the photons acquired during the linear part of the driving signal will be taken into account in the structural or functional image (See Fig. 1.5 *A* and *C*). When compared to each other, the triangular driving signal appear to apply less mechanical strain on the GS as it does not contain this 'fly back' period engendered by the sawtooth signal (see Fig.1.5 *C*).

Thus, on our MPLSM system, we are using the triangular driving signals which provides us functional raster scan images of neural circuits at a sampling frequency of 10 Hz for a FOV of $180 \times 180\,\mu\text{m}^2$ (see Fig.1.5 *D*). An improvement on raster scanning was achieved by [Tan et al., 1999] where they report sampling frequencies as high as 100 Hz for very small FOVs ($\sim 8 \times 4\,\mu\text{m}^2$) . They demonstrated that by using Fourier analyses, they could 'match' the linear segment of the sawtooth or the triangular waveforms with a sine, resulting in a driving signal that reduces the power used when the GS executes its turn around. A further improvement was been made in raster scanning by replacing the XGS by a RGS. In our hands, with an $8\,kHz$ RGS, we were able to perform calcium imaging at a sampling frequency of ~ 30 Hz for a FOV of $300 \times 300\,\mu\text{m}^2$.

To conclude, while raster scanning enables commercial MPLSM to perform functional calcium imaging of neural circuits, it suffers from its inherent sequential nature, forcing the laser beam to scan straight parallel lines over a square FOV. This lack of temporal resolution in the signal acquisition restricts the total number of neurons that can be scanned at once. This has the knock on effect of reducing accurate detection of calcium transient onset.

1.3.3 Two-dimensional scanning strategies

Two-dimensional scanning strategies are designed for *in vitro* fast calcium imaging. Their goal is to calculate the 'optimal' laser scanning paths mainly based on the positions of the ROIs (in our case neural somas), but also taking into account other aspects of the experimental framework. By doing so, their algorithm 'shapes' the voltage applied to both GSs in a way that the cellular sampling frequency of the acquisition is considerably enhanced when compared to raster scanning (see subsection 1.3.2).

Two-dimensional MPLSM scanning strategies were pioneered by [Lillis et al., 2008] in 2008. Their 'Targeted Path Scanning (TPS)' requires the user to select Segments Of Interests (SOIs) from a previously acquired high resolution image and also to define at which constant speed those SOIs are scanned to maintain a sufficient Signal to Noise Ratio (SNR) of the acquisition. All the SOIs are automatically linked to form a closed trajectory, and all links are scanned with maximal acceleration followed by maximal deceleration for acquisition speed and stability purposes. With their TPS, they were able to scan a total of 41 cells distributed over the major part of a juvenile rat hippocampus (Dentate Gyrus (DG), Cornu Ammonis 3 (CA3) and Cornu Ammonis 1 (CA1)) at around 100 Hz with single cell resolution and single AP sensitivity. However, this technique seems to only scale well for a small selected number of sparsely distributed neurons and does not seem to be a substantial improvement in comparison to raster scanning for cortical neural densities.

An automatic way of scanning larger neural population was later developed by Sadovsky et al. [Sadovsky et al., 2011]. After the acquisition of a high resolution image with raster scanning of cortical tissue loaded with the inorganic dye Fura2-AM, neural somas were automatically detected and fed as input into the Lin-Kerningham Heuristic Travelling Salesman Algorithm (TSA). This resulted in computing the shortest path between all the neurons which they called 'Heuristically Optimal Path Scanning (HOPS)'. Another feature of HOPS is the ability to change the imposed dwell time of the laser on neurons to preserve a good balance between SNR and speed of the acquisition. By applying HOPS on *in vitro* neural somas from the somatosensory cortex, they achieved sampling frequencies of around 150 Hz for

50 neurons and around 8.5 Hz for 1000 neurons, which is a considerable improvement over frame scanning. Nevertheless, using the shortest trajectory between ROIs gives rise to a path containing a lot of sharp turns imposing inertial slowdowns of the GSs.

We developed a two-dimensional scanning strategy for *in vitro* fast calcium imaging called 'Adaptive Spiral Scanning (SSA)' that takes into account the mechanical properties of the GSs [Schuck et al., 2014]. By implementing a second order linear model of the GSs, we could simulate the performances of scanning strategies. We then designed the SSA algorithm as a set of circular trajectories where the radius is constantly updated depending on the position of the neurons, to lessen the impact of the GS's inertia upon the scanned path. By doing this, we show that we can scan 200 targets at around 100 Hz and that we outperform HOPS in scanning rates for common cortical neural densities.

The benefits of scanning strategies are multiple as they are easy to implement and come at a low cost as they do not necessitate additional hardware integration.

1.3.4 Three-dimensional scanning with MPLSM

Standard three-dimensional imaging with a commercial MPLSM is performed by successively raster scanning a plane in the tissue at different depths (max depth $700\,\mu$m). This procedure takes time as the frame rate of raster scanning a plane of $180 \times 180\,\mu\text{m}^2$ is around 10 Hz (see subsection 1.3.2). Hence, if raster scanning is a good technique to get structural information in deep scattering tissues, it does not facilitate three dimensional functional calcium imaging considering the kinetics of the most popular calcium dyes [Schultz et al., 2017].

To circumvent this issue, three-dimensional scanning strategies can be developed by either adding a piezo actuator or an Electrical Tunable Lens (ETL) to replace the slow axial objective micro-manipulator. In 2007, Goebel et al. [Goebel et al., 2007] achieved volumetric *in vivo* functional calcium imaging at 10 Hz using a piezo actuator combined with smart-line scanning applied to the GSs. They report a cubic volume coverage of 90% of $0.25 \times 0.25 \times 0.20$ mm^3 using a three-dimensional line scan. In 2011, Grewe et al. [Grewe

et al., 2011] used an MPLSM mounted with Acousto-Optical-Deflectors (AODs) and an ETL. With this technology, they show that they could scan 34 cells *in vivo* (somatosensory cortex) distributed in 2 focal planes separated by 40 μm at a sampling frequency of 21.6 Hz.

We developed a 3D scanning strategy simulation platform for fast functional calcium imaging [Schuck et al., 2015], using a mechanical model of an ETL (the one used in [Grewe et al., 2011]) built on our previously developed 2D SSA algorithm. Two 3D scanning strategies were developed: the first one used a stepwise driving signal for the ETL resulting in a 3D Cylindrical Scanning Trajectory (CST); whilst the second one uses an amplitude modulated sine resulting in an 3D Orbital Scanning Trajectory (OST). Both CST and OST can be performed with an affordable ETL with a commercial MPLSM and enable, in theory, faster and preciser 3D neural population scanning when compared to Goebel et al.,(2007) and Grewe et al.,(2011) [Goebel et al., 2007, Grewe et al., 2011].

Our developed 3D scanning strategy simulation platform has the potential to enable the user to draw/use any kind of 3D trajectory in a simple software application. This trajectory is then directly translated into voltages controlling the optical elements of the MPLSM enabling the user to precisely control the position of the focal point in 3D (GSs (X,Y) and ETL (Z)).

1.4 Fast functional calcium imaging and its limitation

Voltage gated calcium channels are responsible for an influx of extracellular calcium ions, 10 to 100 times the intracellular neuronal resting concentration, following an AP event [Berridge et al., 2000]. They are the main components mediating intracellular calcium ion level fluctuations when compared to other mechanisms involved in this process [Grienberger and Konnerth, 2012]. Therefore, a modern way of deciphering the activity of large neural networks is by simultaneously monitoring the calcium concentration in each individual cell and translating it into their electrical activity. This has been made available by labelling *in vivo* or *in vitro* neural circuits with activity dependent synthetic calcium dyes. Scanning strategies enhancing the sampling rate of the acquisition are therefore becoming necessary

to scan larger neural networks considering the kinetics of these calcium sensors [Schultz et al., 2017], and the point scanning nature of a commercial GS based MPLSM. As scanning strategies are based on the structure of the neural network (line scan passing through neural somas previously acquired with raster scanning; see subsection 1.3.2), they require extreme precision. Therefore, scanning strategies are more suitable for *in vitro* experiments in this respect as they don't suffer from movement artifacts as much as *in vivo* experiments.

Another *in vitro* application where software control of the precise 3D position of the focal point of an MPLSM (as previously described in 1.3.4) becomes important is in creating hydrogel micro-environments for cell cultures. This very new field of study will only be briefly discussed.

1.4.1 Calcium dyes for MPLSM functional imaging

Calcium dyes can be separated into two main categories: the activity dependent synthetic calcium dyes and the calcium sensitive Genetically Encoded Calcium Indicators (GECIs).

Activity dependent synthetic calcium dyes

The first synthetic calcium dyes enabling an insight into cellular activity were aequorin [Ashley and Ridgway, 1968] and arsenazo III [Brown et al., 1975]. However, these dyes were not membrane permeable meaning that they had to be delivered to a single cell with a micropipette. New versions of calcium synthetic dyes were developed upon molecular research, increasing their sensitivity, kinetics and making them capable of being membrane permeable. The most popular among them (known for their high SNR) were Fura2-AM [Tsien et al., 1985, Wokosin et al., 2004, Neher, 1995, Sohya et al., 2007] and later OGB1-AM [Schultz et al., 2009, Sato et al., 2007]. Both dyes undergo an intramolecular conformation change when binding to a calcium ion. This results in a decrease in fluorescence for Fura2-AM and an increase in fluorescence for OGB-AM. More recently, the latest newly developed synthetic calcium dye: Cal-520, achieved fast kinetics and unprecedented SNR values [Tada

et al., 2014]. Its red-shifted version, Cal-590, also enables imaging *in vivo* in deep scattering tissues, up to $-900\,\mu$m below the pial surface while keeping a good SNR [Tischbirek et al., 2015].

For *in vitro* experiments, the membrane-permeable activity-dependent calcium synthetic dyes can be introduced into the tissue with the bath loading technique (see 3.3.2). This results in a uniform labeling of the brain slice for imaging up to $-70\,\mu$m under the surface of the slice [MacLean et al., 2006]. Deeper labeling of the tissue can be achieved *in vitro* as well as *in vivo* by using the bulk loading technique [Stosiek et al., 2003] which consists of locally releasing the dye into the tissue with a micro-pipette (see 5.1.2). These methods enable researchers to label large populations of neurons with a high success rate and are relatively easy to implement. However, they also label the surrounding neuropil inducing a certain level of background fluorescence that can be harmful to the recordings of calcium transients made with an MPLSM due to decreasing the SNR.

GECIs

In 1997 *Miyawaki et al.* achieved a breakthrough in the field of biosensors by developing protein based GECIs. However, in their early development, even the most effective GECIs based on the most popular GCaMP structure possessed a low SNR and poor kinetics when compared to synthetic calcium dyes [Tian et al., 2009]. Nevertheless, recent developments of this same structure, named: GCaMP6, showed strong improvements on both the SNR and the kinetic aspects and hence now constitute a good alternative to synthetic calcium dyes [Chen et al., 2013]. Their advantages over synthetic calcium dyes is threefold: their expression process can be non-invasive, it can be targeted to specific neurons, and it lasts over chronic timescales for *in vivo* experiments (when compared to bulk loading which lasts only 2 to 3 hours *in vivo*). In practice however, the degree of expression of GECIs is less reliable than using synthetic calcium dye preparations.

For the signal quality assessment with our scanning strategy purposes, I chose the syn-

thetic calcium dye Cal-520 for its high SNR, good kinetics and simplicity of use in *in vitro* experiments. I used the AM version with the bath loading technique (see 3.3.2) enabling the entire slice to be labeled and recorded spontaneous activity from Dentate Granular Cells (DGCs). I also used the Potassium salt version delivered using the single cell approach with a patch pipette enabling the simultaneous recordings of calcium time series and corresponding electrophysiology traces (see 3.3.3).

1.4.2 Fast functional calcium imaging in slices

An advantage of *in vitro* brain slicing is that it allows easy access to every region of the brain and therefore functional calcium imaging in areas not attainable *in vivo* (depth of imaging with an MPLSM only allows access to a maximum of around $-900\,\mu$m below the surface with redshifted dyes [Tischbirek et al., 2015]). Precise slice preparation enables the preservation of certain connections between different areas of the brain e.g visual/auditory/somatosensory thalamocortical connections [Cruikshank et al., 2002, Agmon and Connors, 1991, MacLean et al., 2006], entorhinal cortex-hippocampal connections [Schwartz and Coleman, 1981, Per Andersen Richard Morris, 2007], and many others. However, it is important to recognise that *in vitro* and *in vivo* techniques have their distinct advantages and disadvantages.

Mesoscale functional calcium imaging with a commercial GS based MPLSM has only been achieved with the HOPS technique [Sadovsky et al., 2011] as described in subsection 1.3.3. By labelling cortical tissue with Fura2-AM , they were able to scan around 1000 neurones at $8.5\,Hz$ across different cortical layers and columns. Using this technique, they show that the development of spontaneous activity in two regions of the mouse neocortex: somatosensory cortex (S1BF) and auditory cortex (A1), follow a similar evolution [Frye and MacLean, 2016]. The first phase (seen at Post Natal Day (PND) 3 for S1BF and PND 8 for A1) consist in recruiting neighbour neurons in a very small and localised region. Whereas the following second phase (PND 9 S1BF and PND 13 A1) generalises the spontaneous activity to the entire imaged network. Finally, the last phase of cortical development of spontaneous

activity (PND 14 S1BF and PND 15 A1) shows a sparse representation across the imaged cortical layers and columns. These analyses are coherent with previous studies [Rochefort et al., 2009, Siegel et al., 2012] and indicate an internal circuitry development for spontaneous activity common to the entire neocortex rather than to a selective sensory area.

Another investigation at the mesoscale level of neural circuitry involving *in vitro* somatosensory thalamocortical connections in brain slices was recently achieved with HOPS [Sederberg et al., 2015]. They electrically stimulated two distinct regions of the ventral posteromedial nucleus and tried with a linear decoder to characterise these two afferent thalamic inputs by imaging hundreds of neurones in the somatosensory cortex. They show that only a few sparsely distributed neurones in the somatosensory cortex could decode the thalamic stimulation at a level above chance. Furthermore, they report that after 10s to 100s of milliseconds following the stimulus onset, additional neurones were recruited that enabled the decoding of the thalamic stimulation at a level above chance. *Sederberg et al.* can combine the use of mutliphoton imaging and electrical stimulation without encountering any Becquerel artefact as the imaging FOV (in the somatosensory) and the tip of the electrode (in the thalamus) are not overlapping and separated from 2 to 3 mm. The Becquerel effect can be induced by the two-photon pulsed laser into the stimulating micro-electrode whenever the imaging FOV is overlapping or very close with the tip of the stimulating electrode. One possibility to reduce this phenomenon is to zero or blank the laser light amplitude when it is rastering the micro-eletrode.

While the field of optical engineering in MPLSM is developing quickly with new emerging scanless technologies e.g light sheet microscopy [Palero et al., 2010, Bouchard et al., 2015] or holographic two-photon imaging [Nikolenko et al., 2008, Foust et al., 2015], it requires very expensive additional hardware implementations when compared to scanning strategies, which are easily transferable and achieve mesoscale functional calcium imaging.

1.4.3 Limitations of Calcium imaging

Mechanisms making the intracellular calcium concentration fluctuate are coming from diverse sources e.g voltage gated calcium channels, ionotropic glutamate receptors, nicotinic acetylcholine receptors, endoplasmic reticulum releases and the sodium-calcium exchanger [Grienberger and Konnerth, 2012]. However, even the intracellular calcium concentration is governed by many physiological processes, it has been proven that upon an AP, the cytosolic calcium concentration of a cell rises almost instantaneously from around 10 to 100 times [Berridge et al., 2000]. Therefore, in brain tissues loaded with a calcium sensitive dyes, the temporal limiting factor is not how fast the calcium ions are reaching the dyes in the cytosol but the kinematics of the chemical reaction between the calcium ion and the synthetic calcium dye. This chemical reaction dictates the temporal profile of the calcium transients recorded with an MPLSM. In our study, the synthetic calcium dye Cal-520 has a dissociation constant of K_d=320 nM. The calcium transient associated to this chemical reaction has a rising time of around 70 ms and a decay constant of around 800 ms. These time constants are for one AP [Tada et al., 2014]. This shows that the induced calcium transient has a temporal profile lasting about 1000 times longer then the AP. This kinematic difference is valid for all the recently developed calcium dyes and therefore does not allow calcium imaging to track the activity of high firing rate neurons.

Furthermore, cellular subthreshold events that can be detected by the patch clamp technique are invisible with calcium imaging due to the lack of SNR of the calcium dyes. This can be assessed when both techniques are used simultaneously. Recent development of 'voltage' fluorescent dyes are getting closer to the kinematic of a spike [Knöpfel et al., 2015], however, it remains to be seen if their future development achieve a sufficient SNR to detect a single AP event.

1.4.4 Recent progress with customised two-photon microscopes

In the recent years, scanless two-photon microscopy technologies have been developed enabling high speed volumetric functional calcium imaging. With the use of a cylindrical lens, the pulsed laser can be focused into a tight compressed light sheet achieving optical sectioning between 1 and 10 μm [Fuchs et al., 2002, Palero et al., 2010, Ahrens et al., 2013]. This light sheet illumination is orthogonal to the imaging axis and enables the two-photon excitation of an entire plane at once. Fast volumetric calcium imaging is then achieved by moving the sample axially. With this method, *Ahrsen et al.* were able to record the activity of 80% of the entire brain of the zebrafish at a single cell resolution at a sampling frequency of 0.8 Hz. This technique is however limited to orthogonal illumination (in regard to the imaging axis) of almost transparent specimens like zebrafish or C. elegans and can therefore not be used in mice. However, the new developed technique "temporal focusing" developed by *Oron et al.* [Oron et al., 2005] manipulates the temporal profile of the pulsed laser thus allowing two-photon excitation of a sheet on axis. This technique, when coupled with the use of an ETL [Jiang et al., 2015] or piezo actuator [Schrödel et al., 2013], enables fast volumetric functional calcium imaging in mice *in vivo*.

Sofroniew et al. recently achieved functional calcium imaging at the mesoscale level extending the FOV of the acquisition with a customized scanning two-photon microscope called 'Mesoscope' [Sofroniew et al., 2016]. This new scanning technique is build with one Resonant GS and a pair of standard GSs and achieves a sampling rate of 0.7 Hz for a FOV of 4.5x5.5 μm^2 with cellular resolution. Additionally, using a build in remote focusing unit enables the focal point of the mesoscope to scan a volume (cylindre) of 5 mm diameter and 1mm depth. Another interesting feature of this microscope is that it achieves to image four 0.6 mm^2 FOVs in different mouse brain areas at a sampling frequency of 9.5 Hz. This mesoscope pushes the boundary of volumetric functional calcium imaging *in vivo* and is now commercially available and sold by the company 'Neurolabware'.

Functional calcium imaging, even if extending rapidly (see the above described imaging techniques), is still limited to a certain imaging volume. For structural purposes where time is

no longer an issue, fixed neural tissue has brought new insight into brain connectivity and amount of neurons being imaged. *Tomer et al.* were able to image an entire mouse brain with light sheet microscopy and using the CLARITY solution to 'clear' the mouse 'fixed' brain [Tomer et al., 2014]. Another technique consist in using a regular two-photon scanning system coupled to a vibratome. At each depth, an entire brain surface is imaged by stitching together each FOV. Once an entire horizontal brain surface has been imaged, the vibratome cuts the surface by a certain amount of microns before the next brain surface is imaged. This technique, even if relatively slow, enables to image an entire mouse brain with cellular resolution and without the need of using a clearance solution [Economo et al., 2016]. These new emerging structural imaging techniques are rising new challenges regarding data collection and manipulation as one entire mouse brain represent about 10 TB of disk space.
All these imaging techniques using customized optics are pushing the boundaries of structural and functional imaging with cellular resolution. However, these customized microscope are not always available commercially or come at a very high cost so that not every lab can afford them. In this thesis, we provide a cost effective software solution enabling to increase the number of scanned neurons with a standard MPLSM. This will affect all the labs which need fast functional calcium imaging and can not afford to pay customized optics.

1.5 Cell culture micro-environment design

The optical sectioning achieved with an MPLSM is unprecedented. This enables fast and precise functional calcium imaging in deep scattering tissue but can also be used in the purpose of photolithography in specific materials. When appropriately controlled, the focal point of the MPLSM can engender different kind of chemical reactions and amongst them the photo-patterning, photo-degradtion and polymerisation effect. Cell compatible or cytocompatible synthetic 'click-based' hydrogels [Kolb and Sharpless, 2003], based on wavelength-specific photochemical reactions, have enabled the design and control of three dimensional micro-environments for cell cultures. Guided 3D cell migrations were achieved by Lee et

al. (2008) [Lee et al., 2008] by raster scanning cubical shapes with two-photon photolitography. To perform this experiment, they first embedded a human dermal fibroblast into their crosslinkable hydrogel. Secondly, they diffused a cell adhesive peptide Arg-Gly-Asp-Lys (RGDSK) into the entire hydrogel. Finally, the hydrogel was washed from the cell adhesive peptide except for the region where it was linked to the hydrogel due to the two-photon photolitography. Upon this process, they show that cells migrated out of the human dermal fibroblast in the hydrogel, only in the regions patterned with the RGDSK peptide. This study constitutes the first achievement of a cytocompatible micro-environment design for cell culture guidance in three dimensions. Furthermore, the confinement of the MPLSM focal volume can enable precise photochemical reactions (depending on the chemistry of the hydrogel) leading to a good level of control upon the activation of biochemical signals in the presence of living cells [Kloxin et al., 2012, Deforest and Tirrell, 2015].

As described above, previous studies have shown that the use of an MPLSM can enable spatiotemporal control of a three-dimensional micro-environment conceived for cell culture. However, all these studies lack good control of the focal spot of the MPLSM. Therefore, in subsection 5.3, we show a proof a principle of our control system enabling a localized photopatterning process in 2D.

1.6 Introduction to the dentate gyrus

Amongst the principal structures of the hippocampus, the functionalities of the DG are the least well understood when compared to CA1 and CA3. In this thesis, we focus on the DG for a couple of reasons. First, the granular layer of the DG was the perfect platform to test our newly developed scanning algorithm on dense neural populations. Secondly, the genuine functionalities of the DG have only been investigated with electrophysiology recording techniques *in vivo* and did not give clear and satisfactory results. We were able to get a high data throughput of spontaneous and evoked activity from large Dentate granular cell populations by using an MPLSM and changing the experimental setup into *in vitro* hippocampal

brain slices experiments. This is exciting as these data will enable new types of analyses to be performed on the functionalities of the DG. Lastly, it is known that the DG is involved in pattern separation processes and memory formation. With our setup, we could again get a high data throughput with an Alzheimer mouse model and then compare the collected data with an aged matched wild type mouse. Furthermore, we could try with these acquired data to estimate how much the Alzheimer neuropathology is playing a role into memory formation and pattern separation processes in the DG.

1.6.1 Structure of the dentate gyrus

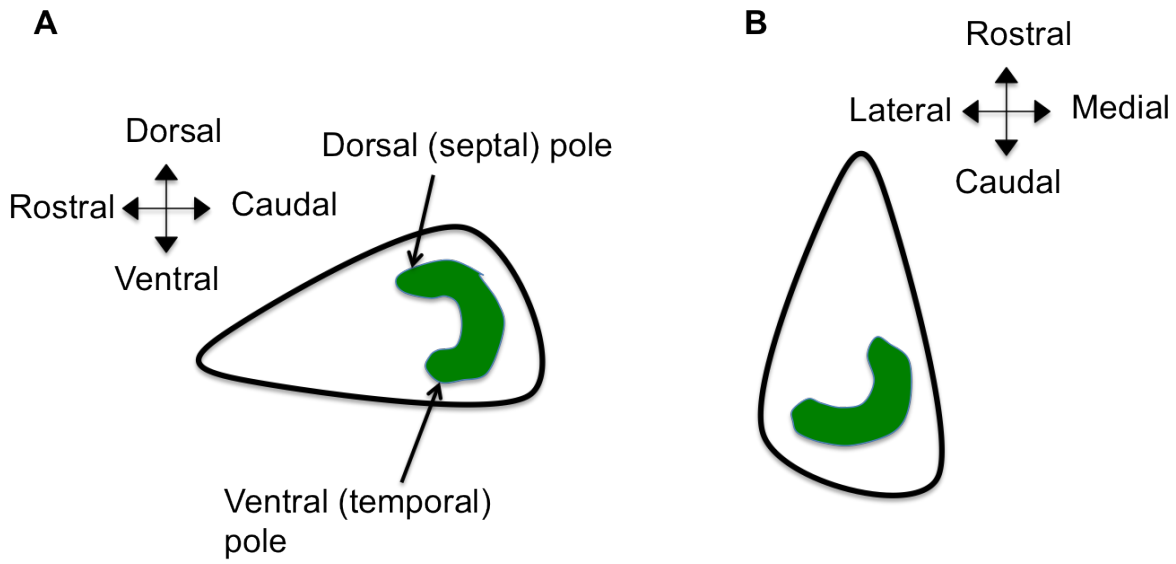


Figure 1.6: Schematic and positioning of the hippocampus in the mouse brain. *A* Dorsal-ventral rostral-caudal schematic of a half hemisphere mouse brain (shape in black) and hippocampus (in green). The dorsal part of the hippocampus is also know as septal pole and the ventral part of the hippocampus is also known as temporal pole. *B* Dorsal-ventral medial-lateral schematic of a half hemisphere mouse brain (shape in black) and hippocampus (in green).

The DG is one of the three main parts of the trisynaptic circuit of the hippocampus (the others being Cornu Ammonis 1 (CA1) and Cornu Ammonis 3 (CA3)) see Fig.1.7 *B*. It receives mainly inputs from the Entorhinal Cortex (EC) see Fig.1.7 *C*. The DG is composed of three main layers: the Molecular Layer (ML), the Granular Layer (GL) and the Hilus. This repartition in layers is identical for rodents, monkeys and humans [Scharfman, 2007].

The DG blade that is contained between CA3 and CA1 is called suprapyramidal whereas the opposite blade is called infrapyramidal. The middle part of the DG is called the crest (see Fig.1.7 *C*). The principal cells found in the DG are in the GL and are called the Granular Cells (GCs). These cells are small, round (around $10-15\,\mu$m in diameter) and excitatory with glutamate as their main neurotransmitter [Toni et al., 2008] (although certain studies show that they present a joint GABA and glutamate phenotype [Gutierrez, 2016]). The total number of GCs has been estimated at 1.2×10^6 in rats [West and Gundersen, 1990, Rapp and Gallagher, 1996]. A specificity of the DG in adult subjects is that there are constant newborn GCs integrating with the mature part of the GL. However, the total number of GCs seems to be constant over time implying a steady replacement of mature GCs with newborn GCs [Kempermann et al., 1997, Per Andersen Richard Morris, 2007]. If the total number of GCs seems to be constant during adulthood (in usual conditions), their dorsal-ventral cell density is not. In the septal lobe of the GL, the ratio between GCs and Pyramidal Cells (PCs) of CA3 is 12:1 whereas at the temporal lobe the density of the GCs decreases giving the ratio of 2:3 [Gaarskjaer, 1978] (see Fig.1.6 *A* and *B* for septal and temporal lobes). In rodents, the dendrites of the GCs are only apical in the ML (see Fig1.8 *A* and *B*) whereas the axon of the GCs, also called Mossy Fiber (MF), is apical in the Hilus. The MF has a main trunk but separates into several thinner collaterals. On their way to the pyramidal cells of CA3, the MFs also connect to a multitude of inhibitory interneurons, all located in the Hilus (see Fig.1.7 *D*).

Basket cells (BCs) are well studied large ($25-30\,\mu$m) pyramidal GABA inhibitory neurons, found in the Hilus. The dendrites of these BCs are confined in the Hilus whereas their axons cross the GL and upon entering the ML split almost symmetrically. Part of the BCs axon's segments form contacts with GCs dendrites and others (the axon segments going along the separation between GL and ML) form contacts with the GCs directly [Scharfman, 2007] (see Fig.1.7 *B* and *C*) . The axons of the BCs are very long so that one BC contacts around 10,000 GCs, which represents approximatively 1% of their entire population.

Another famous cell in the Hilus is the Mossy Cell (MC). MCs have relatively big somas ($25-30\,\mu$m) and are characterized by having two to four thick and curvy dendrites

with multiple branches. A singularity of these MCs is their colossal amount of so-called thorny spines on their distal dendrites strongly innervated by the MFs collaterals (see Fig.1.7 *C* and *D*). Like GCs, the MCs are to glutamatergic [Soriano and Frotscher, 1994, Scharfman and Myers, 2013]. If most of their projections are in the Hilus on the MFs and the GABA interneurons, some of them still penetrate and innervate the GL, building an interesting excitatory feedback loop [Scharfman, 1994, Scharfman, 1995] (see Fig.1.7 *C* and *D*). Since, many other cell types of inhibitory interneurons have been found in the Hilus [Houser, 2007] making the entire DG a complex structure balanced between excitatory and inhibitory neurons.

1.6.2 Functionalities of the dentate gyrus

The role of the DG is still not well understood when compared to the other the main parts of the hippocampus (CA1 and CA3). This is partly due to its cellular complexity described in 1.6.1. A key point to understanding it, is to study the afferent inputs coming mainly from the EC. The two main inputs of the DG are coming from the lateral EC and the medial EC. The lateral EC is known to process non-spatial information like objects, odors whereas the medial EC is known to process more spatial related information [Witter et al., 1989, Hargreaves, 2005]. Therefore, one can consider that the DG can provide the function of 'conjunctive encoding' of space and objects as both lateral and medial EC are projecting to the DG via the PP [Poucet, 1989, van Groen et al., 2003, Witter, 2007, Hunsaker et al., 2007].

A second function associated to the DG is its ability to perform spatial pattern separation. This assumption is based on behavioral experiments in rodents. One famous experimental paradigm developed by Poucet et al. (1989) consists of comparing control rats with rats with lesions in DG, CA3 and CA1. All the rats from the experiments were first habituated to two visual objects prior to the induction of any lesions into a hippocampal structures. At this point, the two objects on a cheesemaze were separated by a constant distance. After repeated exploring sessions, the rats started to get habituated to the visual clues and spend

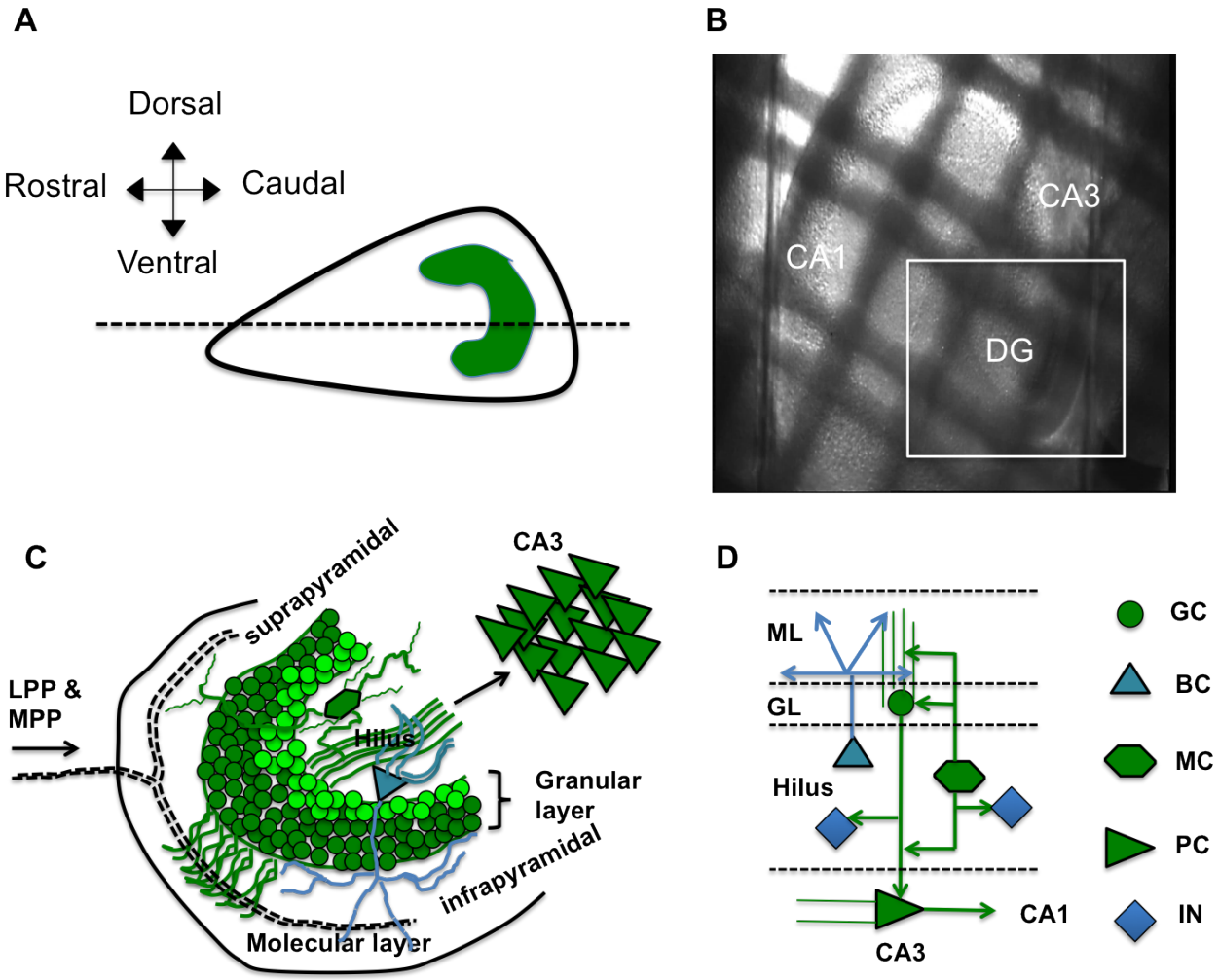


Figure 1.7: Structure of the Dentate Gyrus. *A* Schematic showing the location of a horizontal section (dashed line) that includes the trisynaptic loop. *B* Oblique illumination image of a mouse hippocampal slice lying on a mesh with a 4X objective (see 3.3.3). The principal regions of the trisynaptic circuit : DG , CA3 and CA1 are visible. *C* and *D* Schematics of the DG. Representation of the three layers: Molecular Layer (ML), Granular Layer (GL) and Hilus layer and of the most well-known cell types: GCs, Basket Cells (BC) and Mossy Cells (MC). In *C*, in the GL, the deep green represents mature GCs whereas the light green represents adult newborn GCs. Various number of Interneurons (IN) are also found in the GL. In *D*, some branches of the MFs are projecting to the CA3 Pyramidal Cells (PCs). The color code for the cells is blue for inhibitory cells and green for excitatory cells.

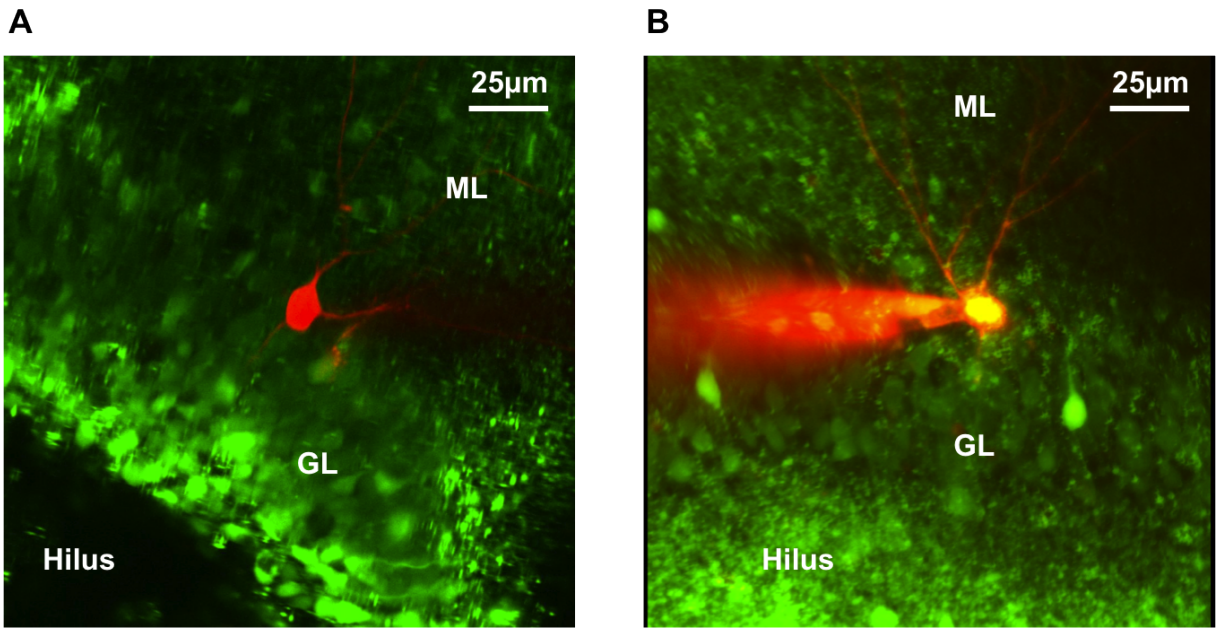


Figure 1.8: Structural MPLSM images of GCs. *A* High resolution image (1024×1024 pix^2 for $180 \times 180\,\mu$m^2) showing mostly the GL but also part of the ML and part of the Hilus. One GC was patched (whole cell, see 3.3.3) and filled with Alexa in red (the patch pipette in red was removed when the image was taken). *B* 3D reconstruction of a stack of high resolution images showing ML, GL and Hilus. One GC was patched and filled with internal solution containing the dyes Cal520 AM (green) and Alexa (red) (see 3.3.3).

less time exploring them. Once this training was achieved, the rats were divided into 4 categories: control, rats with lesions induced in DG, rats with lesions induced in CA3 and rats with lesions induced in CA1. The rats were then placed into this same environment except that at each trial, the distance between the two visual cues was changed. The rats with lesions in DG did not spend more time exploring the visual objects at different distances whereas the rats with lesions only in CA3 or only in CA1 and intact DG spent more time (closer timing to the control rat batch) exploring these two visual cues placed at different distances. The second experiment consisted of placing four visual cues on a cheesemaze. Here also, prior to any lesions, the rats were habituated to explore the four visual objects. Subsequently, lesions were induced in the hippocampal structures of the rats as previously described and the animals were placed on a cheesemaze with two object positions being switched. This time the rats with lesions in the DG and the rats with the lesions in CA3 had a re-exploring time of the environment closer to the control rats and only the rats with lesions in CA1 almost did not notice the switch between the visual objects. Taken together, the results of both behav-

ioral experiments show that the DG is involved in visual object metric scale modifications but is not affected by topological map rearrangements of visual objects. This conclusion led researchers to think that the DG is involved in spatial pattern separation. Recent studies involving high resolution fMRI imaging in humans support this evidence that the DG is engaged in pattern separations processes [Berron et al., 2016].

Often studied separately to the notion of conjunctive encoding and spatial pattern separations, the role of the DG in the acquisition and retrieval of memory is still an active subject of debate. Many controversial behavioral results on the interaction between CA3 and DG for encoding and retrieval of spatial information were found using the Hebb-William maze experimental paradigm [Kesner, 2007, Treves et al., 2008]. However, the combination of new optical - bio - pharmaco-technologies resulted in a new definition of memory associated to engram cells. The experimental goal for the proof and an 'engram complex' is threefold. First, one needs to show that a set of cells are active upon a contextual learning task. Second, one needs to prove that this specific set of cells experience structural or chemical changes in the process of learning, and third, that by activating part (in the case of pattern completion) or all of these cells, there is a recollection of this memory from the animal [Tonegawa et al., 2015]. The experimental design to prove these three steps is, however, extremely challenging. However, some supporting evidence of these three steps prove that the DG contains engram cells. In 2014, Denny et al. showed the inhibition of fear memory formation by optogenetically silencing active cells of the DG during contextual fear learning tasks. This experiment showed a loss of function of the mouse to recall fear memory and is sustainable evidence that these inactivated cells in the DG are part of an 'engram complex' [Denny et al., 2014]. An even stronger evidence, related this time to a gain of memory function, was demonstrated in an experiment carried out by Liu et al. (2012) showing the activation of contextual fear memory in mice by optogenetically activating engram cells in the DG [Liu et al., 2012]. Both previous experimental findings, however, do not demonstrate any structural or chemical change during the learning process of contextual fear. The only study demonstrating these neuro-chemical modifications during the learning or encoding phase of contextual fear has been done by Ryan et. al (2015). They put in evidence that a rapid synaptic strengthening as well as a change

in structural plasticity occurs in engram cells in the DG during this memory encoding period [Ryan et al., 2015]. These very recent studies show the importance and involvement of the DG in encoding and retrieval of memory.

In this DG introduction I first showed in 1.6.1 the complex cellular and synaptic structure of the DG. I then explained in 1.6.2 the past and current experimental paradigms which achieved (only partially) to assess in which higher brain functions the DG is involved. However, there has not been many experimental studies trying to link the two aspects presented here. In the last chapter of this thesis 5, I show that using functional calcium imaging with an MPLSM in *in vitro* experiments on hippocampal slices might provide a good experimental platform for the unexplored bridge between both structure and higher brain functions in the DG.

1.7 Publications

The first two published conference papers cited below constitute the main core of Chapter 2 and Chapter 4, respectively. Chapter 3 represent the Journal paper that has just been submitted. Each of these chapters contain more informations and details than the paper in itself and a future work or appendix section is added for completion.

Published papers:

Scaling up multiphoton neural scanning: the SSA algorithm. Schuck R., Annecchino L.A, Schultz S.R *Conf. Proc IEEE Eng.Med.Biol.Soc. 2014*

Rapid three dimentional two-photon neural population scanning. Schuck R., Quicke P., Copeland C., Garasto S., Annecchino L.A, Hwang J.K, Schultz S.R *Conf. Proc IEEE Eng.Med.Biol.Soc. 2015*

Advances in Two-Photon Scanning and Scanless Microscopy Technologies for Functional Neural Circuit Imaging Schultz S.R, Copeland C., Foust A.J, Quicke P., Schuck R. *Proceedings of the IEEE, Volume 105, Issue 1, Jan 2017*

Paper accepted and about to be published:

ALBE:an Activity-Based Level Set Segmentation Algorithm for Two-Photon Calcium Imaging Data Reynolds S., Abrahamsson T., Schuck R., Sjstrm P.J, Schultz S.R and Dragotti P.L. *eNeuro*

Paper accepted and about to be published:

Multiphoton minimal inertia scanning patterns for fast calcium dynamics acquisition Schuck R., Go A., Garasto S., Reynolds S. and Schultz S.R *Journal of Neural engineering*

Chapter 2

Simulation platform for 2D scanning strategies: the SSA algorithm

2.1 Abstract

In order to reverse-engineer the information processing capabilities of the cortical circuit, we need to densely sample the neural circuit; it may be necessary to sample the activity of thousands of neurons simultaneously. Frame scanning techniques do not scale well in this regard, due to the time 'wasted' scanning extracellular space. For scanners in which inertia can be neglected, path length minimization strategies enable large populations to be imaged at relatively high sampling rates. However, in a standard multiphoton microscope, the scanners responsible for beam deflection are inertial, indicating that an optimal solution should take rotor and mirror momentum into account. We therefore characterized the galvanometric scanners of a commercial multiphoton microscope, in order to develop and validate a MATLAB model of microscope scanning dynamics. We tested the model by simulating scan paths across pseudo-randomly positioned neuronal populations of differing neuronal density and field of view. This model motivated the development of a novel scanning algorithm, SSA , in which the radius of a circular trajectory is constantly updated such that it follows a

spiral trajectory scanning all the cells. Due to the kinematic efficiency of near-circular trajectories, this algorithm achieves higher sampling rates than shortest path approaches, while retaining a relatively efficient coverage fraction in comparison to raster or resonance based frame-scanning approaches.

2.2 Introduction

Understanding information processing at the neural circuit scale is currently a major bottleneck to progress in understanding and treating brain disorders. To advance our understanding of neural circuit function, we need to densely and near-simultaneously sample the activity of large populations of neurons under controlled conditions. Calcium imaging by MPLSM is one of the most promising contender technologies, as it has the spatial resolution necessary to capture cellular processes, allows monitored cells to be precisely localised, and in some cases correlated with genetic markers, offers field of view sufficient to monitor hundreds or thousands of neurons, and has temporal resolution approaching that required to record individual action potential evoked calcium signals.

However, most MPLSM experiments currently utilise raster-based *frame scanning* strategies, which suffer from suboptimal sampling rates and poor photon counting efficiency, due to time wasted scanning extracellular space. This limits the number of cells from which spike trains can be accurately detected. Several improved scanning strategies have been developed, including inertialess scanning [Otsu et al., 2008], and beam splitting approaches [Cheng et al., 2011, Ducros et al., 2013]. These approaches both require substantial customisation of hardware. Most multiphoton microscopes are equipped with scanners based on GSs. Thus, the development of efficient strategies for galvanometric scanning of large neural populations at high sampling rate would enable widely available multiphoton microscopes to be deployed for the study of neural circuitry. A significant advance in galvanometric MPLSM was the recent development of the HOPS technique [Sadovsky et al., 2011], in which the TSA is applied to soma locations automatically extracted from a reference image, in order to minimize the

scanning path length. The performance advances over frame-scanning with such an approach can be substantial (Sadovsky et al reporting 1000 neurons at 8.5 Hz). However, neither this nor other previously developed fast scanning strategies [Lillis et al., 2008] [Nikolenko et al., 2007] take into account the inertia of the GSs themselves, and thus are likely to lead to sub-optimal sampling rates.

In this chapter, we propose a new scanning algorithm 'SSA' which drives the beam in radially modulated circular motions, resulting in a spiral trajectory fitted to pass through each detected soma. Due to the kinematic efficiency of near-circular motions, this new scanning strategy scales well to large neural ensembles, and produces sampling frequencies higher than those previously achieved. We demonstrate the application of the algorithm through a MATLAB model of the galvanometric scan head in a commercial MPLSM (Scientifica SliceScope).

2.3 Material and methods

2.3.1 GS mechanical model

GS can be included in the linear and invariant category of mechanical systems. This means that their behaviour in time is unchanged: $[X(t) \rightarrow Y(t)] \Rightarrow [X(t-T)] \rightarrow Y(t-T)]$ where X(t) is the entry value and Y(t) the corresponding output value of the system. It also means that this mechanical system follows the principles of homogeneity, additivity and superposition: $k_1X_1(t) + k_2X_2(t) \rightarrow k_1Y_1(t) + k_2Y_2(t)$ where $[k_1, k_2] \in \mathbb{R}$ are constants. Finally, for these categories of mechanical systems, the relation between the entry value $X(t)$ and the output value $Y(t)$ is given by an Ordinary Differential Equation (ODE) from the following type:

$$\sum_{i=0}^{i=n} a_i \frac{dY^{(i)}}{dt}(t) = \sum_{j=0}^{j=m} b_j \frac{dX^{(j)}}{dt}(t) \tag{2.1}$$

where $[a_i, b_j]_{(i,j)\in\mathbb{R}}$ are constant coefficients and $i \geq j$ considering that we have physical systems following the principle of causality. Two possible methods are available to get to the differential equation relating entry and output of the mechanical system. The first method consists of defining a model governed by the physical law (see figure 2.1), where the differential equation can be defined without knowing the entry and output signals of the systems. The second one is the identification method where the system is considered as a 'black box', the input signal is known, and by comparing the output of the black box to a 'catalogue' of outputs, the differential equation can be defined. Each ODE can then be associated with a transfer function which characterizes the mechanical system in the frequency domain.

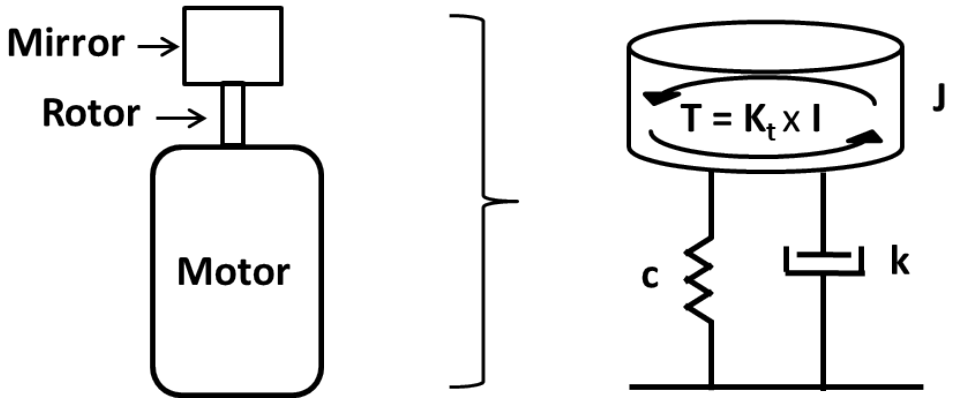


Figure 2.1: Simplified schematic representing the mechanical characterization of the GS.

GSs are defined by two main components: a moving magnet torque motor and a mirror rigidly attached to the rotor (see figure 2.1 and 1.4 A). Thus, it can be characterized by a mechanical system associated to an angular motion second order differential equation (see equation 2.2).

$$J\frac{d^2\theta}{dt^2} + k\frac{d\theta}{dt} + c\theta = K_t I \tag{2.2}$$

where J is the inertia of the equivalent rotor-mirror system, k the frictional constant, c the restoring constant and K_t the driving torque constant. I and θ denote the current applied to the motor and the angular position of the mirror, respectively. In order to measure k and c, we recorded a step response of the Model 6215H Optical Scanner (Cambridge Technology; see Fig. 2.2). We used Labview (NI Ltd) to control the angle of the mirror and acquired the

angular position output from the servo (MicroMax Model 671XX , Cambridge Technology). The step responses Fig. 2.2 to a 1 Volt input show an angular deflection of 2 degrees (output voltage 0.5V/degree). Table 2.1 shows the parameters estimated for our system. In this table, z is the damping factor, ω_n the natural frequency, $t_{r95\%}$ the 95% rise time of the system, $J = 5.6 \times 10^{-9}$ kg.m^{-2}, $K_t = 3.78 \times 10^{-3}$ N.m.A^{-1} being the same for both GSs. The total inertia J is calculated for the worst case scenario, taking the higher value of the recommended load (the mirror) from the data sheet. Our final GS conditional loop model is described in the block diagram shown in Fig. 2.3. The coefficients α_X and α_Y are estimated from an open loop simulation.

Table 2.1: Estimated galvanometer parameters

	k [kg.m$^2 s^{-1}$]	c [N.m.rad^{-1}]	z	ω_n [kHz]	$t_{r95\%}[\mu s]$
X	1.75×10^{-4}	2.04	0.82	19.1	161
Y	1.71×10^{-4}	2.26	0.76	20.1	152

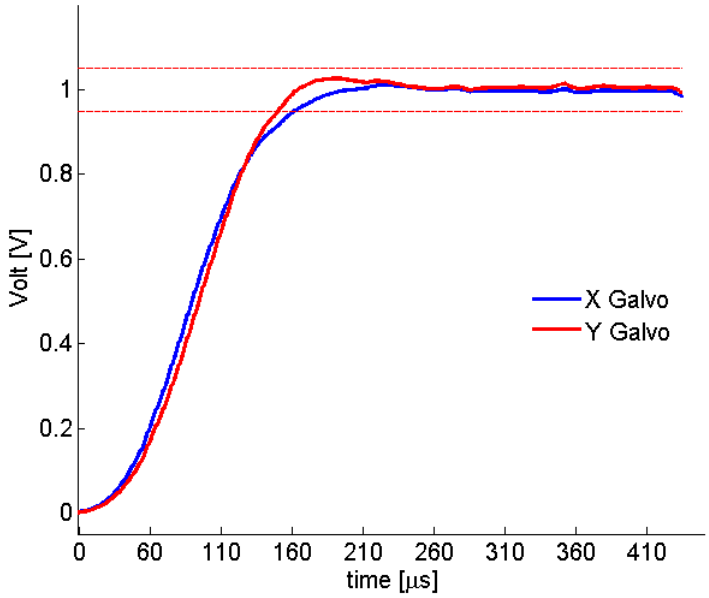


Figure 2.2: Step response of the Cambridge Technology Model 6215H Galvanometric Scanners.

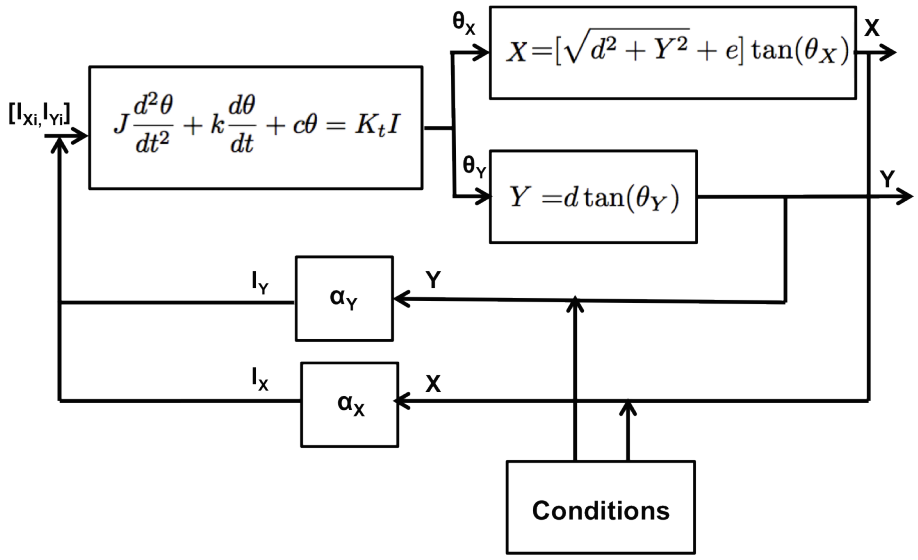


Figure 2.3: The GS model block diagram. $d = 0.15$ m denotes the distance from the centre of the Y mirror to the focal plane, and $e = 0.4$ m the distance between the X and Y mirror centres [Gerald F. Marshall, 2012].

2.3.2 Simulation of populations of neuronal calcium signals

In our simulation we generated surrogate data using the Izhikevich point neuron model [Izhikevich, 2003], driving the dynamics of a simulated GECIs with the dynamics of GCaMP6 [Chen et al., 2013] (see Fig. 2.4). The population consists of 80% excitatory and 20% inhibitory neurons. All of them were randomly interconnected with a synaptic current within [0, 0.5pA] for the excitatory neurons and within [-1, 0pA] for the inhibitory neurons. Each simulated neuron also received Gaussian synaptic noise ($\mu = 0$ pA, $\sigma = 0.5$ pA for excitatory neurons; $\mu = 0$ pA, $\sigma = 0.2$ pA for inhibitory neurons) representing the external thalamic input.

2.4 Results

We incorporated the two GS models described in Fig. 2.3 into the neuronal population simulation code, in order to test algorithms for finding a rapid laser path through randomly generated, pre-selected cell body locations.

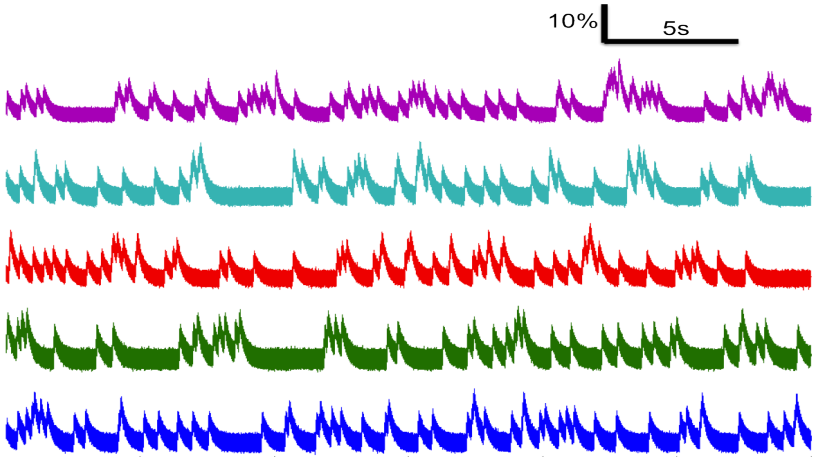


Figure 2.4: Neural ensemble simulation underlying the system model. Calcium dynamics of five simulated neurons (Izhikevich neuron model). Four of the neurons are excitatory regular spiking neurons and one is a fast spiking inhibitory neuron. Calcium transients are modelled as an AP-evoked ramp (45 ms) followed by a single exponential decay ($\tau = 150$ ms), following GCaMP6-like kinetics and coupled to a white Gaussian noise.

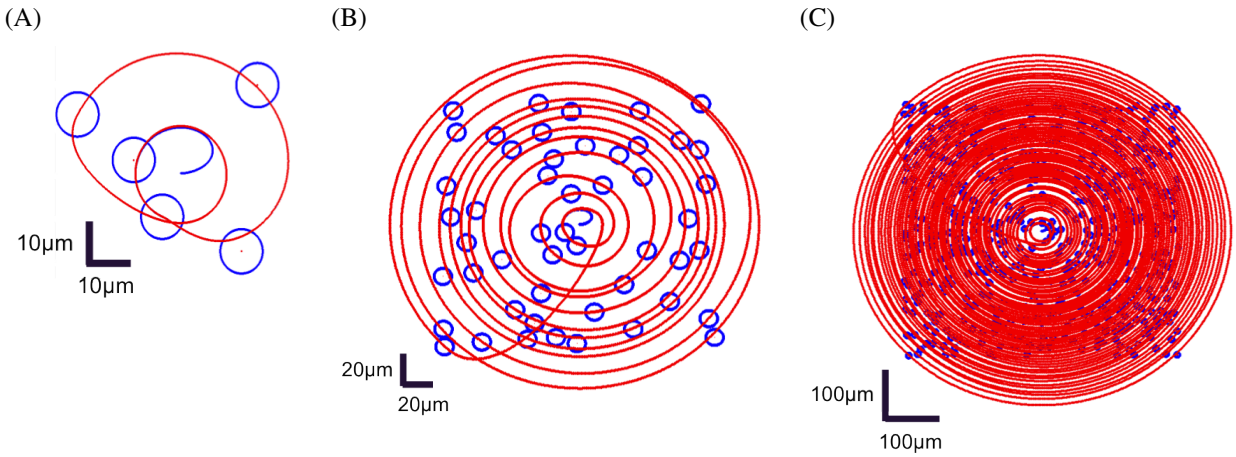


Figure 2.5: Improved fit of spiral trajectories through a pseudo-random population of neurons. (a), (b) and (c) represent five, fifty and five hundred cells, respectively, with the spatial density of active neurons in mouse V1 [Cossart et al., 2003]. The blue trace represents the laser path of the first cycle (starting in the centre of the FOV) and the red trace the laser path for all other cycles.

2.4.1 The SSA algorithm

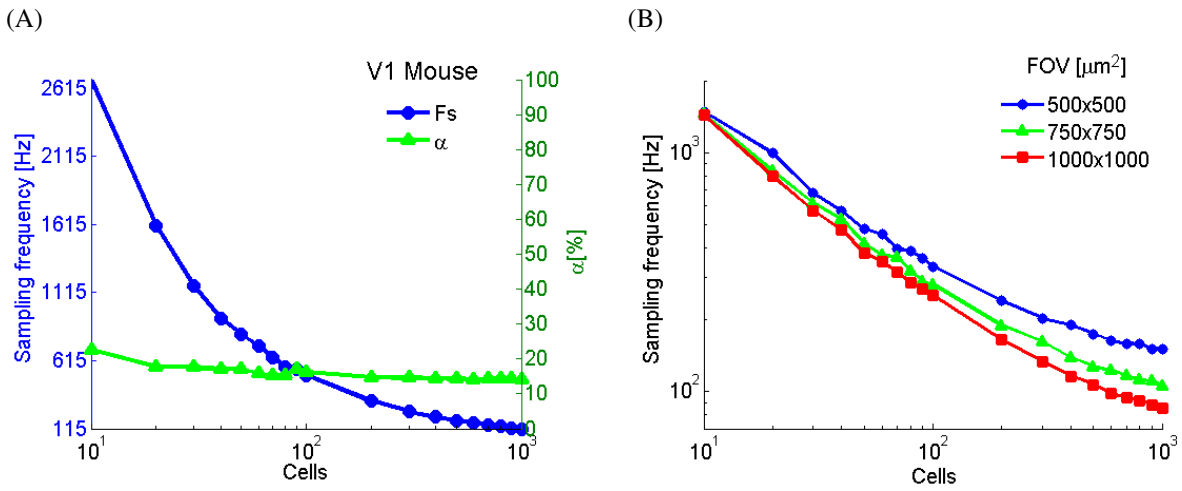


Figure 2.6: Sampling frequencies and useful signal ratio α achieved by the SSA algorithm. α is defined as the fraction of time the laser is focused on active neurons during each cycle (the laser scanned n_1 to n_N). (a) Sampling frequency achieved for spatial density of active neurons in mouse V1 (in blue) and associated α (in green). (b) Three different FOVs: 500×500, 750×750 and 1000×1000 μm^2. For each graph we averaged 5 different cell location configurations.

For inertial systems, smooth patterns (with moderate curvature) and continuous movements are well suited to provide acceleration-free travel [Kovacs, 2008]. The spiral scanning strategy is well known for imaging arrays and has already been applied to two-photon microscopy experiments [Goebel et al., 2007, Kampa et al., 2011]. We aimed to extend this by fitting a spiral trajectory to a specific set of points, after an initial frame-scan to determine soma locations. In order to reduce the impact of inertia (i.e the transient acceleration period, see Fig. 2.2) in the system, both GS are driven at a constant angular speed. This results in circular movements. It is then possible to sample all the cells through an algorithm that modulates the radius of the circular trajectories resulting in a distorted spiral pattern.

Algorithm description (pseudo-code):
For a randomly distributed neuron population $\{n_1, n_2, ..., n_N\}, N \in \mathbb{N}^*$ in a certain FOV, $\forall(i, j) \in N$:

(i) Sort the neurons by their ascending radius r_i to the centre of the FOV.

(ii) For neuron n_i apply a sinusoidal current (I_{Xi}, I_{Yi}) to both GS to drive the laser beam in a circular motion with radius r_i

(iii) While scanning circle r_i,

for all the n_j with $r_j > r_i$

if laser scans with sufficient sample n_j

indx = indx+1

if laser scanned n_i

i = i+indx

(iv) back to (ii)

(v) if scan $n_N -> $ go back to n_1

The geometrical conditions used in this algorithm are fed into the model (Fig. 2.3). At each instance, the radius of the circular trajectories is modulated. Although the impact of inertia is still present, it is reduced by allowing multiple cells to be scanned in a single period. For one cycle (the laser scanned n_1 to n_N), the number of periods (360 degree rotations) is less than the number of cells. In (iii), the number of sufficient samples can be defined by the user for the neurons that are traversed en passant. Using a driving frequency of $\omega_I = 10$ kHz and a FOV of 750×750 μm^2 we performed several simulations with different cell densities (see Fig. 2.6(b)) . With these parameters we achieved sampling frequencies as high as 475 Hz for 50 Cells and 105 Hz for 1000 cells. This suggests that the SSA approach could potentially achieve sampling frequencies higher than those achieved by previously documented scanning approaches.

2.4.2 Signal Acquisition

During signal acquisition, a matrix is collected, with columns containing the photomultiplier output binned throughout each cycle (see Fig. 2.7). To demonstrate the system working, the Izhikevich neuron simulation was applied (with calcium dynamics) described in Fig. 2.4. In this example, the FOV was 500×500 μm^2 for five neurons, allowing a sampling rate of 5 kHz, well above the level required to faithfully reconstruct calcium dynamics.

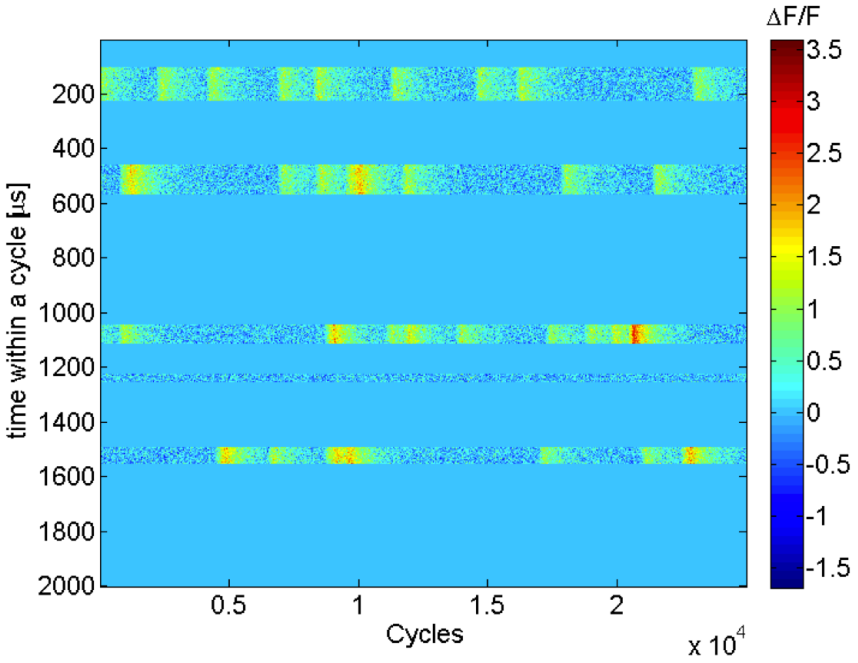


Figure 2.7: Acquisition matrix for a 5 neuron population. Time series are extracted by collecting and averaging rows in which the laser is over the same neuron.

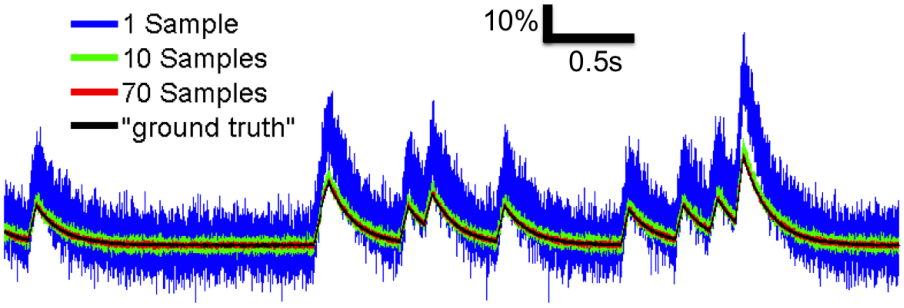


Figure 2.8: Recorded fluorescence ($\Delta F/F$) from a simulated excitatory neuron, demonstrating that, at least in simulation, the system is capable of faithfully reproducing calcium dynamics.

2.5 Discussion

We developed a novel galvanometric scanning algorithm for two photon laser scanning microscopes, SSA. The algorithm has a number of advantages over traditional frame-scanning approaches to galvanometric scanning, yielding both higher sampling rates and a higher proportion of time spent counting photons from structures of interest. This indicates that it should allow spike trains to be reconstructed from a larger population of neurons (for a given detection accuracy), or with better spike detection accuracy (for a given number of neurons) than would be possible with frame-scanning. It also achieves higher sampling rates than path minimisation approaches such as HOPS [Sadovsky et al., 2011], although at the expense of fraction of time spent over neurons, as the latter method uses a 'stop start' approach that allows dwelling over individual neurons in order to increase photon count. The effect of this compromise on spike train detection accuracy [Onativia et al., 2013] remains to be studied.

One disadvantage of linescanning techniques including the approach presented here is that they may be quite vulnerable to movement artefact, being unable to take advantage of image registration techniques to correct for motion artefacts. This may prove to limit the number of cells to which the algorithm can be scaled *in vivo*. The algorithm was tested by simulating the GSs in a commercial multiphoton microscope, with parameters measured experimentally from galvanometric step responses. Validation of the algorithm *in vitro* and *in vivo* is the focus of ongoing work. If validated experimentally, the algorithm could be expected to enhance the number of cells that can be recorded, and the temporal resolution of functional imaging, using standard, off-the-shelf two photon microscope hardware.

2.6 Acknowledgements

We thank Alex Murray of Scientifica Ltd for useful discussions on galvanometric scanning technology.

2.7 Future work

In the next chapter, I will use the SSA algorithm to record functional signals in mouse brain slices. However, prior to this study, I needed to test the second order model on the GS hardware (see Fig.2.1 and Fig.1.4). I tried to apply sine voltages to the GSs and sweep through various amplitude and frequency values for dynamic behaviour characterization according to the second order model. I found that the analogue close loop servo control board Micromax671XX (see Fig.1.4 B) triggered a 'safe mode' which momentarily stopped the current accessing the GS for a sine wave exceeding a certain amplitude/frequency threshold couple. However, repeatedly triggering this safe mode is risky as it might damage permanently the system (our GS broke by repeating this experiment over and over). Hence, I could only collect sporadic values of these limited amplitude/frequency couples, e.g $V_{pp} = 2$ V (corresponding to a 300 μm sweep) and $\omega_I = 1$ kHz. The few collected values tended to show that the close loop Micromax board will limit the SSA algorithm to be driven with sine voltages at $\omega_{Imax} = 1$ kHz. Even considering this limiting factor, I show in the next chapter how the SSA performs when compared to the TSA.

In the future, a collaboration with the enterprise Cambridge Technology would enable the incorporation of a close loop model in our GS simulation. This complete model, if linear, could be used with optimal control theory to approach a close to optimal solution for 2D functional calcium imaging scanning trajectories. Another approach would consist in replacing the Micromax671XX by developing a new PID controller suited for the SSA scanning algorithm.

Chapter 3

Fast functional calcium imaging with 2D scanning strategies

3.1 Abstract

Objective: Multi-photon laser scanning microscopy provides a powerful tool for monitoring the spatiotemporal dynamics of neural circuit activity. It is, however, intrinsically a point scanning technique. Standard raster scanning enables imaging at subcellular resolution; however, acquisition rates are limited by the size of the field of view to be scanned. Recently developed scanning strategies such as Travelling Salesman Scanning (TSS) have been developed to maximize cellular sampling rate by scanning only regions of interest in the field of view corresponding to locations of interest such as somata. However, such strategies are not optimized for the mechanical properties of galvanometric scanners. We thus aimed to develop a new scanning algorithm which produces minimal inertia trajectories, and compare its performance with existing scanning algorithms.

Approach: We describe here the Adaptive Spiral Scanning (SSA) algorithm, which fits a set of near-circular trajectories to the cellular distribution to avoid inertial drifts of galvanometer position. We compare its performance to raster scanning and TSS in terms of cellular

sampling frequency and signal-to-noise ratio (SNR).

Main Results: Using surrogate neuron spatial position data, we show that SSA acquisition rates are an order of magnitude higher than those for raster scanning and generally exceed those achieved by TSS for neural densities comparable with those found in the cortex. We show that this result also holds true for *in vitro* hippocampal mouse brain slices bath loaded with the synthetic calcium dye Cal-520 AM. The ability of TSS to ”park” the laser on each neuron along the scanning trajectory, however, enables higher SNR than SSA when all targets are precisely scanned. Raster scanning has the highest SNR but at a substantial cost in number of cells scanned. To understand the impact of sampling rate and SNR on functional calcium imaging, we used the Cramér-Rao Bound on evoked calcium traces recorded simultaneously with electrophysiology traces to calculate the lower bound estimate of the spike timing occurrence.

Significance: The results show that TSS and SSA achieve comparable accuracy in spike time estimates compared to raster scanning, despite lower SNR. SSA is an easily implementable way for standard multi-photon laser scanning systems to gain temporal precision in the detection of action potentials while scanning hundreds of active cells.

3.2 Introduction

There has been extensive development of new optical neuroimaging techniques in the last two decades. Since the emergence of multi-photon laser scanning microscopy (MPLSM) in the 1990s [Denk et al., 1990, Chris Xu, 1996], synthetic and genetically encoded calcium fluorescent indicators [Chen et al., 2013, Tada et al., 2014] have been used *in vitro* and *in vivo* to monitor the activity of 10s to 1000s of neurons at subcellular resolution [MacLean et al., 2006, Kampa et al., 2011, Cossart et al., 2003], typically by galvanometric scanning of a point focus throughout the tissue. However, the point scanning nature of this technique limits temporal resolution, and this becomes more pronounced with an increasing number

of scanned cells. An important goal of large-scale two photon calcium imaging is to extract time-series signals from as many cells as possible, with sufficient signal to noise ratio (SNR) to detect action-potential induced calcium transients, and sufficient sampling rate to detect calcium transient onset time accurately. There is thus, the need to develop methods which maximise the cell count, sampling rate, and SNR, subject to the trade-offs between these quantities.

The bandwidth limitations of galvanometric scanning systems have motivated the development of inertialess scanning microscopes based on acousto-optic deflectors, and scanless microscopy systems [Schultz et al., 2017]. However, such technology adds considerable complexity to a microscope, and cannot easily be retrofitted into legacy multiphoton microscopes. Resonant scanning galvos allow for increased sampling rates. However, as they still spend much time scanning non-interesting regions of tissue, SNR, which depends on the number of photons collected from structures of interest, suffers. Here, we study the performance of scanning approaches that allow sampling of targeted regions of interest (ROIs) and which can be used with standard, commercial two photon microscope hardware, provided that the microscope software provides the capability to drive the galvos along a pre-defined trajectory.

To increase temporal resolution in galvanometric MPLSM, one strategy is to direct the focus from one target cell to the next along a shorter targeted scanning path, avoiding sampling uninteresting regions of tissue. One implementation of such a strategy, Targeted Path Scanning (TPS) [Lillis et al., 2008], was used to achieve sampling rates of 100 Hz with single action potential (AP) sensitivity, while scanning individual neurons sparsely distributed over the entire hippocampus of a juvenile rat (> 1.5 mm). More recently, Sadovsky *et al.* [Sadovsky et al., 2011] introduced the Heuristically Optimal Path Scanning (HOPS) algorithm. In this approach, the Travelling Salesperson Problem is solved to find the shortest path between all ROIs. In this paper, we refer to Travelling Salesperson Scanning (TSS) algorithms generically (with HOPS being the specific implementation in [Sadovsky et al., 2011]). With TSS, the fraction of time spent scanning ROIs can be increased from around

4% to 40% when compared to raster scanning, achieving sampling frequencies of 150 Hz for a population of 50 neurons in the somatosensory cortex [Sadovsky et al., 2011].

However, as galvanometric mirrors are inertial systems, they cannot be driven above a certain speed; otherwise, they fail when scanning sharp turns in the trajectory. Motivated by this, we have developed the Adaptive Spiral Scanning (SSA) algorithm, first reported in [Schuck et al., 2014], and described in more detail here. SSA is based on a simple galvo model, and fits a set of near-circular trajectories to the somatic locations of a population of neurons. In [Schuck et al., 2014], we demonstrated by simulation that high sampling rates can be achieved with minimal-inertia trajectories for typical neural densities found in the visual cortex, somatosensory cortex and hippocampus. In this paper, we present a full description of the implementation of this system, validate the approach by simultaneously performing whole cell patch clamp electrophysiology with two photon scanning of hippocampal and cortical brain slices, and compare its performance with TSS, as well as raster scanning.

To compare signal quality between different scanning strategies, we employ a new (in this context) procedure: calculating the Cramer-Rao Bound (CRB) [Hammersley, 1950, Chapman and Robbins, 1951] of the uncertainty in the AP onset time, given the sampling rate (f_s) and SNR of the analyzed time series, and the electrophysiological recorded "ground truth" signal. This metric allows us to demonstrate the effect of varying f_s and SNR, through manipulations of the two photon scanning path employed, on precisely transcribing the activity of large neural networks.

3.3 Material and methods

3.3.1 Path generation for targeted scanning strategies

Scan paths were generated in MATLAB (Mathworks Ltd), and tested with a standard MPLSM (SliceScope, Scientifica Ltd) (i) on purely simulated neuron location distributions,

(ii) on real ROI distributions corresponding to neural somas from raster-scanned slices, but applied "offline", and (iii) on real brain slices. For two-dimensional (2D) simulated neurons, cell centers were assigned to a uniform distribution of random positions in a circular field of view (FOV) of 300 μm diameter with the condition that cells cannot be superimposed. Scan paths were generated with the TSS and SSA algorithms for distributions of 50, 100, 150, 200 and 250 cells (cell radius 7 μm). When comparing the three different scanning algorithms, raster scanning was performed first (as this was used to localise cell bodies), and then TSS and SSA were randomly interleaved, to avoid any systematic effects due to bleaching. For real neuron distributions, we segmented the calcium movies using a semi-automated algorithm based on user input and on the temporal profile of the pixels. First, we apply temporal edge detector and binary thresholding on a spatially down-sampled movie to individual Points Of Interest (POIs). We then use the k-means algorithm to classify these POIs as putative neurons or noise based on the similarity between their temporal activity and a stereotypical calcium transient profile. Finally, for each of the POIs labelled as putative neurons, we compute the average time signals and segment the original calcium movie based on the correlation map with such signal, obtaining ROIs. We only keep those ROIs whose shape and size belong to a biologically plausible range. For some of them (depending on how conservatively we set the algorithm parameters), we also ask for feedback from the user before definitively selecting them as neurons. At the end of this procedure, the final result is shown in a graphical user interface in MATLAB where the user can select additional neurons manually. The ROI centers were then fed into the TSS and SSA algorithms to generate the appropriate scanning path. Scan paths were then uploaded into the Labview-based program *SciScan* (Scientifica Ltd), which controlled the MPLSM, and were tested at varying f_s and target dwell times. The positions of the galvanometric mirrors (Model 8315Kl, Cambridge Technology) were recorded using an electronic position feedback circuit (Micromax 671xx, Cambridge Technology) allowing us to determine the actual path traversed by the laser, and the number of targets hit or missed. MATLAB code for the TSS and SSA algorithms, and details on how to use them in conjunction with *SciScan* are available at http://www.github.com/schultzlab/scanning.

Adaptive Spiral Scanning:

The SSA algorithm is implemented in MATLAB, as part of a simulation platform for MPLSM scanning algorithms [Schuck et al., 2014]. The algorithm inputs are a set of cell soma locations. The first step of the SSA algorithm consists of sorting cell locations by ascending radius r_i from the center of the FOV. Subsequently, the path generation of the SSA algorithm is based on this ordering of cell locations, and on the numerical integration of a linear, second order, Ordinary Differential Equation (ODE) that approximates the mechanical behavior of galvanometric scanners (GS) [Schuck et al., 2014]. In our linear GS model, the driving force is a current that rotates the rotor and therefore, controls the precise angle of the GS mirror. Consequently, driving two GSs with two sine waves results in driving the focal point of the MPLSM in a circle, minimizing the impact of the inertia on the scanning system. The SSA algorithm is initiated by integrating the ODE with two sine waves applied to both GSs with an amplitude corresponding to the radius r_1 of the first cell to be scanned. The radius of the scanned circle is then updated after the first cell location is visited with a number of samples defined by the user. After every cell location visit, the radius index is incremented by a scalar j satisfying the equation $r_k = r_i + r_j$ where k is the new radius index, i the current radius index of the scanned cell and j the number of neurons scanned (with a sufficient number of samples) while scanning circle i. If $k = N$ where N is the number of cell locations and all the cells have been scanned, then $r_k = r_1$ and a new cycle starts.

Travelling Salesman Scanning:

In our implementation of travelling salesperson scanning, we followed in most respects the HOPS algorithm developed by Sadovsky *et al.* [Sadovsky et al., 2011]. The TSS algorithm also starts with ordering of scanning locations. To find a near-optimal solution to the shortest path between cells, we used open source genetic algorithm travelling salesperson code, *tsp_ga.m*, written by Joseph Kirk, and made available via http://www.mathworks.com/matlabcentral. This code computes a near optimal solution to the shortest path between all the locations to

be scanned, with the condition that each location is only scanned once. After the locations to be scanned have been ordered, we applied current steps to both galvanometric scanners (GSs) and sampled the trajectory by integrating the ODE characterizing the mechanical behavior of the GSs. Finally, in the TSS computer path generation, we added a condition that enables the user to choose a fixed number of samples per visited ROI. This allows the galvos to be driven as fast as possible from one cell to another while enabling the user to adjust the dwell time over the target depending on the type of dye used, the inertia of the path and the required SNR for the experiment. The user has, however, to bear in mind that GSs are inertial, inducing a slight delay towards reaching their imposed location. It is therefore necessary to choose a number of samples that allows all the ROIs - even those located on sharp turns - to be reached and sampled with a sufficient amount of time. One TSS scanning cycle is achieved when all the cell locations have been successfully scanned.

3.3.2 In-vitro cell loading of hippocampal slices with calcium indicator dyes

All animal experiments were performed under institutional guidelines and were approved by the Home Office (UK) and were in accordance with the UK Animals (Scientific Procedures) Act 1986 and associated guidelines. Juvenile wild-type mice (C57Bl/6 P13-P21) were anaesthetized with isoflurane. Depth of anaesthesia was assessed by loss of pedal withdrawal reflex prior to decapitation procedure. Brain slices (400 μm thick) were horizontally cut in 1-4°C oxygenated (95% O2, 5% CO2) slicing artificial cerebro-spinal fluid (sACSF, containing in mM: 0.5 $CaCl_2$, 3.0 KCl, 26 $NaHCO_3$, 1 NaH_2PO_4, 3.5 $MgSO_4$, 123 sucrose, 10 D-glucose) using a ceramic blade (Camden instrument 7550/1/C), with the vibratome (7000smz, Camden Instrument) adjusted to the following parameters: $\Delta z < 3\mu$m, horizontal slicing frequency 80 Hz and slicing speed 0.06 mm/s. Slices containing the trisynaptic loop of the hippocampus were taken and allowed to rest in oxygenated recovery ACSF (rACSF, containing in mM: 2 $CaCl_2$, 123 NaCl, 3.0 KCl, 26 $NaHCO_3$, 1 NaH_2PO_4, 2 $MgSO_4$, 10

D-glucose) for 30 min at 37°C. Subsequently, the hippocampal slices were incubated and "painted" for 30 min at 37°C in a dark oxygenated chamber containing the following solution: 2.5 mL rACSF, 50 μg Cal-520 AM (AAT Bioquest), 2 μL Pluronic-F127 20% in DMSO (Life Technologies) and 48 μL DMSO (Sigma Aldrich). Slices where then washed in rACSF at room temperature for 30 min before being transferred to the recording chamber.

3.3.3 Two-photon imaging and electrophysiology

Imaging was performed using a standard commercial GS based two-photon microscope (SliceScope, Scientifica Ltd) coupled to a mode-locked Mai Tai HP Ti:S laser system (Spectra-Physics) operating at 810 nm with pulse width of 100 fs at 80 MHz. A 40×, 0.8 NA water immersion objective was used to locate the dentate granule cells (DGCs) or the nearby entorhinal cortex under oblique illumination. Individual cells were filled through the patch pipette (R = 3 to 6 MΩ) with intracellular solution containing in mM: 130 K-gluconate, 7 KCl, 10 HEPES, 4 ATP-Mg, 0.3 GTP-Na, 10 phosphocreatine-Na, 0.1 Cal-520 potassium salt (AAT Bioquest) and 0.1 Alexa-594 (Molecular Probes). We allowed the calcium dye to diffuse into the cell for 10-30 min, after which we evoked APs in the patched cells by applying current steps while simultaneously recording membrane potential and obtaining two-photon calcium images. Whole-cell current clamp recordings were performed with a MultiClamp 700B using WinWCP 5.2.0 (University of Strathclyde) while two-photon images were acquired using the Labview based software *Sciscan* associated with the commercial microscope. Imaging power at the specimen did not exceed 15 mW.

3.3.4 Assessing the quality of scanned signals

Having presented three different scanning algorithms: raster scanning, TSS and SSA, each of which can be run at different sampling rates, subject to overall physical limitations, it is essential to compare the quality of the signals sampled. There are two aspects to signal quality that we considered. The first is the overall SNR defined as A/σ, where A is the

peak amplitude of a single calcium transient and σ is the standard deviation of the noise. The standard deviation of the noise of each trace was estimated as the sample variance in a region of length 5 s (2100 samples) in which no spikes were detected. We estimated the peak amplitude as the value of A that minimized the mean square error between acquired time series with the MPLSM and the times series resynthesized from the pulse model using known AP times from the electrophysiological signal. However, the SNR does not uniquely determine the usefulness of the signals produced; for instance, if one wants to precisely determine the time of occurrence of a set of events (such as calcium transient onsets), it is advantageous to have high f_s, whereas a lower f_s might be tolerated if all that is needed is to detect the presence or absence of an event. We analyzed the trade-off between SNR and f_s by taking a second, complementary measure of signal quality: the CRB of the mean squared error in estimating the time of occurrence of an action potential from fluorescence calcium imaging data. This bound gives us the best case scenario for uncertainty in spike time estimation for a given SNR and f_s. We calculated the CRB as

$$CRB(t_0) = \frac{\sigma^2}{\bar{A}^2}\left[\sum_{n=0}^{N-1}\left(\alpha e^{-\alpha(nT-t_0)} - \gamma e^{-\gamma(nT-t_0)}\right)^2 \times u(nT-t_0)\right]^{-1} \tag{3.1}$$

where t_0 is the spike time, determined by whole cell recordings; σ is the standard deviation of the noise; N indicates the number of samples in the time series, and $T = 1/f_s$. u is the indicator function where $u(nT-t_0) = 0$ for $nT - t_0 < 0$ and $u(nT-t_0) = 1$ for $nT - t_0 \geqslant 0$, $\bar{A}$ is the normalized pulse amplitude and parameters α and γ determine the rise and decay times of a single calcium transient, with $e^{-\alpha t}$ reflecting the speed of decay and $\left(1 - e^{-(\gamma-\alpha)t}\right)$ reflecting the speed of the rise. Parameters $\alpha = 3.18\,\mathrm{s}^{-1}, \gamma = 34.49\,\mathrm{s}^{-1}$ were estimated from the rise and decay times in [Tada et al., 2014]. Further details of the CRB derivation are provided in the Appendix.

3.4 RESULTS

Both high temporal resolution and SNR are important in order to faithfully transcribe spike trains from the calcium traces of recorded neurons. An important aim of our experiments was, thus, to compare these criteria for raster scanning, TSS and SSA applied to two dimensional scanning for *in vitro* slice experiments.

3.4.1 Minimal inertia scanning paths enable fast and precise functional calcium imaging

Calcium transients can be detected when the laser is focused on a neuron while its internal calcium is elevated following an AP. In our *in vitro* experiments we used the synthetic calcium dye Cal-520, which has a rise time of < 70 ms and a decay time constant of < 800 ms for a single AP [Tada et al., 2014]. In an FOV of $300 \times 300\,\mu\text{m}^2$, the sampling frequency achieved by raster scanning is about 3 Hz. Although higher temporal resolution can be achieved, it comes with a substantial reduction in the FOV, and thus, the number of cells that can be sampled. In contrast, targeted 2D line-scanning strategies such as TSS and SSA allow calcium transient detection from a much larger FOV at the same sampling frequency (and for the same FOV, allow higher sampling frequencies and better signal reconstruction) . To compare the sampling frequencies of these scanning strategies under well-controlled experimental conditions, we simulated the somatic locations of a random population of cells (drawn from a spatial distribution approximately the same as that of layer 2/3 of mouse primary visual cortex [Cossart et al., 2003]), and scanned these locations with the two photon microscope (Fig. 3.1a-d).

Employing TSS on a simulated population of 200 cells in a $300 \times 300\,\mu\text{m}^2$ area showed that for this (typical) instance of random cell positions, the highest cellular sampling rate f_s allowing the galvos to follow the command voltage and hit all desired targets was 51 ± 7.4 Hz (Fig. 1a). Any increase of f_s above this value resulted in missed cells, due to the

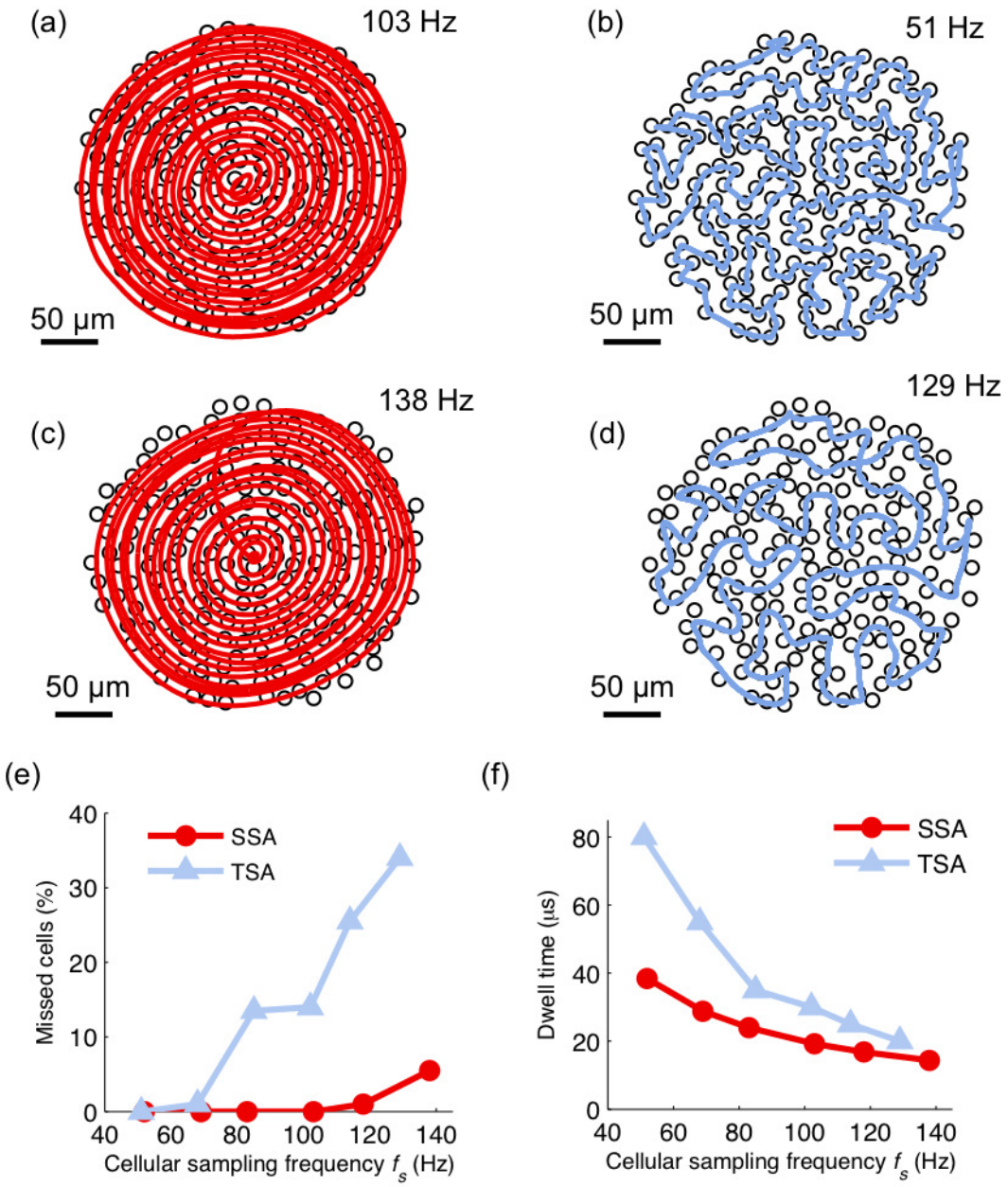


Figure 3.1: Spiral scanning yields lower cellular miss rates, but travelling salesperson scanning higher SNRs, for the same somatic locations. (a) Recorded galvo positions for one full path of SSA for 200 neurons at $f_s = 103$ Hz (all cells are scanned). (b) TSS path for the same neural population in *a*, but with a scan rate of 51 Hz, the maximum for which all targets were visited. (c) SSA scanpath at 138 Hz, with 11 targets now missed. (d) TSS scanpath for the same population, with neuron sampling rate increased to 129 Hz. At this rate, 65 cells were missed. (scale bar 50 μm for *(a)*, *(b)*, *(c)* and *(d)*. (e) The fraction of target cells missed for increasing f_s with the same soma locations as above. (f) The average time spent collecting photons from each ROI, for the SSA and TSS paths as a function of increasing f_s. Increasing value on the y-axis indicates greater SNR in the resulting time series signals.

system not being able to follow precisely the desired trajectory (Fig. 1b). Performing a similar assessment on the same neuronal locations for SSA shows that all the targets can be hit at sampling rates up to 103 ± 6.7 Hz, almost double the maximum f_s for TSS (Fig. 3.1c). In general, the number of missed cells is lower for SSA compared to TSS (Fig. 1e). However, at any given sampling frequency f_s, the microscope spends more time collecting photons from ROIs per sample under TSS (Fig. 3.1e). This quantity is essentially a measure of the SNR for the resulting time series, and thus, it appears that TSS can be advantageous when maximising sampling rate is not the most important criterion. In the experiment above, the neural density was 2200 neurons/mm^2. In general, higher sampling rates for SSA (in comparison to TSS) were achieved for target densities exceeding 1400 neurons/mm^2 (Fig. 3.2a-d). Automated cell contour detection in mouse somatosensory and visual (V1) cortex from *in vitro* MPLSM high resolution images shows neural densities around 3100 cells/mm^2 and 2100 cells/mm^2, respectively [Cossart et al., 2003, Sadovsky et al., 2011]. This suggests that when dense sampling of neurons is required, higher sampling rates are achievable using SSA. It should be noted that in some cases, labelling may be sparse (eg. due to use of a cell-type selective promoter), so this provides an upper limit on target density. The dwell time advantage of TSS can be seen to apply regardless of neuronal density (Fig. 3.2e).

To further validate and characterise the performance of the algorithms, we performed *in vitro* two photon imaging experiments in mouse hippocampal brain slices bath-loaded with the calcium dye Cal-520 AM, as described in Methods. Figure 3.3a shows the dentate gyrus of such a bath-loaded slice. This area, which is densely packed with granule cells, provides an excellent testbed for the platform. We used an initial raster-scan, together with semi-automated cell body localisation (see Methods), to locate individual granule cells that were either spontaneously active or electrically driven during the raster-scan (cyan discs in Fig. 3.3b). In this particular image, 137 cells were extracted within a FOV of $180 \times 180\,\mu$m^2 (corresponding to a density of $\sim$4200 cells/mm^2). TSS allowed scan rates (inverse of time to cover one full cycle back to the same location) of up to 88 Hz before the path started missing ROIs (Fig. 3.3b shows the path at 88 Hz) Applying the SSA algorithm, we generated a spiral

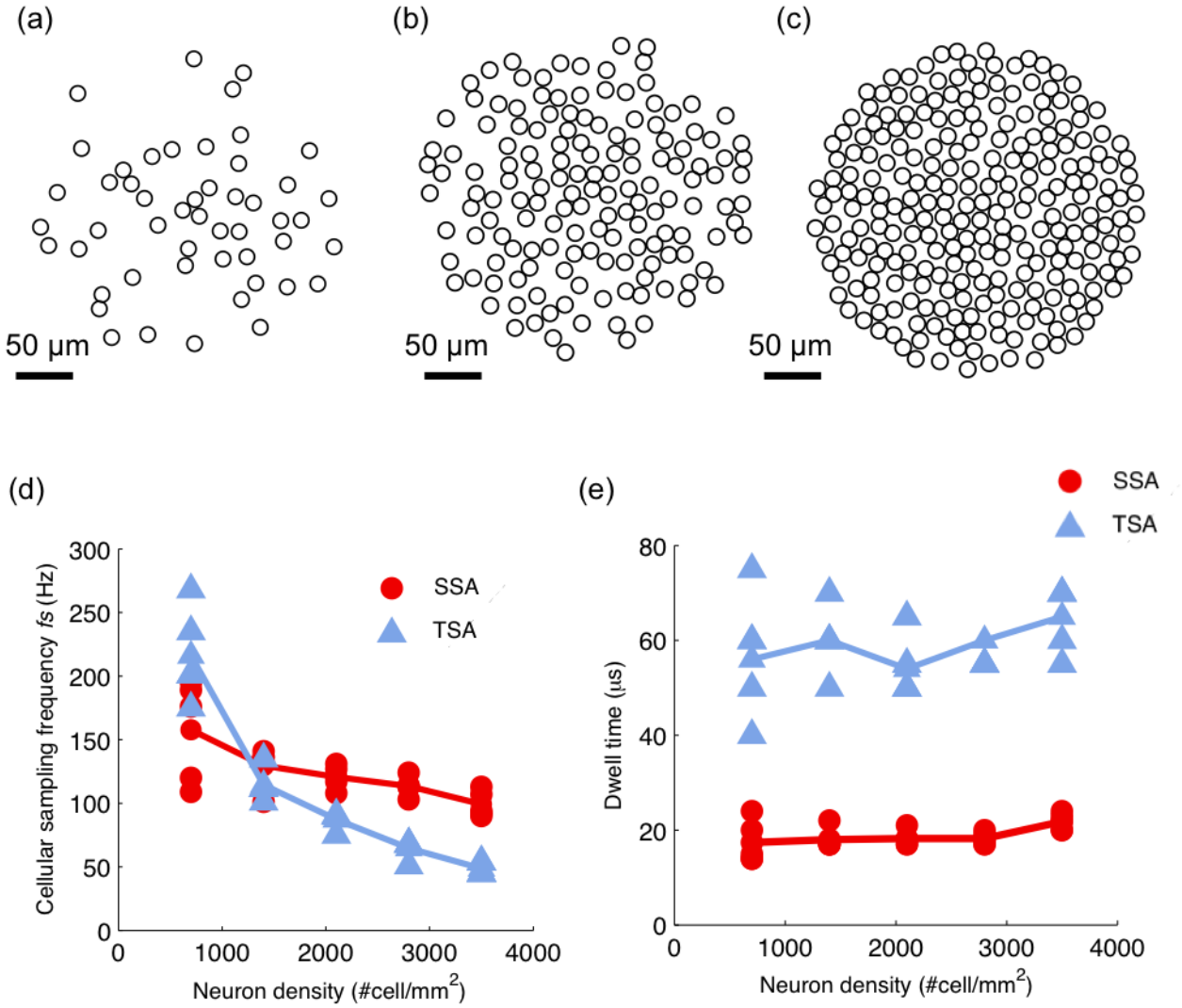


Figure 3.2: Sampling frequency and dwell time achievable for the TSS and SSA algorithms. (a)-(c) Exemplar spatial distributions of cells (uniformly distributed within a circle of diameter 300 μm), for a total cell count of 50 (*a*), 150 (*b*) and 250 (*c*) cells . These examples correspond to densities of 700, 2100 and 3500 cells/mm^2, respectively (scale bar 50 μm for *(a)*, *(b)* and *(c)*). (d) The maximum sampling frequency at which all the targets are hit, for TSS and SSA across different neuronal densities (each cell density was tested on five different geometric cell arrangements). (e) Average dwell time over the target across the same neural distributions as used in *(d)*.

trajectory which passed through all cell bodies at sampling rates up to 117 Hz (Fig. 3.3b shows the 117 Hz path). For lower cell densities, however, we found that often TSS would reach higher sampling rates than SSA before missing cells. For instance, at a density of 50 cells per $180 \times 180\,\mu m^2$ (1500 cells/mm^2), SSA was able to reach 165 Hz, whereas TSS was able to reach 208 Hz (Fig. 3.3d). Both scanning algorithms yield high quality calcium transient recordings (Fig. 3.3e,f).

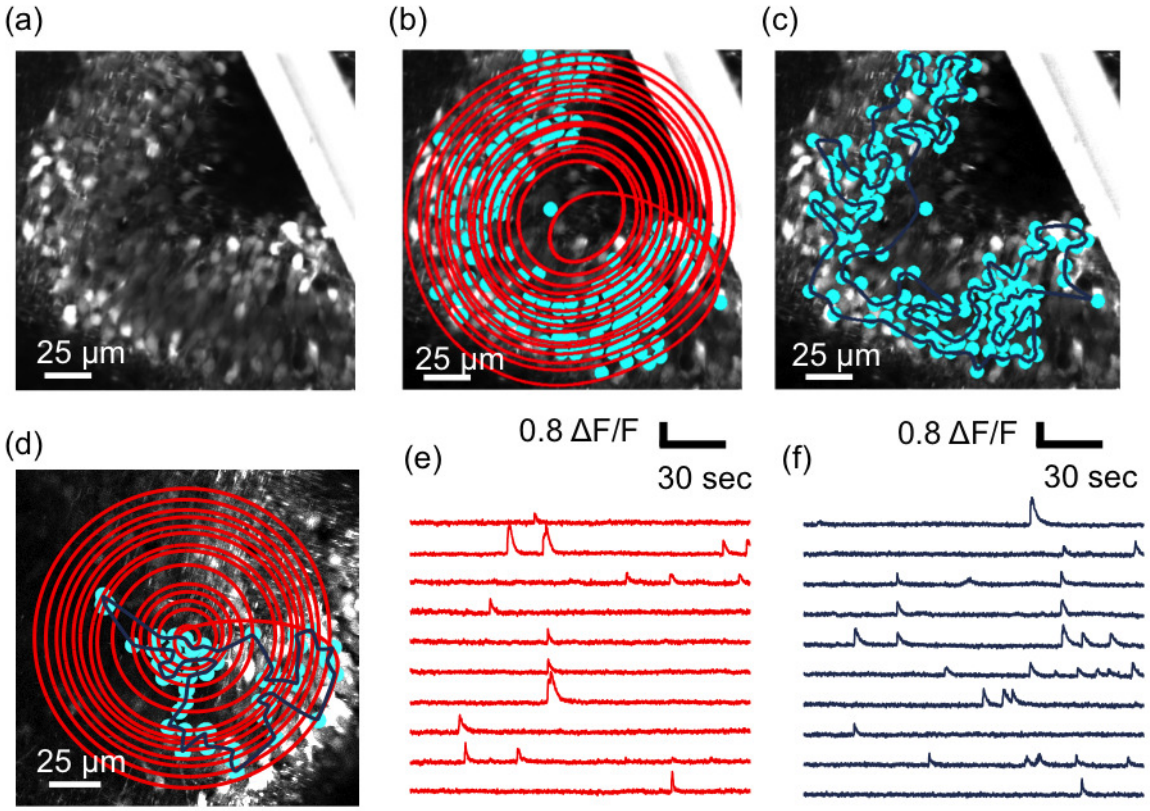


Figure 3.3: Scanning patterns for fast acquisition of calcium signals. (a) Raster-scanned image of dentate granule cells used to locate targets for scanning. (b) 137 ROIs (in cyan) are shown overlaid, indicating granule cells that were spontaneously active or electrically activated during raster-scanning for target acquisition. The overlaid dark blue trace indicates the recorded galvo trajectory for the highest f_s (88 Hz) at which TSS is able to hit all targets. (c) Overlaid SSA path (red), at maximum f_s (117 Hz) to hit all targets. (d) Frame-scanned image of dentate granule cells with 50 ROIs (in cyan) overlaid with scanning paths for maximum f_s for TSS (208 Hz, dark blue) and SSA path (165 Hz, red), scale bar 25 μm for *(a)*, *(b)*, *(c)* and *(d)*. (e) Spontaneous activity acquired from 10 (of 50) granule cells with TSS at 208 Hz (traces 40-point median filtered for visualization only). (f) Spontaneous activity traces from the same granule cells acquired with SSA at 165 Hz (traces 50 point median filtered to match temporal regularisation in *(e)*).

Missed targets can be seen at sharp turn locations in the TSS trajectory, indicating that the inertia of the galvanometric scanners do not allow them to sharply change direction above a certain speed. To examine this further, we segmented 50 ROIs corresponding to spontaneously active dentate granule cells in $180 \times 180\,\mu m^2$ and scanned them with TSS at f_s rates ranging from 166 Hz to 885 Hz (Fig. 3.4a,b). Consider the scanned granule cell encircled in orange in Figure 3.4b: the target ROI is just grazed for $f_s = 425$ Hz, and is missed entirely above this scanning frequency. The recorded time series for this example is shown in Figure 3.4c (no median filtering). At 885 Hz, no functional signal was visible, as the scanpath did not intersect with the ROI. More of the functional signal is retrieved at 425 Hz and 166 Hz when 36 μs and 122 μs, respectively, were spent collecting photons per cycle (dwell time). Note that in TSS the dwell time can be artificially increased by causing the focus to stop for a period in the centre of the cell. This, however, comes with a substantial penalty in terms of sampling rate.

3.4.2 Signal quality

SNR dependence upon scanning strategy.

We saw in section 3.4.1 that while the SSA algorithm has (depending on the exact distribution of cells) some advantages for sampling rate, TSS tends to produce higher dwell times over each neuron for the same neuron density. This dwell time could be further increased by "parking" the laser over a cell for longer. However, this comes at the expense of sampling rate. The duration of time spent collecting photons from each target structure provides an indirect way to compare the SNR (all other things being equal). SNR is critical to the fidelity with which APs can be reconstructed from calcium transient time series. Therefore, we analysed the extent to which it can be improved by increasing the dwell time over each neuron in TSS.

To examine this, we used the TSS paths at different sampling frequencies for functional calcium imaging of cortical cells while simultaneously doing whole cell patch-clamp elec-

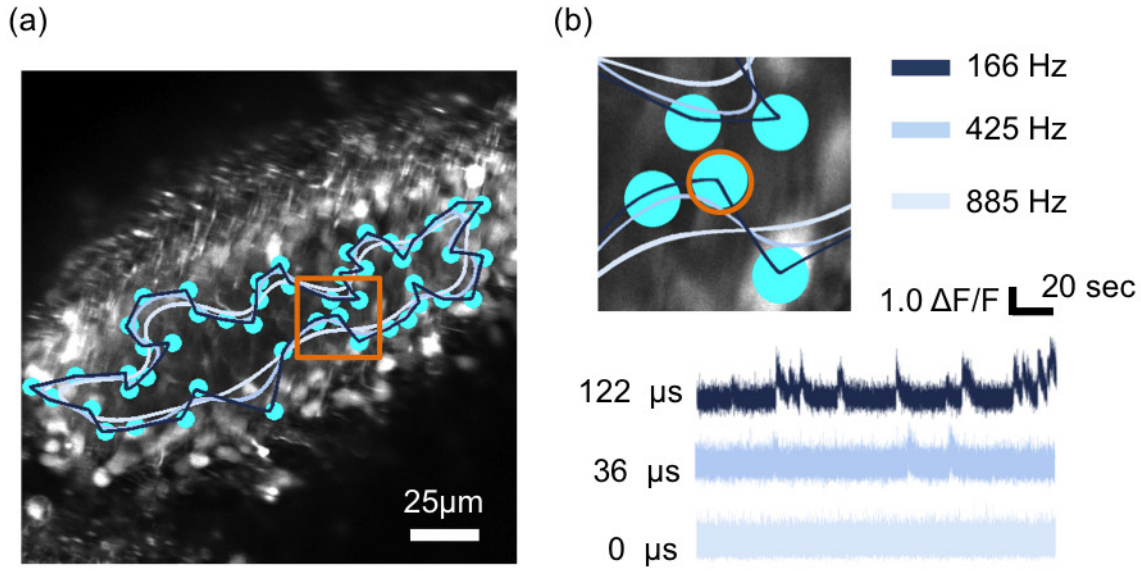


Figure 3.4: High sampling rates in TSS lead to ROI dropping. (a) Raster scan of an imaged region of dentate gyrus. Spontaneously active neurons are indicated by cyan discs. The 3 different TSS paths shown indicate the trajectory followed by the MPLSM focal point when the galvos were driven at increasing speed (scale bar 25 μm). (b) Expansion of the orange square in (*a*); path colour indicates sampling rate (scale bar 10 μm). (c) Time-series of the orange-highlighted neuron for different dwell times corresponding to the different scanning frequencies in (*b*).

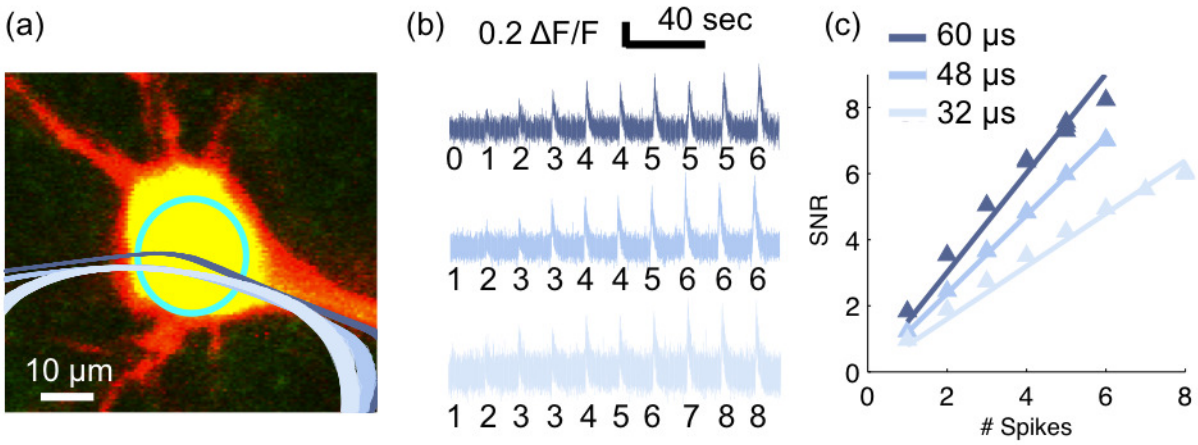


Figure 3.5: Photon collection with TSS. (a) Zoom in on a whole cell patch of a cortical pyramidal cell with the associated ROI (cyan circle) and three TSS paths overlaid: 102 Hz (dark blue), 137 Hz (medium blue) and 208 Hz (light blue) (scale bar 10 μm). (b) Calcium time series associated to the TSS paths in (*a*) and their corresponding number of APs. (c) SNR evolution with an increasing number of APs for the three TSS paths shown in (*a*) and corresponding to the calcium traces shown in (*b*). The photon collection time (dwell time) from the patched cell was: 60 μs (dark blue data points), 48 μs (medium blue data points) and 32 μs (light blue data points). For each TSS path, a linear least square fit has been used on the SNR values.

trophysiology on one of the cells in the scanning path (Fig. 3.5a). This allowed us to elicit individual APs from the patched cell, in current clamp mode, in order to measure SNR. Increasing numbers of APs were elicited, yielding calcium transients of increasing amplitude, and correspondingly, SNR (Fig. 3.5b). For a relatively small number of APs (up to 8), signal amplitude increased approximately linearly with the number of APs elicited for the three TSS paths (Fig. 3.5b). We measured the SNR per spike by taking a linear fit of the plot of SNR (calculated as described in Methods) versus the number of APs elicited (Fig. 3.5c). The slope of the linear fit can then be interpreted as the SNR per spike, that is, a measure of the signal quality independent of the number of APs in a given event. The increase of the slope values in Figure 3.5c between the three TSS paths clearly shows that the SNR per spike increases with dwell time (time spent collecting photon from the ROI) albeit at the expense of sampling frequency.

To further compare the trade-off between SNR and sampling frequencies amongst raster scanning, TSS and SSA, we used the same technique of simultaneous functional calcium

imaging and whole cell patch clamp recording of one cell on the scanning path. For each patched cell ($n = 4$ in our study) we could define multiple cell geometries (with different cell counts) and therefore, try out multiple scanning paths within a $300 \times 300\,\mu\text{m}^2$ FOV. To determine and visualize the scanning paths of TSS and SSA, we overlaid them over the recorded tissue. If at the depth of the studied patched cell, surrounding neurons were not well loaded with the Cal-520 AM bath loading technique, we chose random ROIs to be scanned by TSS and SSA. We found our Cal-520 AM bath loading technique most effective down to $\sim 30\,\mu$m under the slice surface for mice $<$ PND21 (see Methods). Below this depth, the loading of the tissues decreases down to $-50\,\mu$m where it stops. We filled the patched neuron with Cal-520 potassium salt (see Method) to ensure that the cell was well-loaded.

Figure 6a shows a representative two-photon image of a cortical pyramidal cell while Figure 6b shows the overlaid TSS and SSA scanning paths. The recorded somatic potential and the corresponding calcium trace from raster scanning at 10 Hz are shown in Figure 6c. This scanning frequency was achieved by raster scanning over a much smaller FOV, $180 \times 180\,\mu\text{m}^2$. The calcium traces from TSS and SSA scanning over the entire FOV are shown in figure 6d. For all the scanning strategies, we also found an almost linear increase in the SNR with the number of APs (up to 8). This is shown in a linear fit of the plot of SNR versus number of APs for three examples, with different scanning algorithms and sampling rates, in Figure 3.6e. Note that these are examples taken at different sampling rates, and should not be compared directly. To appreciate the trade-off between SNR and sampling rate for the three scanning algorithms, we then plotted the cumulative data for SNR per spike versus sampling rate for the different experiments (Fig. 3.6f). The three examples from Figure 3.6e are indicated in Figure 3.6f by orange symbols. Overall, it is apparent that raster scanning typically achieves the highest SNR per spike: 1.49 (median value amongst $n = 14$ trials), importantly, at a substantial cost in sampling frequency and FOV (or number of cells sampled). In these examples, TSS and SSA scanning achieved similar SNR per spike of 0.75 (median of $n = 9$ TSS paths) and 0.74 (median of $n = 14$ SSA paths), respectively. The similarity in SNR for TSS and SSA in these examples is due to the TSS path being driven at

high sampling rates and therefore reducing the dwell time spent on the patched neuron. Path precision analyses on galvo positions also show that most of the high sampling frequencies achieved with the TSS paths are missing ROIs (Fig. 3.6f). For the same neural distributions, the SSA paths were driven at relatively conservative f_s and therefore did not miss any ROIs (Fig. 3.6f).

Lower bounds on the uncertainty of AP timing

The quality of signals obtained by multiphoton fluorescence calcium imaging can be measured in various ways. One way is to measure the root mean square (RMS) deviation between the measured fluorescence time series, and the true underlying calcium signal - if one had access to it. Unfortunately, however, this is not the case. In any event, for many applications we are particularly interested in reconstructing spike trains, and thus, in the time at which AP-induced calcium transients occur. Relevant ground truth for this situation can be obtained, by performing whole-cell patch clamp electrophysiology simultaneously with imaging, as described above. The question then is how well the timing of each AP can be reconstructed from the scanning data [Reynolds et al., 2015]. One way to assess that would be to apply a particular spike train reconstruction algorithm, and to measure the RMS error in the timing of spikes. However, the results would apply only to that particular reconstruction algorithm. A more general approach, which we take here, is to compute the Cramer-Rao lower bound (CRB) of the variability with which spike timing can be extracted using any algorithm, based upon the measured properties of the recorded signals. In this paper, we compute the lower bound on the uncertainty of the estimated location of one AP. Details of this calculation are provided in Methods and the Appendix. Although this is simpler than the general case of reconstructing the location of an unknown number of spikes, it is indicative of algorithm performance at one of the key challenges of successful spike train reconstruction — estimating the location of an AP with high temporal precision. The resulting quantity describes the temporal precision of the scanned signals, and can thus be used to compare different scanning algorithms in this respect.

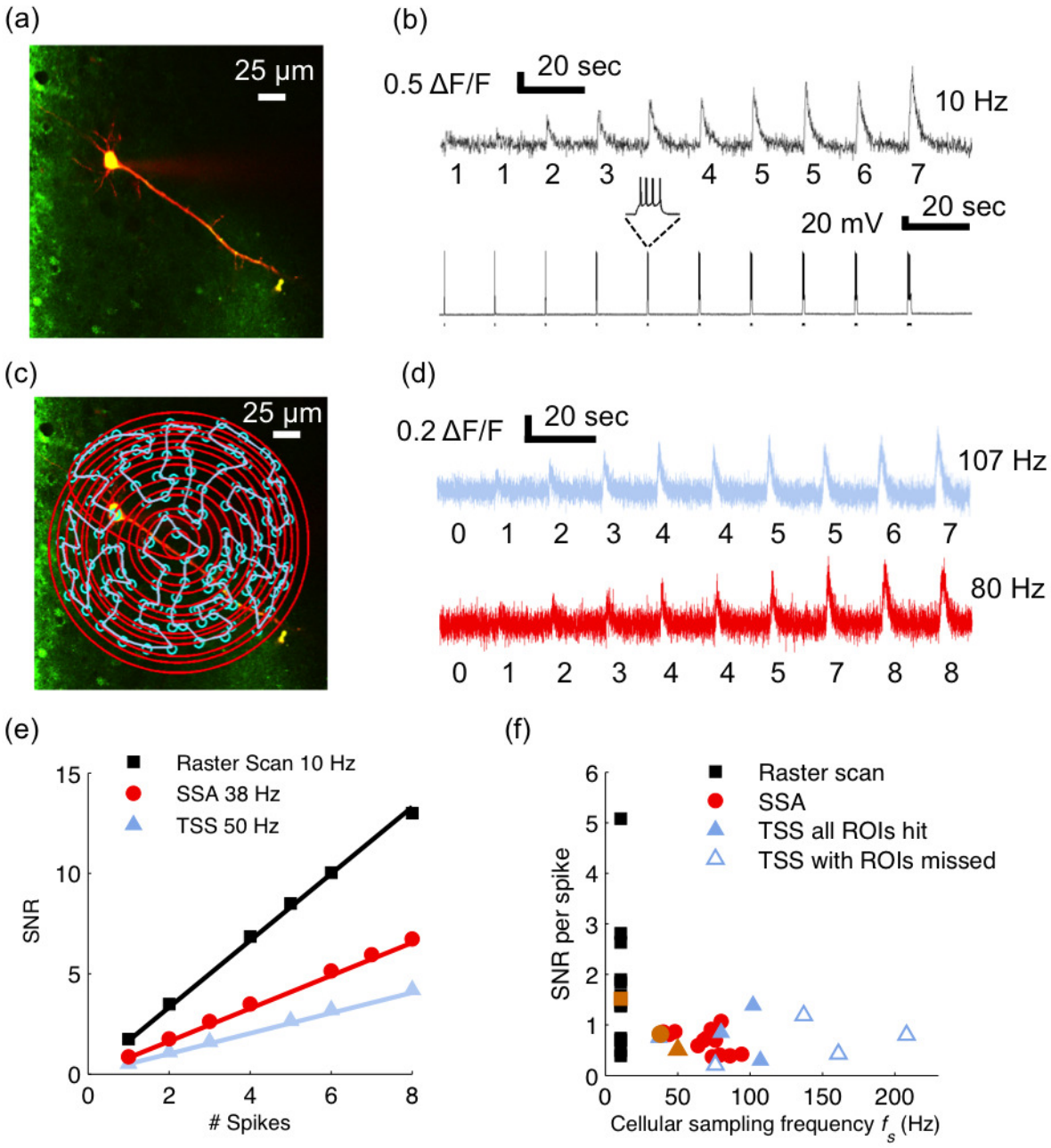


Figure 3.6: Simultaneous functional calcium imaging and ground truth electrophysiology recordings for raster scanning and scanning strategies. (a) High resolution image showing a whole-cell patch of a cortical pyramidal cell (scale bar 25 μm). (b) High resolution image showing the SSA (in red) and TSS (in light blue) scanning trajectories for 129 neurons. The locations of the neurons in cyan (except the cell that is patched) have been chosen arbitrarily as the neurons were not well loaded with Cal-520 AM) at this imaging depth (scale bar 25 μm). (c) Representative example of recorded somatic potential (bottom) and raster scanning associated time series (top) sampled at 10 Hz. Black bars under recorded somatic potential indicate the current step duration in the stimulation protocol. The number of APs evoked is written under each calcium transient. (d) Representative example of times series sampled at 107 Hz for TSS (in light blue) and 80 Hz for SSA (in red). The numbers of APs at every stimulation is written under each trace. (e) Example of SNR evolution with an increasing number of APs for raster scanning, TSS and SSA. For each type of scan, a linear least square fit has been used on the SNR values. (f) SNR per spike values for multiple (n=14) raster scans at 10 Hz and multiple SSA (n=14) and TSS (n=9) scans for cellular sampling frequencies within [38 Hz to 208 Hz]. The filled data point markers represent scanning paths where all the ROIs are hit whereas the open ones represent the paths with missed targets along the scanning trajectory. The orange markers correspond to the example in (*e*).

We analysed the experiments from the previous section in which whole-cell patch clamp electrophysiology was used to evoke accurately timed APs while one of the three scanning algorithms was used to record calcium transients. For each acquisition, we calculated the CRB of the uncertainty in spike time estimates from the time series. Figure 3.7 shows the interplay between SNR and f_s on the CRB. Figure 3.7a shows the CRB - SNR plane and we see that for each scanning algorithm the CRB value decreases, that is, the temporal precision of the acquisition increases, when the SNR value increases. For a given uncertainty in AP timing, raster scanning requires the highest SNR among the three. That is, TSS and SSA are able to achieve comparable uncertainties in spike time estimates as raster scanning despite their lower SNR (Fig. 3.7a). This is due to their high sampling frequencies. Similarly, in the CRB - f_s plane in Figure 3.7b, we see that raster scanning can achieve AP uncertainty less than 20 ms only at SNRs greater than 3. In contrast, AP timing uncertainty below 20 ms was achievable for SNRs less than 1.5 with both TSS and SSA.

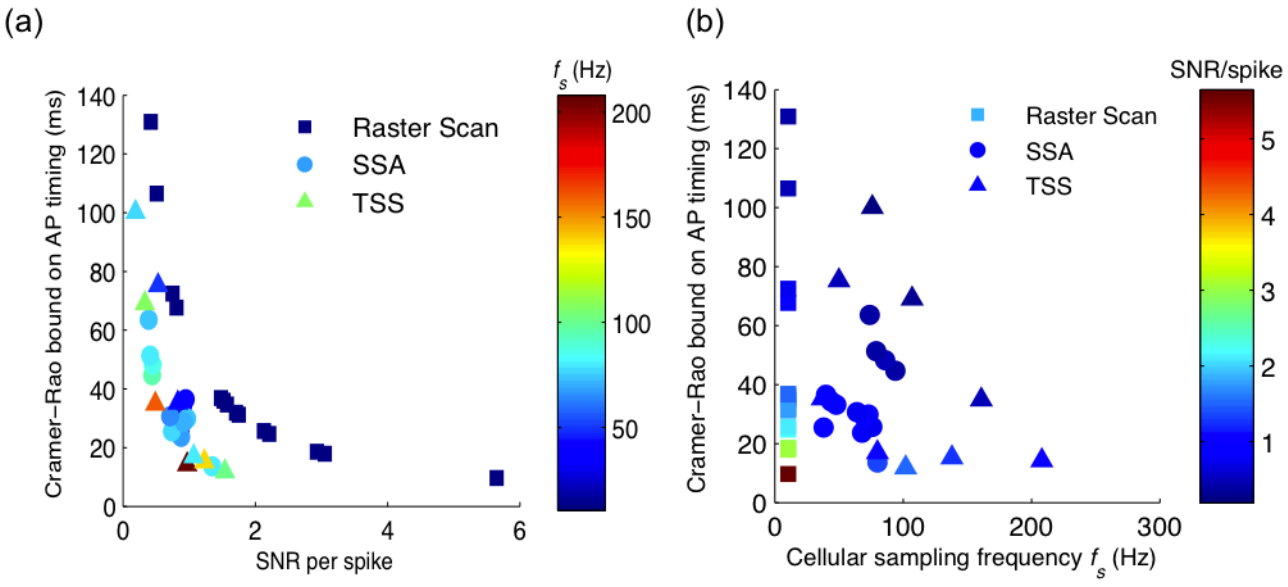


Figure 3.7: Uncertainty in timing of reconstructed action potentials depends on both SNR and sampling frequency. (a) The Cramer-Rao lower bound on the uncertainty with which the time of an action potential can be estimated, as a function of SNR (abscissa) and sampling frequency (colour scale), for raster scanning (n=14 cells), TSS (n=9 cells) and SSA (n=14 cells). Ground truth spike timing was obtained by simultaneous whole-cell patch clamp electrophysiology. (b) The same dataset visualised with sampling frequency on the abscissa and SNR on the colour scale.

3.5 Discussion

We have described in detail the Adaptive Spiral Scanning algorithm for use with a standard commercial galvo-based multiphoton microscope and have demonstrated its capability for recording high quality, high sampling rate (100s of Hz) time series signals from many cells simultaneously. We have compared its performance in terms of sampling rate and SNR to raster scanning and the Travelling Salesperson Scanning algorithm. We have found that SSA outperforms raster scanning by an order of magnitude in terms of achieved f_s for the same population of neurons. It likewise outperforms TSS in f_s for common neural densities encountered in *in vitro* experiments (visual cortex, somatosensory cortex, GCs of the hippocampus). We have also found the SNR of TSS to be higher than that of SSA as TSS spends, on average, more time per cell collecting photons since it allows the laser to be "parked" on each ROI. However, the SNR of raster scanning exceeds those of both scanning strategies TSS and SSA as it scans the entire neuron. The low sampling rate for raster scanning is sufficient to capture calcium events. However, the cost for raster scanning is a much smaller FOV and thus, fewer cells that can be sampled. For instance, a $300 \times 300\,\mu\text{m}^2$ region may be sampled at $\sim$3 Hz by raster scanning, whereas the same region may be sampled by SSA at $\sim$100 Hz. For a larger FOV (and hence, a larger neural population), e.g $500 \times 500\,\mu\text{m}^2$, the raster scanning sampling rate decreases to $\sim$1 Hz. Although this frequency may still allow some calcium events to be captured, there will be considerable loss in the accuracy of spike timing estimates.

We have also compared the different scanning strategies in terms of signal quality of the calcium traces. This can be measured by a number of different metrics [Onativia et al., 2013, Wilt et al., 2013, Reynolds et al., 2015, Theis et al., 2015]. In our study, we used the Cramer-Rao Bound to measure the temporal precision between the onsets of the calcium transients and their associated APs emitted by the neuron. This metric shows the weight of the f_s and SNR in the temporal precision of the acquisition (see 3.3.4 and 3.6). The values of the CRB represent the lower bound of an AP time estimate from the calcium imaging data.

We found that to attain the same temporal precision, raster scanning needs a significantly higher SNR than either TSS or SSA. This is due to the f_s of the SSA and TSS being at least an order of magnitude higher than the f_s of raster scanning for the same number of neurons scanned.

The measure of signal quality and the choice of the scanning type for functional calcium imaging is heavily dependent on the experimental setup. In *in vitro* experiments, it strongly relies on the ability to induce the dye into the tissue with the bath loading technique. The latter depends on the composition of the bath and the age of the animal [Hamad et al., 2015]. In older brain slices (>PND 21), protective recovery slicing methods [Ting et al., 2014], bulk loading [Stosiek et al., 2003] or even newly developed bath loading techniques [Mauleon et al., 2013] help to induce the dyes into the tissue even if the amount of dye induced is less then in juvenile mice. Therefore, using a longer dwell time per scanned neuron (achievable with the TSS) might be necessary to obtain a good SNR when imaging older dye loaded brain slices. The quality of the signal is also determined by the choice of the dye. Recent development of genetically encoded voltage indicators [Gong et al., 2015, Knöpfel et al., 2015] show major improvements regarding kinetics when compared to calcium indicators. In the case of voltage indicators, fetching a single fluorescent event is only achievable at high sampling rates (achievable with TSS and SSA) as the kinetics are relatively close to the original AP. However, it remains to be seen if scanning strategies enable sufficient SNR to precisely detect a voltage fluorescent event engendered by a single AP. All these experimental aspects highlight the need to develop adaptable scanning strategies for standard MPLSMs to enable the fine tuning of scanning parameters and obtain the best signal quality considering the general experimental framework limitations.

Moreover, another positive aspect resulting from scanning strategies is the minimal coverage of the imaged FOV in comparison to raster scanning: only one line segment passes through each ROI for each full trajectory thus limiting the overall heating of the tissue and bleaching of the dye [Podgorski and Ranganathan, 2016].

In addition to improving the functional fluorescent signal quality acquired with a stan-

dard MPLSM of large neural networks, these scanning strategies only require software development and hence are not expensive and easily transferable from one setup to another.

3.6 Appendix 1: Cramer Rao bound for spike detection from calcium imaging data

This appendix was written as a joint effort with Stephanie Reynolds (EEE department Imperial College).

3.6.1 Signal model

We model a fluorescence signal, consisting of K spikes at time points t_k, with the following equation

$$f(t) = \sum_{k=1}^{K} A \left(e^{-\alpha(t-t_k)} - e^{-\gamma(t-t_k)} \right) u(t-t_k), \tag{3.2}$$

where A, α, γ are the amplitude, rise and decay parameters of the characteristic pulse shape and $u(\cdot)$ is the indicator function. When a signal only contains one spike at location t_0, we write

$$f(t) = A \left(e^{-\alpha(t-t_0)} - e^{-\gamma(t-t_0)} \right) u(t-t_0). \tag{3.3}$$

We assume we have access to N noisy samples $\{y[n]\}_{n=0}^{N-1}$ of this signal, such that

$$y[n] = f[n] + \varepsilon[n]. \tag{3.4}$$

Here, $\varepsilon[n]$ are samples of a zero-mean Gaussian process with standard deviation σ^2 and $f[n] = f(t)\Big|_{t=nT}$ are samples of $f(t)$ evaluated at $t = nT$.

3.6.2 Cramer-Rao bound calculation

The Fisher Information for estimating a single parameter t_0 from N samples $\{y_0, y_1, ..., y_{N-1}\}$ of the form in Eq. (3.4) is

$$I(t_0) = \frac{1}{\sigma^2} \sum_{n=0}^{N-1} \left(\frac{\partial f}{\partial t_0}(nT) \right)^2. \tag{3.5}$$

The Fisher information uses a partial derivative of f with respect to t_0 — in the following working we thus consider t (the time stamp from the set $\{0, T, 2T, ..., (N-1)T\}$) to be fixed. From Eq. (3.3), we have

$$f(t) = g(t, t_0)u(t - t_0), \tag{3.6}$$

where

$$g(t, t_0) = A \left(e^{-\alpha(t-t_0)} - e^{-\gamma(t-t_0)} \right). \tag{3.7}$$

By the product rule and from Eq. (3.6), we have

$$\frac{\partial f}{\partial t_0} = g(t, t_0) \frac{\partial}{\partial t_0} (u(t - t_0)) + \frac{\partial}{\partial t_0} (g(t, t_0))\, u(t - t_0). \tag{3.8}$$

The distributional derivative of $u(x)$ with respect to x is the dirac delta function, so that we obtain

$$\frac{\partial}{\partial t_0} (u(t - t_0)) = -\delta(t - t_0). \tag{3.9}$$

From Eq. (3.8) and Eq. (3.9), the derivative evaluated at $t = nT$ is

$$\frac{\partial f}{\partial t_0}(nT) = -g(nT, t_0)\delta(nT - t_0) + \frac{\partial}{\partial t_0} (g(nT, t_0))\, u(nT - t_0). \tag{3.10}$$

Due to the delta function, this derivative is infinite if $t_0 = nT$, so when the sample is picked exactly at the timepoint of the spike. For our analysis, it suffices to simulate a fluorescence

signal with $t_0 \neq nT$ to remove this singularity. Mathematically, it is probably sufficient to state that, if the spike location t_0 is continuously distributed across the time interval [0,(N-1)T], there is zero probability that $t_0 = nT$, so $\delta(nT - t_0) = 0$ almost everywhere (in the sense of the Lebesgue measure). Furthermore, a thorough analysis of the CRB might necessitate it being averaged over all possible values of t_0, i.e. computing

$$\text{Mean CRB} = \frac{1}{(N-1)T} \int_0^{(N-1)T} \text{CRB}(t_0) \mathrm{d}t_0. \tag{3.11}$$

In this case the integral over the troublesome set of measure zero where $t_0 = nT$ would be 0, which removes the singularity. We can therefore write

$$\frac{\partial f}{\partial t_0}(nT) = \frac{\partial g}{\partial t_0} u(nT - t_0) \tag{3.12}$$

$$= A \left(\alpha e^{-\alpha(t-t_0)} - \gamma e^{-\gamma(t-t_0)} \right) u(nT - t_0). \tag{3.13}$$

The Fisher Information is thus

$$I(t_0) = \frac{A^2}{\sigma^2} \sum_{n=0}^{N-1} \left(\alpha e^{-\alpha(t-t_0)} - \gamma e^{-\gamma(t-t_0)} \right)^2 u(nT - t_0). \tag{3.14}$$

The CRB, the inverse of the Fisher Information, is

$$\text{CRB} = \left[\frac{A^2}{\sigma^2} \sum_{n=0}^{N-1} \left(\alpha e^{-\alpha(t-t_0)} - \gamma e^{-\gamma(t-t_0)} \right)^2 u(nT - t_0) \right]^{-1}. \tag{3.15}$$

Chapter 4

Introduction to 3D scanning strategies

4.1 Abstract

Recording the activity of neural populations at high sampling rates is a fundamental requirement for understanding computation in neural circuits. Two photon microscopy provides one promising approach towards this. However, neural circuits are three dimensional, and functional imaging in two dimensions fails to capture the 3D nature of neural dynamics. ETLs provide a simple and cheap method to extend laser scanning microscopy into the relatively unexploited third dimension. We have therefore incorporated them into our SSA algorithm, which calculates kinematically efficient scanning strategies using radially modulated spiral paths. We characterised the response of the ETL, incorporated its dynamics using MATLAB models of the SSA algorithm and tested the models on populations of Izhikevich neurons of varying size and density. From this, we show that our algorithms can theoretically at least achieve sampling rates of 36.2Hz compared to 21.6Hz previously reported for 3D scanning techniques.

4.2 Introduction

Understanding neuronal dynamics is a key step towards comprehending brain function and dysfunction and will help inform future treatments of brain disorders. In order to understand these dynamics the activity of many neurons must be sampled at high frequency and in three dimensions. MPLSM of genetically encoded Ca^{2+} indicators enables high spatial (μm) and rapidly improving temporal (ms) resolution imaging of large numbers (up to 1000) of labelled neuronal subtypes. Thus far most imaging occurs in two dimensions due to the difficulty of quickly shifting the focal plane along the optical axis. This precludes cross-layer cortical information flow capture. To address this problem, several strategies evolved to image in 3D including AODs [Katona et al., 2012], mechanical objective translation [Goebel et al., 2007], wavefront shaping [Quirin et al., 2014] and ETLs [Grewe et al., 2011]. All of these techniques except ETLs require custom built or extensive additions to microscopes, whereas an ETL can easily integrate into a commercial MPLSM setup. Previous implementations combined ETLs with x-y raster scanning; however, as demonstrated by our previous work [Schuck et al., 2014], 'smart' scanning strategies increase sample rates 5-10x by reducing time spent scanning extracellular space. Our algorithms take GSs and ETL inertia into account to calculate a faster spiral scanning trajectory in 3D. In this paper, we show two examples of 3D scanning strategies that resolve Ca^{2+} transients from GCaMP6f for a population of 800 neurons.

4.3 Materials and methods

4.3.1 ETL Model

Our system uses an ETL (EL-10-30-VIS-LD, Optotune) in conjunction with an offset lens (f = -75 mm, LC4513-A, Thorlabs) placed close to the objective rear aperture, powered by a current source (LD3000R, Thorlabs), to axially translate the focal plane. We measured

the current source command voltage/axial shift curve (Fig. 4.1) using a phantom of 1 μm fluorescent beads (F-13080, Life Technologies) suspended in 1% agarose. By measuring the objective displacement required to refocus the microscope onto beads as a function of voltage, we show that the ETL can be approximated by a linear system over a range of $120-800\,\mu$m. This range spans up to layer five of the mouse cortical column. Fig. 4.1 shows the data with a linear fit with a slope of $-3508\,\mu\text{mV}^{-1}$ and an offset of $51.94\,\mu$m.

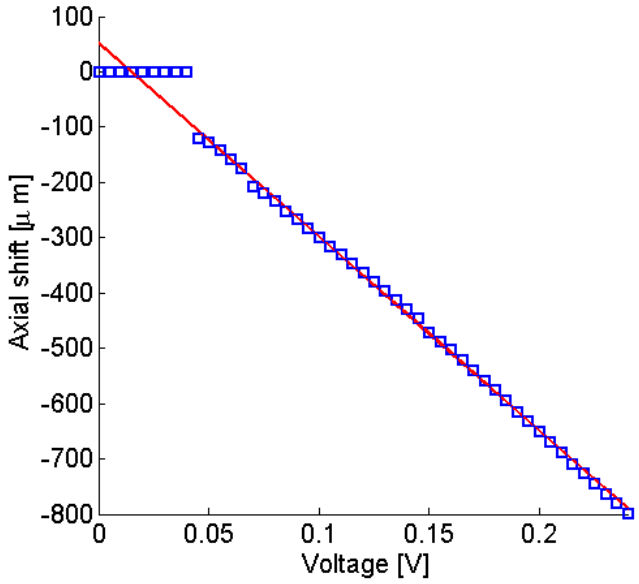


Figure 4.1: The measured axial shift of the focal plane (blue squares) as a function of command voltage fit with a linear function (red line) which we use to calculate its response. A = f(V) = -3508V + 51.94 where A is the axial shift in microns and V is the command voltage.

Figure 4.2 shows ETL step response data measured by Optotune [Opt, 2014] fit with our model (see table 4.1), a damped sine modulated by a first order exponential:

$$z(t) = G(1-e^{-\beta t})(1+Ae^{-\alpha t}sin(2\pi\omega_0 t+\phi)) \tag{4.1}$$

$G\,[mm]$	β [s^{-1}]	$A\,[mm]$	α [s^{-1}]	$\omega_0[Hz]$	ϕ [rad]
0.1096	243	-2.011	357.2	384.4	-0.9332

Table 4.1: Fitted parameters for our model of the ETL step response function. G is the gain, β the time constant of the first order exponential, ω_0 the natural oscillation frequency, A the amplitude of the oscillation, α the damping factor and ϕ the phase.

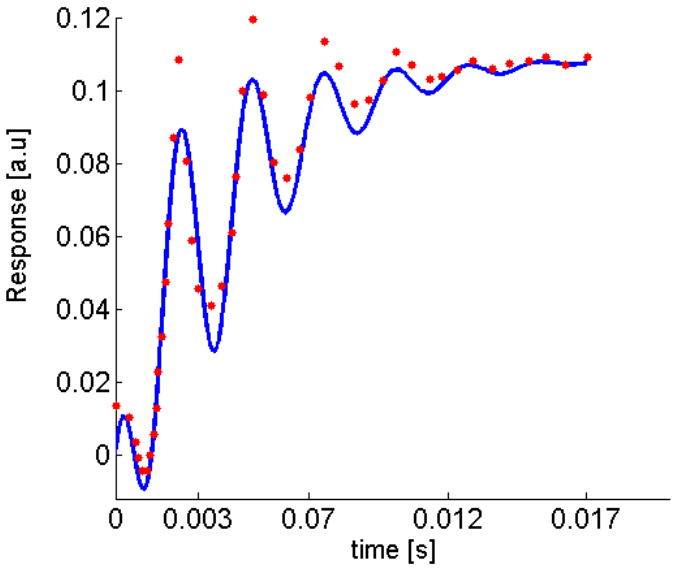


Figure 4.2: Our model of the dynamic response of the ETL (blue line) fit to the step response recorded by Optotune (red points).

4.3.2 Scanning and neural population model

Our previous work introducing the 2D SSA algorithm [Schuck et al., 2014] showed how we characterised the galvanometer's (6215H, Cambridge Technology) transfer function similarly to the ETL. In order to validate the scanning algorithm on real brain tissue samples, GFP was expressed in mouse primary somatosensory cortex (S1) via stereotactic injection of adenoassociated viruses under the CAG promoter into C57BL/6 mice (Fig. 4.3). 6 weeks post-injection, animals were perfused with 4% PFA, the brain removed and submerged in ACSF prior to 2-photon imaging. Procedures were Home Office (UK) approved and accorded with the Animals (Scientific Procedures) Act 1986. 3D algorithms use the transfer functions to calculate the driving signals, I_X, I_Y and V_z delivered to the two GSs and the ETL respectively, to move the focal point to the coordinates X, Y, Z. The algorithm, given a set of neuronal coordinates, sorts the neurons by distance from the center of the FOV and increasing axial depth. Starting at the FOV center it scans the neurons in an x-y spiral trajectory in a z-plane defined by the center of the first neuron. Once the spiral reaches the first neuron's center the axial focal depth is increased stepwise using the ETL. Neuron densities are usually high enough such that the spiral will have sampled activity from the tops of deeper neurons.

Therefore the depth is increased to coincide with the shallowest neuron center not already sampled sufficiently by the beam. This is shown schematically in figure 4.4. To test the algorithm we generated surrogate data from functional fluorescent signals governed by calcium indicator GCaMP6f dynamics [Chen et al., 2013] from firing patterns of Izhikevich neurons [Izhikevich, 2003],[Schuck et al., 2014].

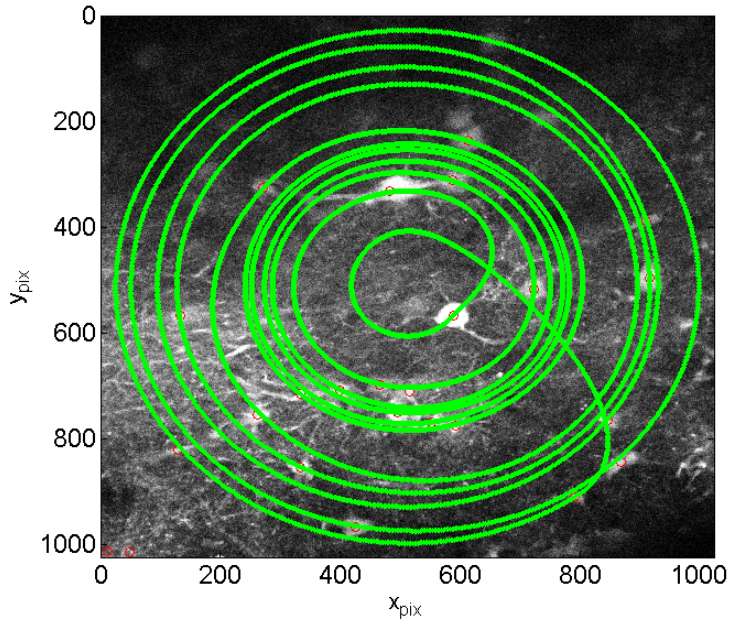


Figure 4.3: An example beam path from our SSA algorithm applied to GFP labelled neurons. We acquired a full frame raster scan of 1024x1024 pixels and automatically extracted the coordinates of the neuron centres (red circles). Finally, we used these coordinates with our 2DSSA algorithm to generate a spiral scanning path (green line).

4.4 Results

Combining a simulated population of neurons emitting fluorescent signals and a 3D dynamical model of the scanning elements from a MPSLM, we built a platform that is able to test various kinds of scanning strategies. Here we describe the performance and limitations of the SSA algorithm extension.

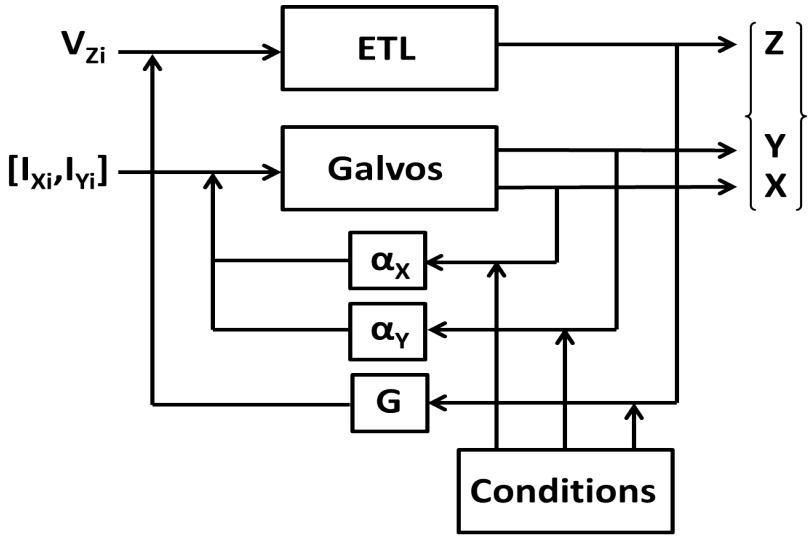


Figure 4.4: 3D Scanning model block diagram. α_X, α_Y and G are the gains in the open loop from GS_X, GS_Y and the ETL respectively which are modulated to produce axially displaced spiral paths which sufficiently sample all neurons.

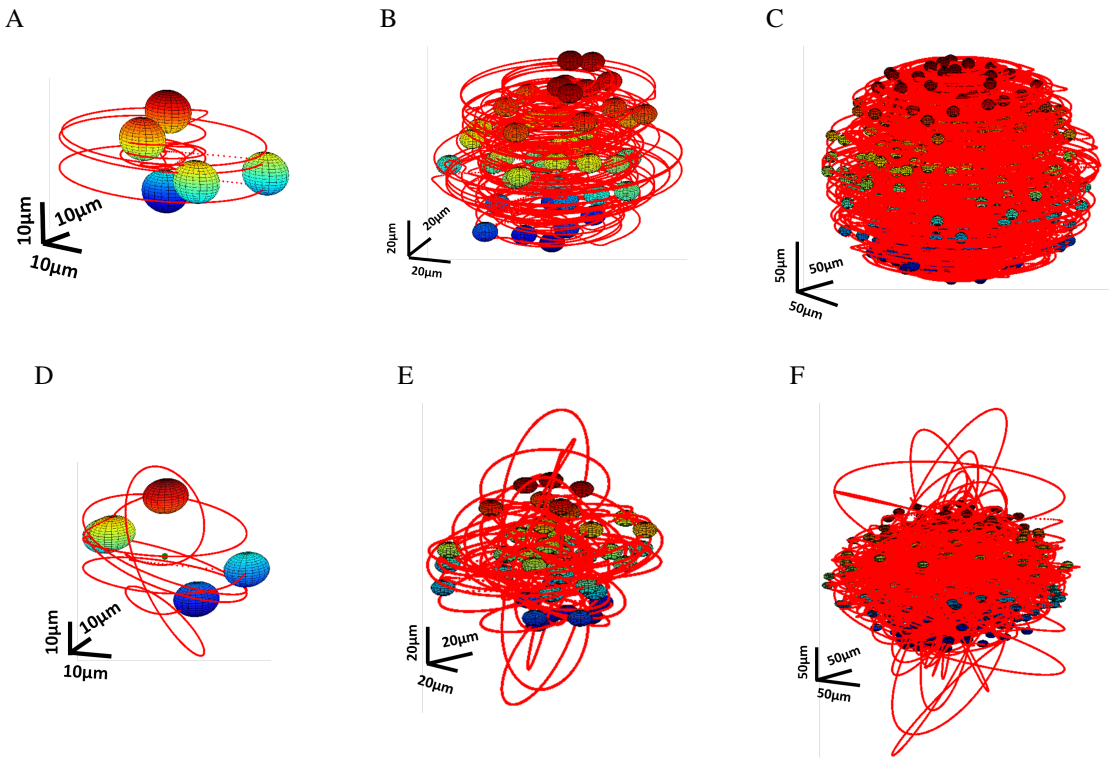


Figure 4.5: Two examples of 3D MPLSM scanning strategies on pseudo-random population of neurons. *A*, *B* and *C* represent the laser path in red for the CST for five, fifty and five hundred cells. The spherical neuron distribution is modelled with the spatial density of active cells in mouse V1 [Cossart et al., 2003]. *D*, *E* and *F* represent the laser path of the OST.

4.4.1 SSA algorithm extension for 3D scanning

Algorithm: *3D Cylinder Scanning Strategy*

Data: Randomly distributed neuron population $\{n_1, n_2, .., n_N\}_{N\in\mathbb{N}^*}$ and dynamical model of GSs and ETL.

Result: $[X, Y, Z]$ smart trajectory coordinates

$\forall(i, j) \in \mathbb{N}^*$,

Sort the neurons by decreasing depths z_i from the top of the acquisition and compute their radius $r_i = \sqrt{x_i^2 + y_i^2}$.

indx describes the number of tops of deeper neurons already scanned with a sufficient number of samples.

begin

- **for** $i \Leftarrow 1$ **to** N **do**
  - (i) Apply sinusoidal current (I_{X_i}, I_{Y_i}) to the GSs and the constant voltage V_{Z_i} to the ETL to drive the laser beam along a spiral with radius r_i
  - indx = 1
  - (ii)**while** *scanning the spiral* r_i **do**
    - **for** $j \Leftarrow i+1$ **to** N **do**
      - **if** *laser scans with sufficient sample* n_j **then**
        - indx = indx+1
    - **if** *laser scanned* n_i **then**
      - i = i+indx
- **if** *scan* n_N **then**
  - Same algorithm with a change of index so that we scans n_N to n_1

We used the SSA algorithm in a 2D experiment on 6 μm fluorescent beads (Polyscience Inc) suspended in 1% Agarose. Driving the GSs above a threshold frequency elicited position drift. Hence, in our simulation we decreased the amplitude modulated sine frequency applied to the GSs I_X, I_Y from $\omega_I = 10$ kHz to $\omega_I = 1$ kHz. Two 3D Algorithm were tested: the 'Cylindrical' scanning strategy (CST) and 'Orbital' scanning strategy (OST) which differ by the type of ETL driving signal. For the CST, the voltage V_z applied to the ETL is a series of steps: $V_{z_i} = \frac{z_i}{G}$ where $i \in \{1..N\}$, G is the gain of the ETL, $[z_i]_{i\in\{1..N\}}$ are the planes occupied by the neurons and N is the total number of scanned cells (See Algorithm (i)). For the OST, the voltage V_z applied to the ETL is an amplitude modulated sinusoid: $V_{A_i} = A_i sin(\omega_{ETL} t)$ where $A_{i\in\{1..N\}}$ is the amplitude and ω_{ETL} the frequency of the voltage applied to the ETL. For reasons of clarity, we present only the CST algorithm in detail here. We combined the previously CST presented driving signals with specific geometric conditions (see Algorithm (ii) and Fig. 4.4) resulting in modulated, tilted, circular trajectories fit to a randomly positioned 3D set of cells (Fig. 4.5 *A*, 4.5 *B* and 4.5 *C*), reducing the impact of the GSs inertia and where the user can define a neuron dwell time determining the time spent in each axial plane.

4.4.2 Sampling frequency and calcium transient acquisition

Driving the dynamics of the GSs and the ETL with the above described driving signals enabled us to calculate the sampling frequency of our 3D scanning strategies across various neural geometries. Fig. 4.6 *A* shows that for a constant density of cells, there is a log-log linear decrease in sampling frequency for both the CST and the OST. Theoretically, single neuron AP extraction necessitates a sampling rate over the Nyquist frequency corresponding to a calcium transient from a specific fluorescent protein. Based on these requirements, our simulation simultaneously resolved calcium transients (GCaMP6f) from 800 neurons with the CST and 700 neurons with the OST (Fig. 4.6 *A*). Our simulated raw PMT signal acquisition is based on the same principle as for the 2DSSA [Schuck et al., 2014]. Fig. 4.6 *B*, 4.6 *C*

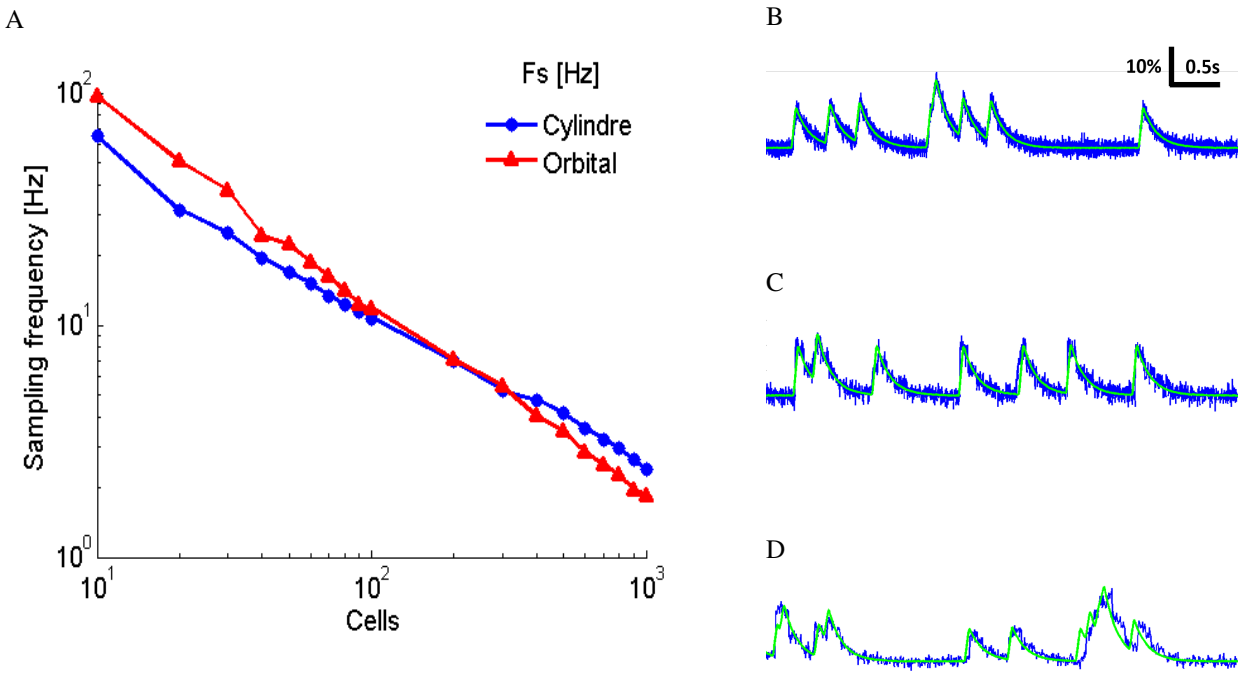


Figure 4.6: 3DSSA allows the sampling of high number of neurons. *A* is a loglog plot representing the Sampling frequency decay of both CST and OST according to the number of cells. This was done for a specific neuron density $d = 9.5 \times 10^{-5} \mu m^{-3}$ and shows that we can resolve calcium transient for up to 800 cells with the cylinder scanning strategy. *B*, *C* and *D* describe ground truth fluorescent in green and reconstructed calcium transient in blue from 5, 50 and 100 neurons sampled at 156 Hz, 18 Hz and 10 Hz over 5 s, respectively with the CST.

and 4.6 *D* show ground truth fluorescent (green) and reconstructed Calcium transient (blue) from 5, 50 and 100 neurons sampled at 156 Hz, 18 Hz and 10 Hz respectively for the CST.

4.5 Discussion

Here we present faster 3D scanning strategies using an ETL. Previous studies such as [Grewe et al., 2011] reported a 21.6 Hz scan rate for 34 neurons in two planes separated by 40 μm using AODs. Our CST can sample 40 neurons distributed in and between equivalent planes using cheaper GSs at a higher rate of 36.2 Hz. Simulations also indicate our strategy will be able to sample 800 neurons sufficiently fast to detect Ca^{2+} transients from GCaMP6f. Our OST further increases scanning speeds up to 51.6 Hz for the same situation and offers significant increases for up to 200 neurons (Fig. 4.6). We also hope to further increase scan speeds by applying optimal control theory to our 3D algorithms to find kinematically optimal modulations of the driving signals applied to GSs and ETL. The highest scanning speed that we can achieve whilst maintaining high enough sampling for good spike detection accuracy [Onativia et al., 2013, Reynolds et al., 2015] remains to be seen. One possible problem we anticipate when we implement high speed scanning in hardware is drift in focal spot position caused by heating of the ETL and GSs. This could cause the trajectory to drift enough to bypass some neurons completely and require software compensation. We are currently working towards validating our model by imaging functional fluorescent indicators in mouse cortex both *in vivo* and *in vitro*.

4.6 Acknowledgement

We thank Stephan Smolka of Optotune for useful discussions on ETL technology.

4.7 Future work: 3D scanning strategies experimental validation

To thoroughly characterize the path precision in 3D, I needed to know/record the position of the two-photon focal spot at any moment in time and space. The GSs mirror positions can be recorded at any time thanks to the servo driving the GSs in close loop, but this option is not available with the ETL as it is driven in open loop without a position readout. Therefore, one aspect of this precision validation consists of directly recording the movement of the MPLSM focus in a fluorescein solution (see Fig. 4.7 *A* and *B*). In order to image the trajectory, a lateral 10x microscope was built with a 10x objective (CFI Plan Apo Lambda - Nikon), a tube lens (AC508-180-A - Thorlabs) and a high speed camera (FastCam SA3, Photron) see Fig.4.8 *A* and *B*. A good approximation of the trajectory followed by the focal spot could be achieved once a z projection of 100 frames was done (see Fig. 4.9 and Fig. 4.10).

However, this does not give us a full characterization of the path precision. An additional position synchronization test needs to be run between GSs and ETL as the horizontal (x,y) GSs command was achieved with the software 'Sciscan' (Scientifica Ltd) and the axial command (z) was run by a separate Labview program. A slight delay between the two control signals would cause the ETL and GSs to desynchronize and impact on the precision of the acquisition. Another problem that can be encountered is an increased size of the point spread function when the ETL is placed at the rear of the objective due to the ETL reducing the effective NA of the objective. Hence, further characterization needs to be done to see whether a horizontal or vertical positioning of the ETL in the optical path is optimal and how much 'pulse shaping' needs to be done in both cases to adjust the point spread function of the microscope focus. Once these problem have been solved, the 3D scanning path can be validated on fluorescent microbeads embedded in agar.

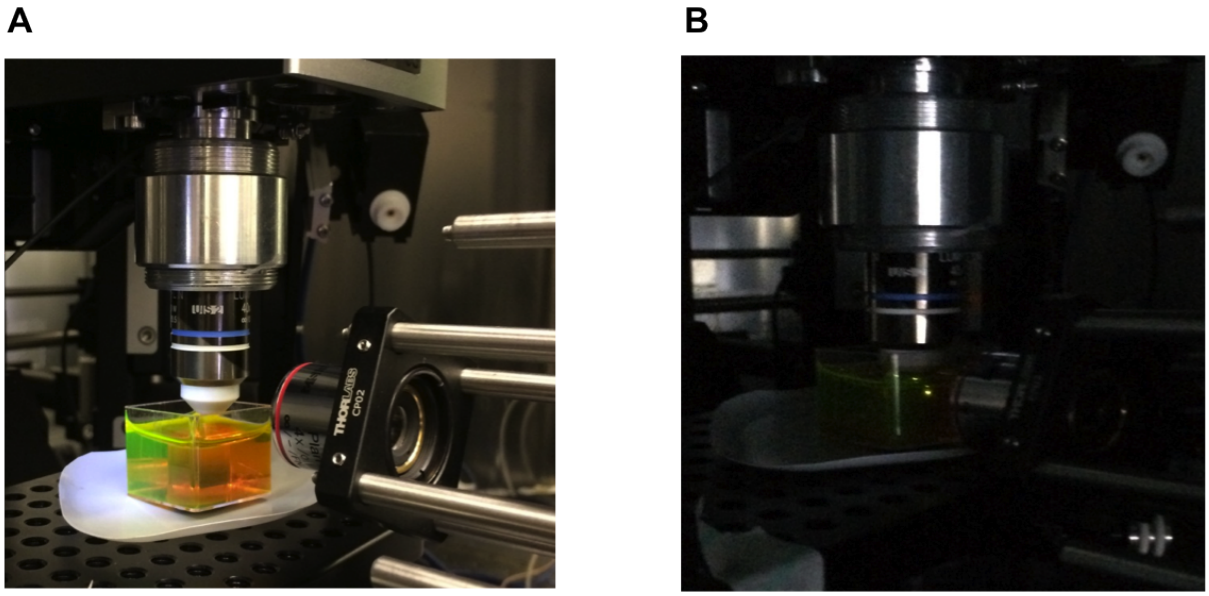


Figure 4.7: two-photon focal spot in fluorescein. *A* Picture of the two-photon objective with the ETL at the rear, the fluorescein solution and the 10x objective of the lateral microscope. *B* Same picture as in *A* but during focal spot position acquisition

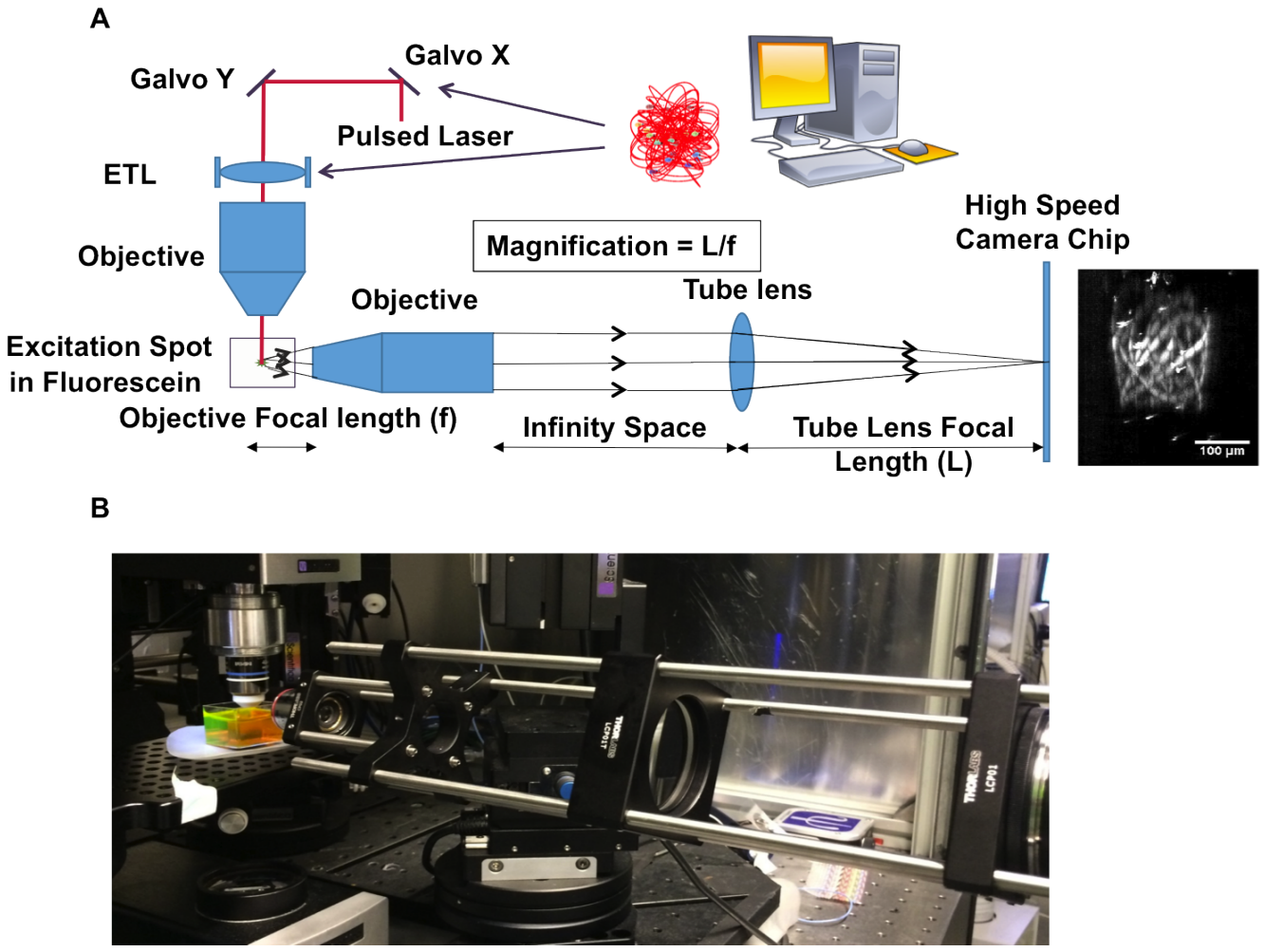


Figure 4.8: 3D two-photon focal spot imaging. *A* Schematic representing the different stages of imaging the MPLSM focal spot. The first stage is to generate the simulated trajectory with the computer. Second stage consist of mapping this trajectory to voltages that correspond to GSs and ETL. The third and last stage is to image the focal spot with a high speed camera via the lateral microscope. *B* Picture of the schematic *A*

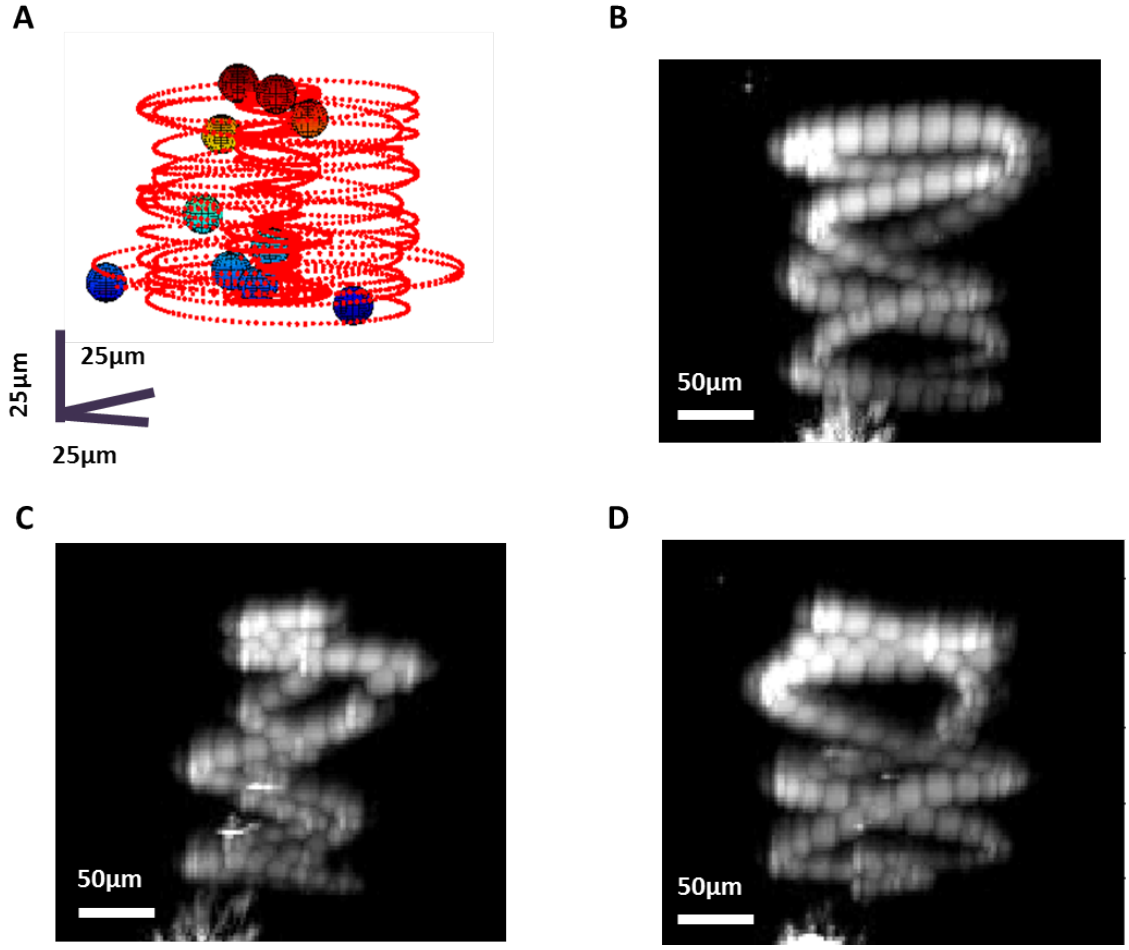


Figure 4.9: 3D cylinder scanning strategy position assessment. *A* Computer simulated trajectory of the cylinder 3D scanning strategy for 10 neurons. *B*, *C* and *D* each represent the maximal intensity projection of 100 video frames taken at 5 kHz. 100 frames at a time are shown for visualization purposes.

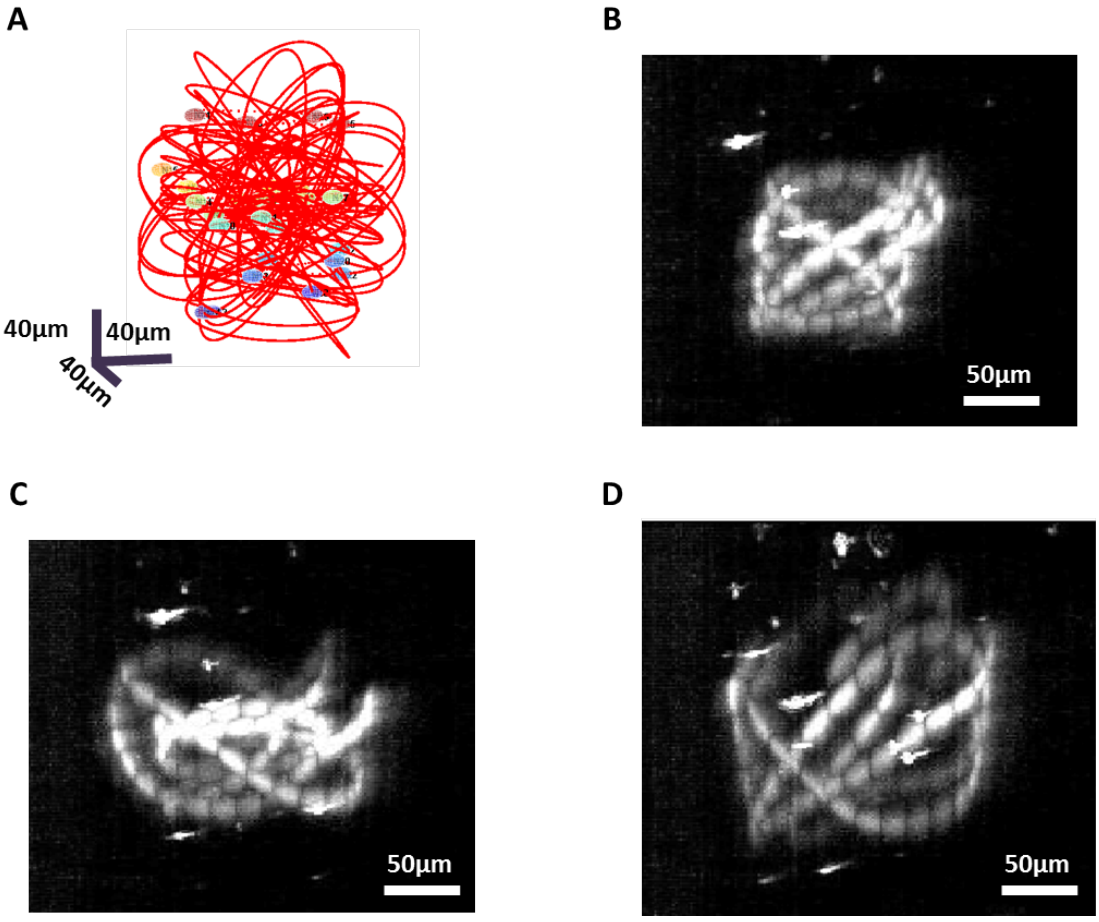


Figure 4.10: 3D orbital scanning strategy position assessment. *A* Computer simulated trajectory of the orbital 3D scanning strategy for 25 neurons. *B*, *C* and *D* each represent the maximal intensity projection of 100 video frames taken at 5 kHz. 100 frames at a time are shown for visualization purposes.

Chapter 5

Functional calcium imaging of dentate granular cells in slices

The previously presented work mostly concerns engineering techniques that improve the temporal resolution of functional calcium imaging with a commercial standard MPLSM in *in vitro* brain slice experiments. In this section, I will discuss the preliminary results on hippocampal GC microcircuit dynamics. As described in 3.3.2, after quickly extracting the brain of the anesthetized mouse, I cut horizontal slices (400 μm each) and only saved the ones that contained the three main parts of the hippocampus (DG, CA1 and CA3 see Fig.5.1) known as the tri-synaptic loop. I focused the functional calcium imaging effort on DGCs, (see Fig.5.1 *C*) for three main reasons. Firstly, many GCs were spontaneously active in juvenile wild-type mice, providing a good benchmark to test the 2D scanning strategies (see 3.4). Secondly, the functionality of the DG is poorly understood when compared to CA3 and CA1 and only very few studies have used functional calcium imaging with a MPLSM for both for in-vitro [Yu et al., 2013] and *invivo* [Pilz et al., 2016] large neural population recordings, making it a very novel and exciting research area. Finally, these cells seem to be involved in certain aspects of memory, associative/spatial learning and pattern separation processes [Scharfman, 2007, Lopez-Rojas and Kreutz, 2016, Treves et al., 2008] and that in the longer run, I would like to compare their activity on a microcircuit level to ones from an

aged-matched mouse model of Alzheimer's.

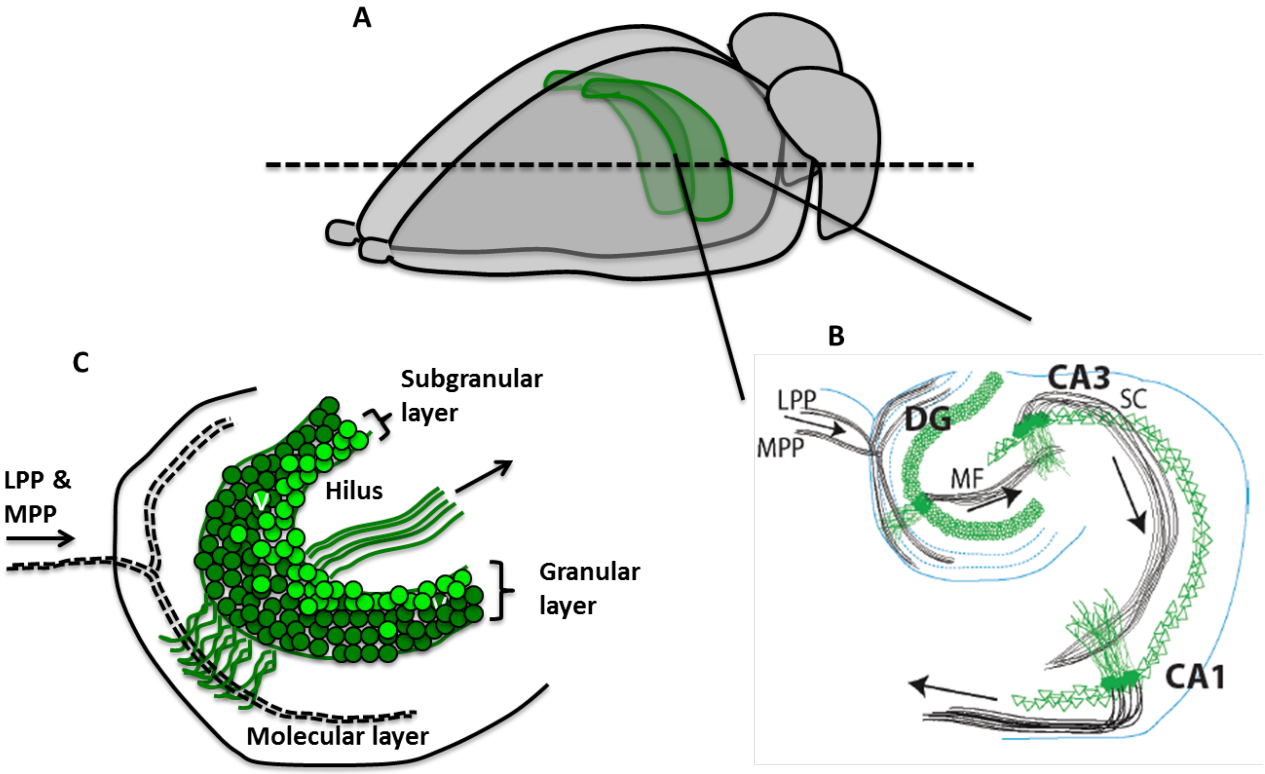


Figure 5.1: Horizontal Hippocampal mouse brain slice schematic. *A* Mouse brain schematic with hippocampal structure highlighted in green and horizontal slicing direction represented by the black doted line. *B* Tri-synaptic connections schematic. First, the Lateral and Medial Perforant Path (LPP and MPP) project to the GCs which in turn project to CA3 through the Mossy Fibers (MF) *Madar, Ewell et Jones 2017, submitted.* Finally, CA3 pyramidal cells project to CA1 through the Schaffer Collaterals (SC) *C* Dentate Gyrus Schematic at PND14. Mature granular cells are represented in dark green whereas immature granular cell are represented in light green

5.1 Spontaneous activity of hippocampal granular cells

5.1.1 Juvenile wild type mice

The development of the granular layer is characterized by its delayed and heterogeneous maturation in comparison to the other major neural structures of the hippocampus (CA1, CA3) [Schlessinger et al., 1975]. Immunostaining has been used to follow the development of DGCs in the rat brain for the entire of the first postnatal month, after which the DG

is considered fully mature [Pedroni et al., 2014]. The same study found that immature GCs are scattered in the hilus at PND2, with immature and mature GCs coexisting at PND6 in the granular layer, and mostly mature GCs were found in the granular layer at PND28 (although immature GCs were still found in the subgranular zone see Fig.5.1 C).

Additionally, Pedroni et al. (2014) [Pedroni et al., 2014] electrophysiologically characterized the spontaneous firing patterns of immature GCs between PND1 and PND3 using whole cell patch recordings. Across all their patched immature GCs (n=63), they showed that most were firing bursts of APs induced by giant depolarizing potentials similar to the ones found in CA1 [Ben-Ari et al., 1989]. During this postnatal period, they also reported some immature GCs being spontaneously active and only very few of them showing no activity at all.

Patching cells is a tedious process and [Pedroni et al., 2014] were only able to sample from 63 cells. While testing the 2D scanning strategies for MPLSM, there was a high data throughput and I was able to scan around 150 GCs in each of the in vitro calcium imaging experiments (see Fig.3.4 *B* and *C* and Fig3.6 *A*). I only have preliminary results here to show that more spontaneous calcium traces throughout the entire granular layer at PND10 were detected than at later developmental stages (here PND14), where the spontaneous activity was more confined to the subgranular zone (see Fig.5.1 *C* and Fig.5.2 *A* and *B*). These results are consistent with the developmental studies performed by [Pedroni et al., 2014] and if continued, would allow the study of the dynamics of spontaneous network oscillations of immature DGCs and their contribution to the consolidation of circuit connectivity.

5.1.2 Adult wild type mice

The development of new neurons or neurogenesis only occurs in two main areas of the adult brain throughout adulthood: The subventricular zone of the olfactory bulb, and the subgranular layer of the hippocampal DG [Sakamoto et al., 2014, Gonçalves et al., 2016]. Adult newborn immature DGCs take around 8 weeks to integrate into the granular layer circuit and are thought to have functional implication in learning and memory due to their

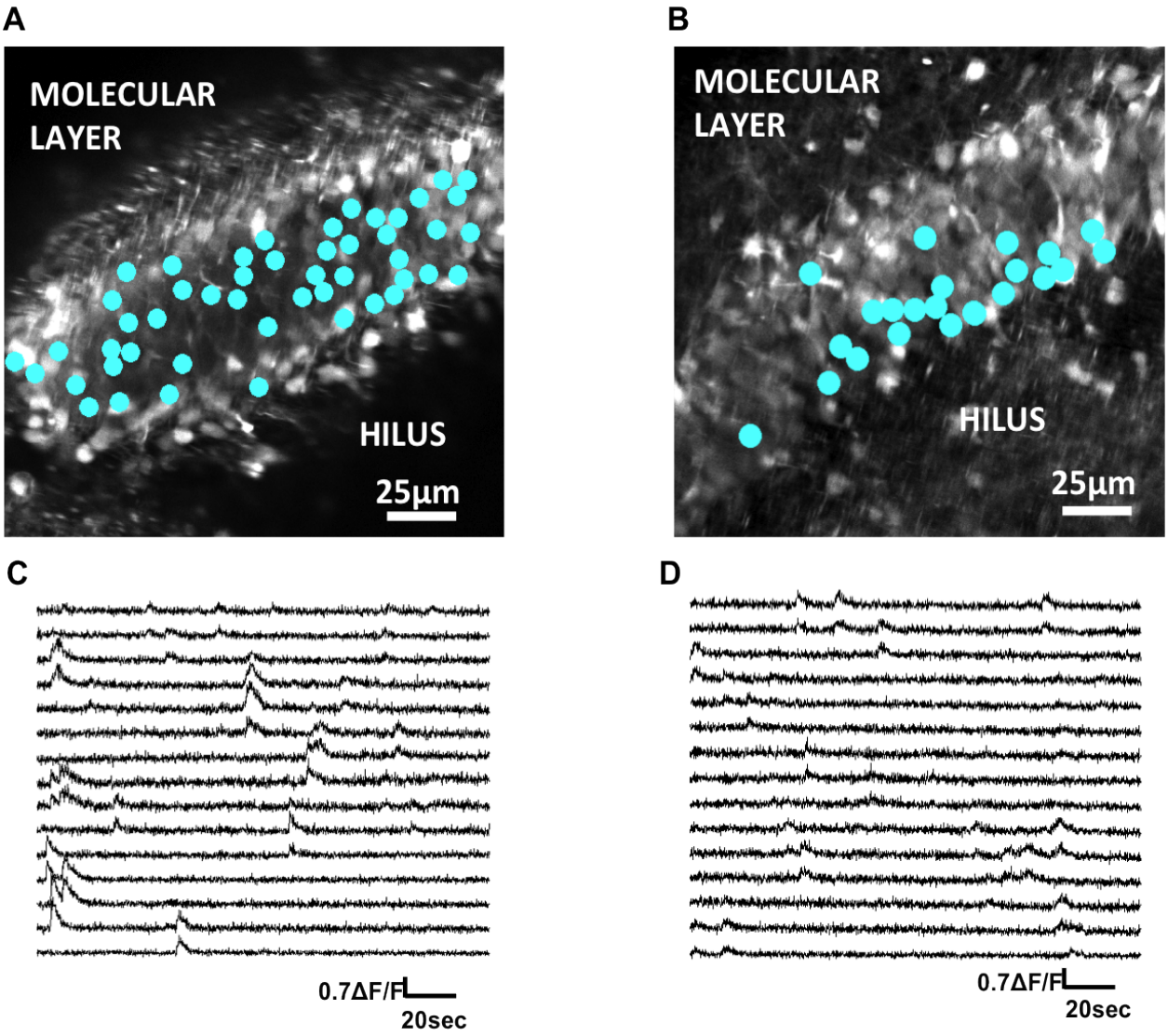


Figure 5.2: Spontaneous activity of Dentate Gyrus granular cells in juvenile wild-type mice. *A* High resolution image taken at PND 10 showing the three regions of the DG: the molecular layer, hippocampal granular cells and the hilus. The cyan ROIs represent the neurons showing spontaneous activity. *B* High resolution image taken at PND 14, showing the same three regions of the DG. *C* 15 time-series displaying spontaneous activity and corresponding to a subset of the 50 ROIs of image *A*. *D* Spontaneous activity displayed in 15 calcium times series from a subset of the 23 ROIs in image *B* . In both *B* and *C* calcium traces were acquired with frame scanning at 10 Hz

higher excitability and increased plasticity [Ninkovic et al., 2007, Abrous and Wojtowicz, 2015]. Although, controversial studies [Redondo et al., 2014, Ryan et al., 2015] also show that mature GCs, which in comparison are almost always silent, contribute to the same higher cognitive functions. Consequently, the relative contribution between adult newborn GCs and mature GCs in learning and memory processes still remains unknown.

I carried out the same in-vitro hippocampal brain slice experiments in the juvenile wild-type mice as described previously (3.3.2), but this time with two and a half month old adult mice where the DG was completely mature. The brain slicing preparation is very similar (see subsection3.3.2) except for the slicing ACSF and dye loading protocol. To preserve older slices, we used the "protective recovery method" [Ting et al., 2014] using the following slicing ACSF saturated with carbogen (95% O2/5% CO2) : 92 mM NMDG, 2.5 mM KCl, 1.25 mM NaH2PO4, 30 mM NaHCO3, 20 mM HEPES, 25 mM glucose, 2 mM thiourea, 5 mM Na-ascorbate, 3 mM Na-pyruvate, 0.5 mM CaCl24H2O and 10 mM MgSO47H2O. The brain slices were first sliced into this slicing ACSF at 1-4°C, then placed in the same sACSF but at 34 °C (this constitutes the protective recovery step) and finally transferred to the recovery ACSF (as is subsection 3.3.2) where they were kept for one hour prior to imaging. Regarding the bath loading technique, it worked up until PND21 after which the dye would not penetrate into the tissue of the older slices. This is with relevance to a recent study which tried bath loading with various AM-ester fluorescent dyes in cell culture at different ages [Hamad et al., 2015]. Here, a workaround technique was used to "bulk-load" the dye, a technique that works in-vivo and in-vitro in older animals and was developed by [Stosiek et al., 2003] but is, however, more challenging and only loads a tiny area of the slice. The external solution used for the bulk-loading technique in older slices consists of: 50 μg of Cal520-AM, 3 μL of pluronic P-127 and 0.5 μL of Alexa594. This solution is vortexed and left resting in the dark for one hour. 76 μL of the following solution: 150 mM NaCl, 2.5 mM KCl, 10 mM HEPES at pH 7.4 is then added and the entire solution is sonicated for around 2 minutes before being placed in a filter eppendorf and centrifuged for approximatively 0.5 sec. Glass pipettes (the same used as in 3.3.3) were pulled and filled with this dye solution. Using the same micro-manipulator as for patch clamp experiments, the glass pipette was inserted

into the tissue approximatively 100 μm under the slice surface. Both Köler and two-photon tissue illuminations were used to make sure that the pipette was inserted in the correct area of the slice (in our case the pipette was inserted in the hilus close to the granular layer) and that the pipette was not blocked (see Fig.5.3 *A*, *B* and *D*). After successful bulk loading, a one hour wait-time is required before imaging to let the dye solution diffuse into the tissue sufficiently.

Again, I have only very preliminary results showing that adult newborn GCs contain sparse spontaneous activity, using funcitonal calcium imaging (see Fig.5.3 *B*, *C* and *E*). Their location is consistent with the fact that immature GCs are born in the subgranular zone of the DG (see ROIs of Fig. 5.3 *C*). In the future, these results could be compared with age matched recordings from an Alzheimer's mouse model in order to get a better understanding of how spontaneous activity in adult newborn neurons plays a role in learning and memory in neurodegenerative disease.

5.2 Pattern separations in hippocampal granular cells

All populations of neurons tend to, on some level, follow either pattern separation or pattern completion processes [Santoro, 2013]. In the case of the DG, the discrete memory representation is thought to be based on the pattern separation process. In rodents, layer 2 of the entorhinal cortex (around 112,000 principal neurons) is the main input to the the DG granular layer (around 1,200,000 GCs) which then directly relays the information through the mossy fibers to CA3 (around 250,000 pyramidal cells). Therefore, the DG is seen as a gate, where the pattern separation process is due to the sparse representation of the input from the entorhinal cortex in the granular layer.

Multiple in-vivo electrophysiology studies have tried to identify the functionality of the DG, but its role seems to be more challenging to define then other sub-areas of the hippocampus (CA1,CA3)[Leutgeb et al., 2007, Marrone et al., 2011, Neunuebel and Knierim, 2012]. The in-vivo electrophysiology study carried out by [Leutgeb et al., 2007] in rats shows a

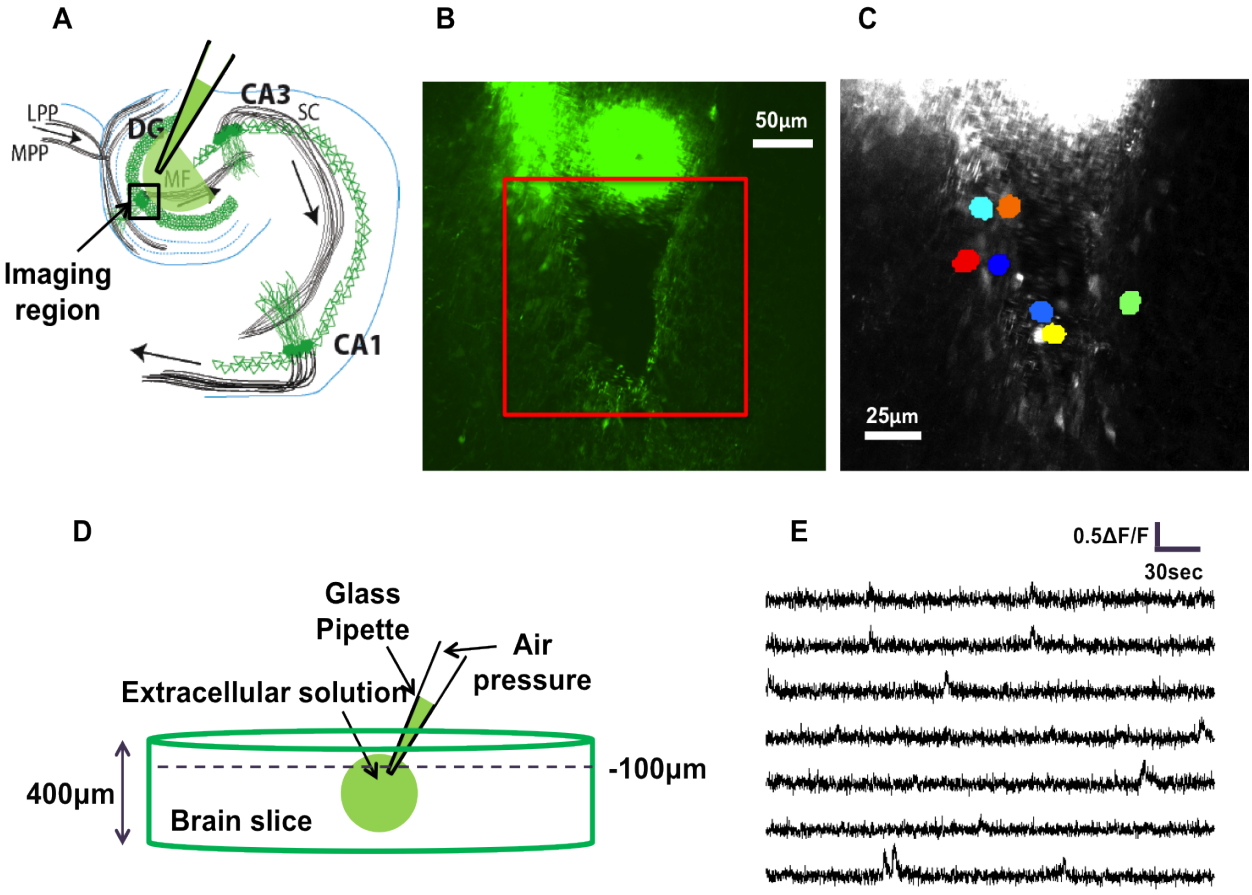


Figure 5.3: Spontaneous activity in Dentate Gyrus granular cells of adult wild-type mice. *A* Schematic of the tri-synaptic Hippocampal loop showing the two-photon imaging and dye loading regions. *B* High resolution image $300 \times 300\,\mu m^2$ showing both where the glass micropipette went into the tissue to execute the bulk loading (in green) and encircled in red, the area where functional calcium imaging was performed. *C* High resolution image $180 \times 180\,\mu m^2$ of the tissue where functional imaging was performed (see image *D*) and ROIs of neurons showing SA. *D* Schematic of the bulk loading protocol see subsection 5.1. *E* Times-series acquired with frame scanning at 10 Hz and corresponding to the ROIs in *C*.

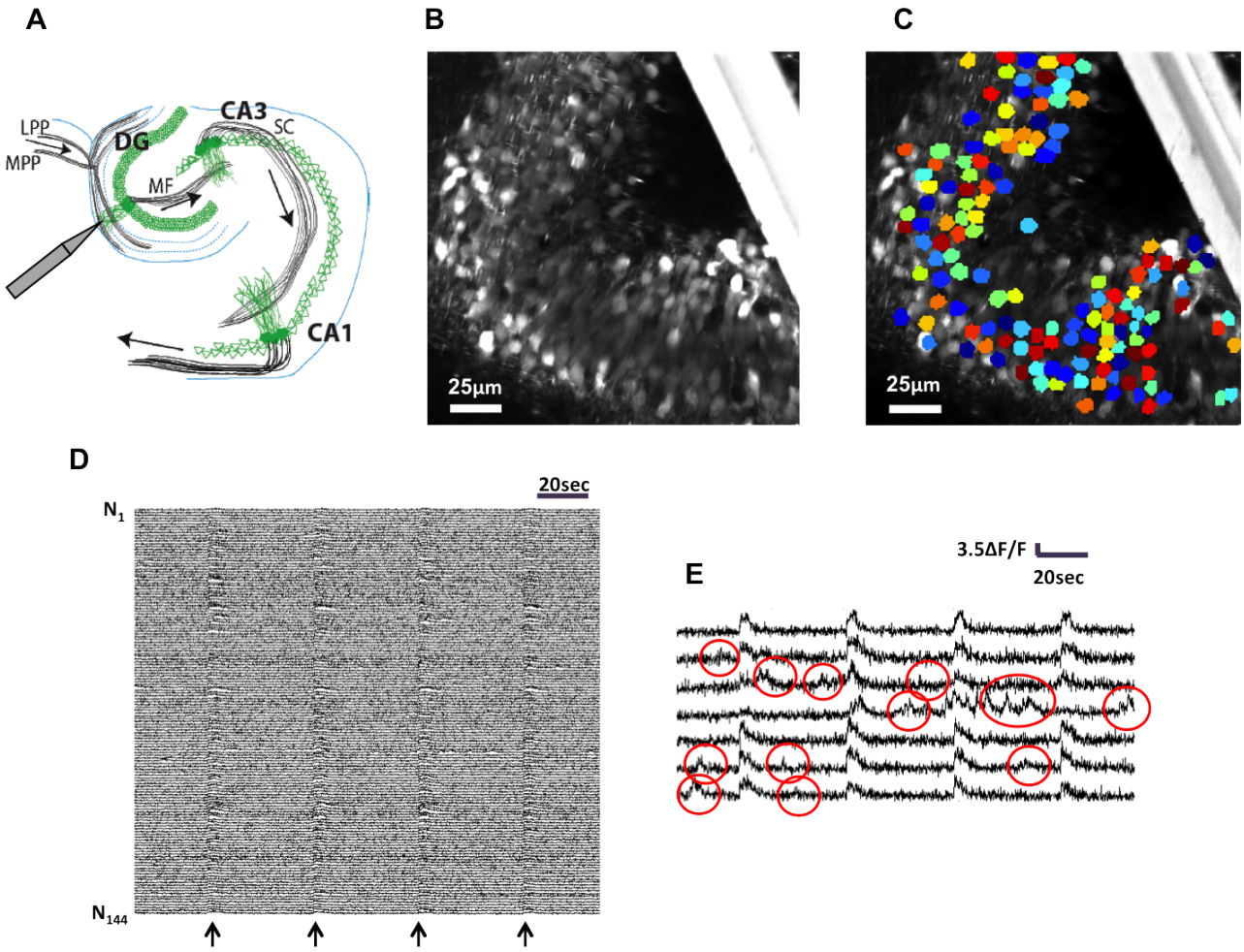


Figure 5.4: Evoked activity of Dentate Gyrus granular cells in Juvenile (PND 13) wild-type mice. *A* Schematic of the tri-synaptic Hippocampal loop showing the positioning of the micro-electrode stimulating at the edge of the DG molecular layer. *B* High resolution image $180 \times 180\,\mu m^2$ showing the Hippocampal granular layer (A subsection of a nylon fiber from the nylon mesh stabilizing the brain slice is seen on the top right corner of the image). *C* Same image as *B* but including the 144 ROIs corresponding to neurons responding to electrical stimulation. *D* 3 min times series acquisition with frame scanning at 10 Hz of the 144 ROIs shown in *C*. Electrical stimulation is represented by the arrows under the times series and occurs every 40sec. *E* Subset of the time series in *D* showing neurons containing both SA (highlighted in red) and evoked activity (every 40sec).

more sparse representation of spatial receptive fields in the DG than in CA3. They performed two distinct experiments while recording simultaneously from DGCs and CA3 pyramidal cells. Their first experiments consist in letting the rat run in an enclosure changing gradually from square to circular and vice versa (the walls of the enclosure are flexible). In this fashion, they show how a slight change in the rat's environment is reflected in both DGCs and CA3 pyramidal neurons. This experiment led to the conclusion that through sparse input representation from the entorhinal cortex in DGCs, complete orthogonalization of slight environmental changes could be achieved in CA3. Their second experiment consisted of considerably changing the rat's environment. Here, their recordings show that statistically independent neural population subfields of CA3 were activated, indicating that the pattern separation process caused by a significant change in the environment was triggered by a direct link between entorhinal cortex and CA3.

If the in-vivo electrophysiology experiments show strong evidence that the DG is implicated in pattern separation, it does not give a precise explanation of the process at the cellular level. To gain a deeper understanding on a microcircuit level, in-vitro horizontal hippocampal slices retaining axonal connection between entorhinal cortex and hippocampal subfields should be used (see 3.3.2). The only main in-vitro studies of pattern separation in the DG were carried out by [Hyde and Strowbridge, 2012, Zylberberg et al., 2016]. These studies show how stimulating different locations of the perforant path can be decoded in separable EPSP frequencies of downstream DG hilar neurons. These studies are based on repeated patch clamp results from 3 hilar neurons over experiments. To overcome the tediousness of the patch clamp technique, I show preliminary results of functional calcium imaging of large neural networks in the DG granular layer that considerably increases the amount of data acquired per experiment (see Fig.5.4 *A*,*B*,*C*,*D* and *E*). I hypothesize that using spatially segregated electrical input and similarity input variations on the PP, while functionally imaging the DG at the mesoscale using an MPSLM, will enable a deeper understanding in pattern separation processes on a microcircuit level *in vitro*.

5.3 Appendix: Hydrogel photolithography with MPLSM

Any focused laser source can perform photolithography in hydrogels when used with the right parameters (i.e wavelength, material and exposure time). Regular 3D printers are using this concept with specific choices of resins. As with an MPLSM, 3D printers are using two GSs to steer the laser focal point in the direction of the layer of resins that needs to be polymerised. This process is being repeated layer after layer until the entire object has been 3D printed. By 'hacking' into the controls of 3D printers, one can change the printing parameters e.g laser exposure time and power of the laser to be able to use its polymerisation ability to a broader sets of materials. This customised control of 3D printers has been used to build biocompatible 3D scaffold hydrogels. In this context, two types of biocompatible scaffolds can be polymerised. The first one consist of the polymerisation between a hydrogel precursor (seeded with living cells) and a photo-initiator [Lu et al., 2006, Chan et al., 2010, Zorlutuna et al., 2011]. The second one is similar except that the cells are seeded into the material after the 3D hydrogel has been printed [Seol et al., 2013]. These 3D polymerisation techniques achieve a spacial specificity of around 300 to 100 μm horizontally and generally around 25 μm axially.

Recent studies have shown the abilities of an MPLSM for lithography purposes in biocompatible hydrogels. The advantages of the control of the focal point of an MPLSM over the one from a standard 3D printer is its spacial selectivity. Photolithography in hydrogels with an MPLSM allows chemical reactions between the pulsed laser and the hydrogel to be confined to the focal volume of the objective (generally around 1 μm^3). This enables photo-degradation, photo-patterning and photo-polymerisation effects to occur in 3D with an unprecedented spacial accuracy. Furthermore, as most of the MPLSM lasers have a tuneable wavelength, they also offer the possibility to image living cells embedded in those 3D scaffolds. In 2008 , *Kloxin et al.* embedded ATII epithelial cells into multiple closed up hydrogels wells. Upon MPLSM irradiation, photo-degradation was achieved in this specific hydrogel allowing to create canals and hence establish cells connectivity between the different wells. Moreover, they were able to record the structural development of these cells

induced by a change in geometry of their microenvironment [Kloxin et al., 2012]. In 2015, *DeForest et al.* successfully showed that an MPLSM can be used to guide the stem cells fate in a biocompatible 3D micro-environment [Deforest and Tirrell, 2015]. Two years later, in 2017, the same research group was also capable of reproducing micro-vascularisation with an MPLSM [Arakawa et al., 2017]. They used the photo-degradation effect in hydrogels to create micro-canals with a diameter ranging from 10 to 200 μm. Both abilities to guide stem cell fate differentiation and vasculature reproduction were achieved through the use of two-photon microscopy and will play a determining role in the creation of organoids and 4D tissue engineering. As described above and in 1.5, the precise control of an MPSLM focal point allows an accurate spatiotemporal control over a cell culture microenvironment design. Furthermore, it also allows to record the activity (through calcium imaging) and structural development of 3D cell populations. These capabilities can only be achieved with a software that precisely control the location and dwell time of the MPLSM focal point. The two following sections on photo-patterning and photo-degradation in hydrogels are here to show a proof of principle that our customised software achieves these specific features.

5.3.1 Photo-patterning effect

The hydrogel scaffold: 8-arm Polyethylene Glycol (PEG) norbornene (molecular weight 20,000) is partially crosslinked with linear dithiol molecules to create a highly hydrated, 3-dimensional hydrogel network. The reaction between norbornenes and thiols is initiated by a radical reaction - in this case, activation of a photoinitiator that produces radicals under exposure to UV light (365 nm). To validate and visualize a high level of spatial control over patterning in 3-dimensional space, a fluorescently labeled peptide (the cell-adherent RGD peptide, labelled with rhodamine) is photopatterned into hydrogels. Partially crosslinked hydrogels are first formed and swollen in PBS. Then, a solution of RGD peptide and photoinitiator is swollen into the hydrogel, and multiphoton light at 740 nm is used to precisely pattern the RGD into the hydrogel (see Fig.5.5 *A*). Following patterning, unreacted RGD diffuses out of the gel, and patterns are verified using confocal microscopy techniques (see Fig.5.5 *B*

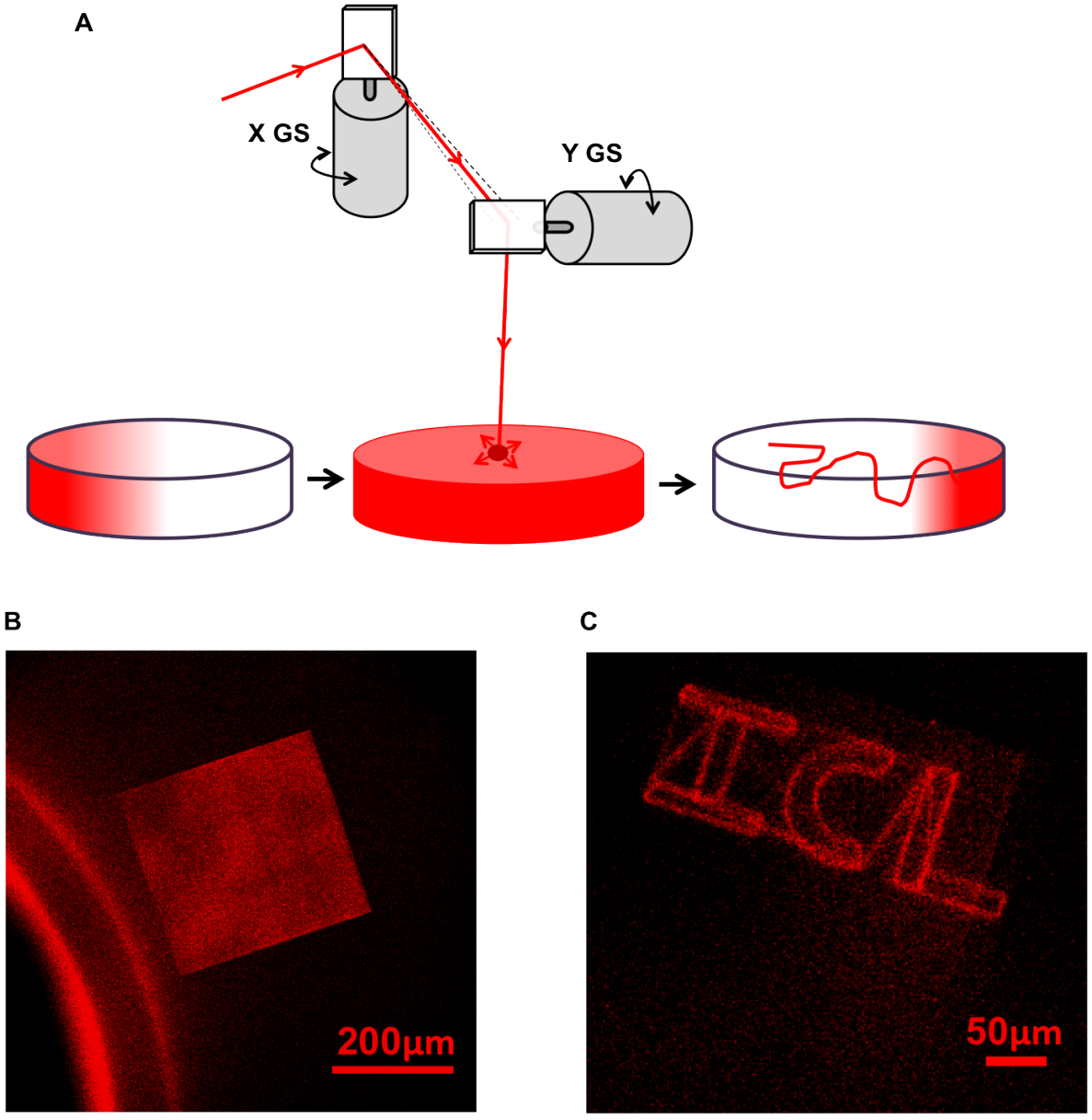


Figure 5.5: Hydrogel two-photon photo-patterning process. *A* Three steps (from the left to the right) schematic representing the two-photon photo-patterning process in hydrogels. First a red-shifted fluorophore is swelled into the hydrogel. Second the photo-patterning effect occurs where the focal point of the MPLSM delivered enough energy to induce a chemical reaction binding the fluorophore to the hydrogel. Third the red fluorophore is swelled out of the hydrogel except in the regions where the photo-patterning effect occurred. *B* High resolution image $750 \times 750\,\mu m^2$ taken with a CLSM showing the photo-patterning effect produced by raster scanning a $300 \times 300\,\mu m^2$ large area (red square) with our MPLSM (red arc caused by a bubble embedded in the hydrogel). *C* Image also taken by a CLSM but this time showing three letters "ICL" initials for Imperial College London that have been photo-patterned into the hydrogel with the GS software control of our MPLSM.

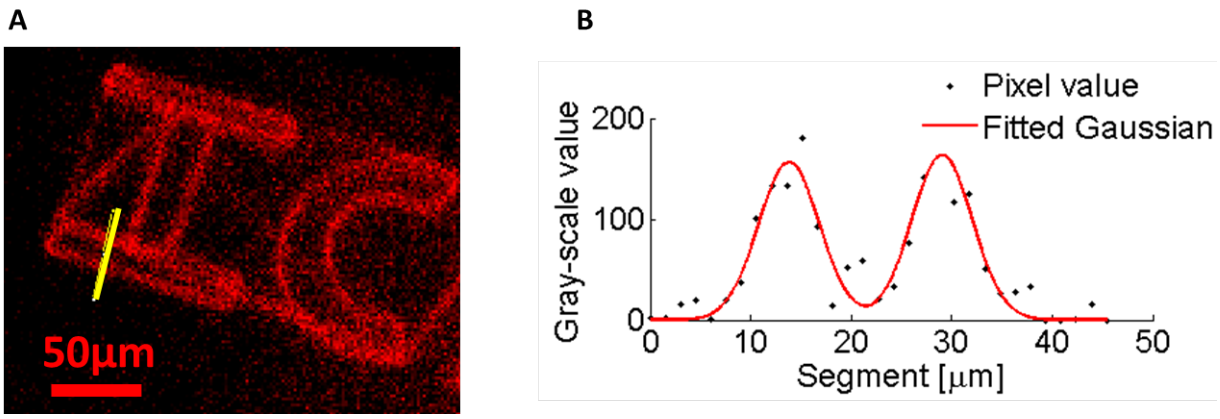


Figure 5.6: Horizontal photo-patterning profile in hydrogel obtained with an MPLSM. *A* Zoom in on the "IC" photo-patterned letters. In yellow the analysed line of pixel values. *B* Horizontal 50 μm pixel grey-scale value profile (black points) (with fitted Gaussian in red) of the yellow line in *A*.

and *C*). The GS software development allowed precise control of the position of the 2-photon focal spot, enabling the ability to draw any kind of two-dimensional pattern in the hydrogel (see Fig.5.5 *B* and *C*). By using line scanning, I was able to photo-pattern the lines "ICL" standing for Imperial College London into the hydrogels, see Fig.5.5 *C*. For the parameters: total pixel dwell time: 10 μs and constant laser power at objective: 68.5 mW), I show that the horizontal precision of the patterning is around 8 μm (see Fig.5.6). These preliminary results inform on the order of magnitude of what can be achieved with a commercial MPLSM in terms of spatial patterning precision. However, further tests need to be established by varying the power and total pixel dwell time parameters to explore the axial and horizontal accuracy achievable with an MPLMS in the photo-patterning chemical processes.

5.3.2 Photo-degradation effect

The photo-degradation effect is shown in an 8-arm PEG maleimide hydrogels (molecular weight 40,000). These gels are crosslinked with a synthesized PEG-based dithiol molecule which includes the o-nitrobenzyl group and cleaves in half by absorbing light at 365 nm (740 nm with two-photon light). This photo-reactive part of the hydrogel was labelled red by adding a small amount of dye (0.05 mM AlexaFluor 546 C5-maleimide) that covalently in-

corporates into the hydrogel. The gel was made on top of a thiol-functionalized glass slide in order to keep it in place, and was equilibrated and swollen in PBS before and after patterning. The assessment of the patterning was performed with an MPLMS using the wavelength 980 nm outside the range of the patterning wavelengths (see Fig.5.7 *A*, *B* and *C*).

Here again, in a similar study as in 5.3.1, I was able with the developed software to pattern different kind of shapes into this specific hydrogels. This allowed me, for a set of hardware parameters (laser power at the objective and total pixel dwell time), to determine the axial and horizontal photo-degradation patterning precision achieved with a commercial MPLSM. Firstly, I show with raster scanning, that the axial patterning increases with longer exposure times. The laser power at the objective was maintained constant at 68.5 mW whereas I increased the total exposure time on $50 \times 50\,\mu\text{m}^2$ square areas from 62 ms to 18 sec (see Fig.5.8 *A* and *B*). This increase in exposure time at constant power expanded the axial photo-degraded area (see Fig.5.8 *B*). For the exposure times: 18 sec, 5 sec and 62 ms, the FWHM of the fitted gaussian to the axial gray-scale pixel value profile was: $25\,\mu$m, $33\,\mu$m and $36\,\mu$m, respectively (see Fig.5.8 *C*, *D* and *E*). Further tests need to be accomplished but I hypothesize that the application of lower powers would enable us to access a tighter patterned cross sections closer to the PSF of the MPLSM. Secondly, I also used arbitrary line scans to pattern the "ICL" letters into the hydrogels enabling me to determine the horizontal spatial precision achieved with a standard MPLSM for the photo-degradation process (see Fig.5.9 *A*). With a total pixel dwell time of $10\,\mu$s and a constant power at the objective of 68.5 mW, I show that the photo-degradation process can be confined in about $2.5\,\mu$m (see Fig.5.9 *A* and *B*). These preliminary results on spatial restrictions of the photo-degradation process in hydrogel scaffolds gives us more information on what type of micro-environment/structures can be achieved for cell cultures.

Further characterization of these photo-degradation and photo-patterning processes will inform us on what type of spatiotemporal 3D micro-environemnt can be achieved in hydrogels with the use of an MPLSM for cell cultures purposes.

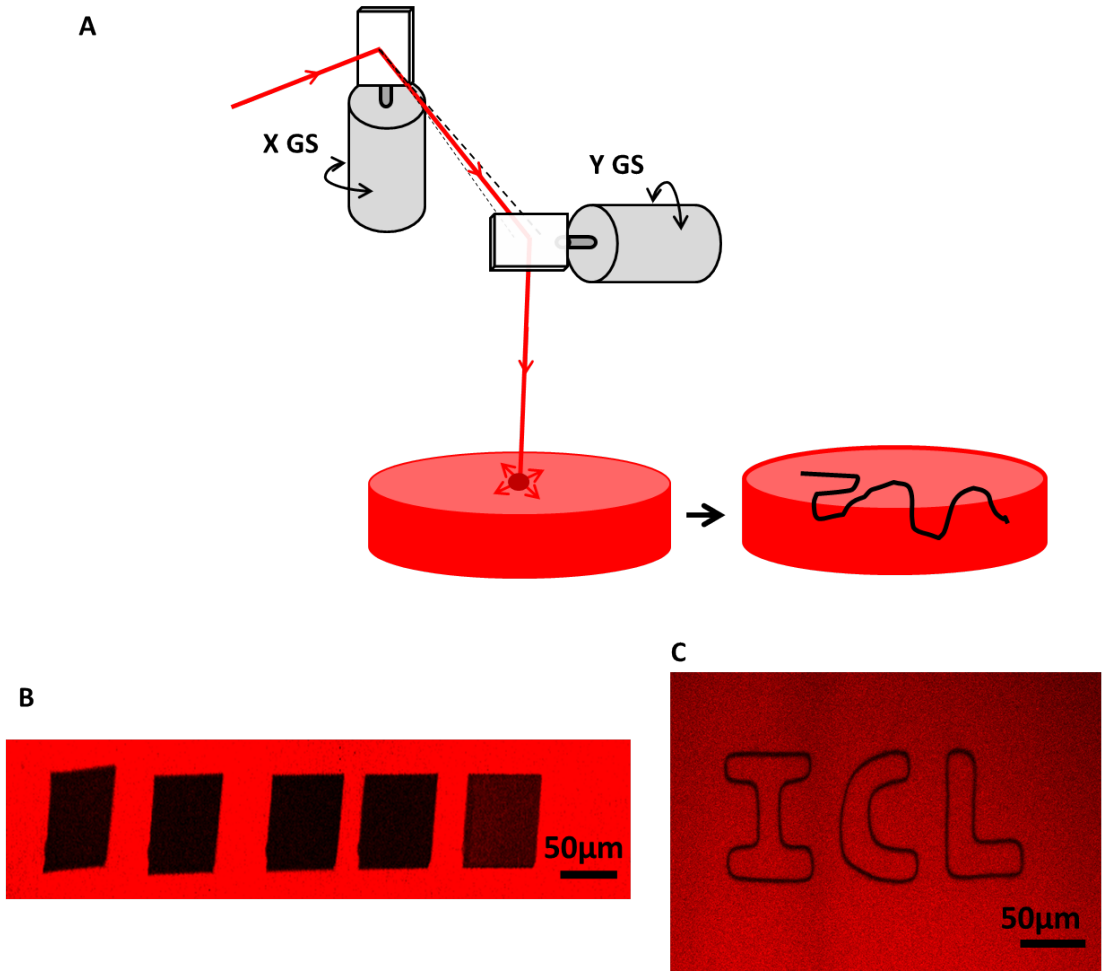


Figure 5.7: MPLSM hydrogel photo-degradation process. *A* Two steps (from the left to the right) schematic representing the two-photon photo-degradation process in hydrogels. First, *B* Axial view (x,z) of five $50 \times 50\,\mu m^2$ photo-patterned squares obtained with raster scanning. From left to right the photo-patterning times are: 18 sec, 10 sec, 5 sec, 1 sec and 62 ms. Each square was photo-degraded with a constant power at the objective: 68.5 mW. *C* Photo-degradation process with arbitrary MPLSM line scanning of the letters "ICL".

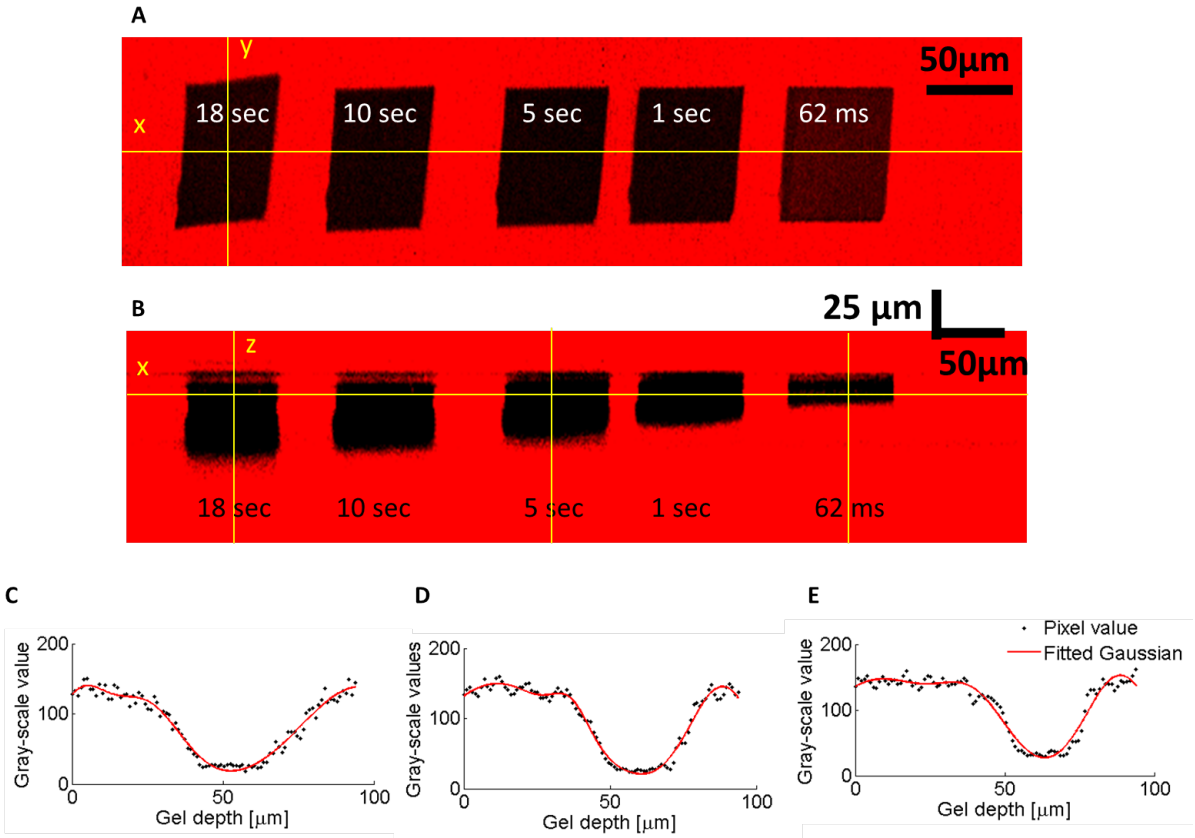


Figure 5.8: Hydrogel two-photon photo-degradation process. *A* Horizontal view (x,y) of five $50 \times 50\,\mu m^2$ photo-patterned squares obtained with raster scanning. From left to right the photo-patterning times are: 18 sec, 10 sec, 5 sec, 1 sec and 62 ms. *B* Axial view (x,z) of five $50 \times 50\,\mu m^2$ photo-patterned squares obtained with raster scanning. From left to right the photo-patterning times are: 18 sec, 10 sec, 5 sec, 1 sec and 62 ms. Each square was photo-degraded with a constant power at the objective: 68.5 mW. *C*, *D* and *E* axial (x,z) grey-scale pixel value profile (black points) over $100\,\mu m$ for a 18 sec, 5 sec and 62 ms photo-degradation process, respectively. A Gaussian fit (red line) was added to each axial grey-scale pixel value profile.

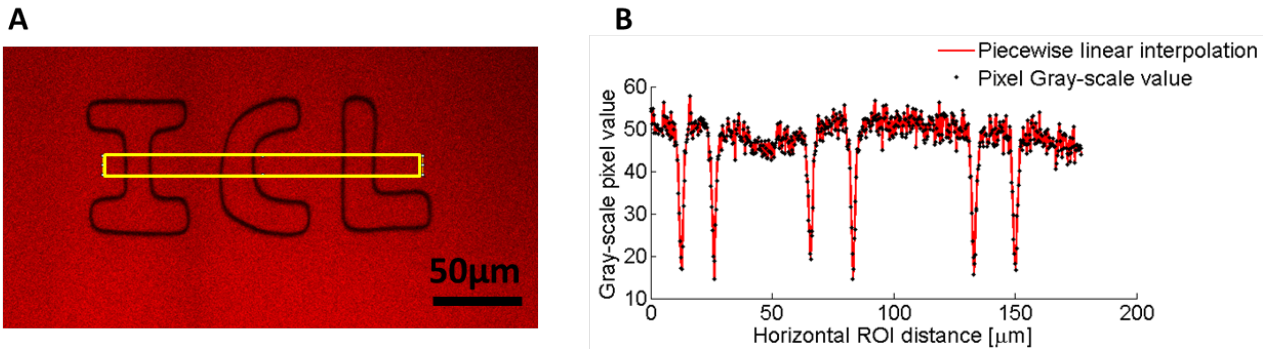


Figure 5.9: Arbitrary line MPLSM photo-degradation process. *A* Horizontal view (x,y) of a photo-degradation process with an arbitrary line method (”ICL”). *B* Horizontal photo-degradation profile obtained with an MPLSM. The gray-scale pixel values (black dots) correspond to the vertical average of the yellow rectangle in *A*. The pixel values were linearly interpolated (red line)giving an estimated size of the photo-degradation chemical reaction.

Chapter 6

Conclusion and future directions

6.1 Summary of thesis achievements

In this thesis, I have explored 2 and 3D scanning of a standard commercial galvanometric scanner MPLSM with an engineering approach, based on improving fast functional calcium imaging of large neural networks. The first step consisted of building a model of the main elements of the experiment. Therefore, I simulated a 2D neural population with a pseudo random distribution where each neuron was associated with an Izhikevitch spike train model. Furthermore, I also simulated the fluorescent signal emitted by these neurons according to their spike trains, and the kinetics of the used fluorescent dye. Finally, I modelled the GSs with a second order differential equation to represent their mechanical properties and the PMT signal acquisition. This simulation platform enabled me to assess the performance of 2D scanning with a standard MPLSM and develop a novel scanning algorithm: SSA, taking into account the mechanical properties of the GSs for fast functional calcium imaging.

This new scanning strategy was then tested and compared to the TSA in real conditions. GSs servo loop positions recordings show that the SSA achieves higher sampling frequencies then the TSA on simulated neural distribution with a density of neurons representative of the ones found in mammalian cortex. Moreover, I show that this result remains true while

scanning a real distribution of mouse hippocampal GCs. I then demonstrated in mouse hippocampal brain slices loaded with the fluorescent dye Cal520-AM that scanning strategies can record spontaneous and evoked activity from a high number of neurons at sampling frequencies one order of magnitude higher than frame scanning. Finally, I assessed the signal quality achieved with scanning strategies and frame scanning by simultaneously acquiring the calcium traces and the electrophysiology traces (whole-cell patch). Using the CRB as a metric of signal quality, we demonstrate the weight of CSF and SNR for temporal precision in calcium imaging data.

Another achievement of this thesis is the extension of scanning strategies to the relatively unexplored third dimension. I broadened the simulation platform by incorporating an ETL model giving rise to the development of two new 3D scanning algorithms: cylindrical and orbital scanning strategies. A preliminary hardware validation of this technique was achieved by imaging the moving focal spot of the MPLSM with a high speed camera.

Finally, I show that the control of the two-photon focal spot in 3D can also be used in "click-based" hydrogels, illustrated in this case with the photo-patterning and photo-degradation effect.

6.2 Future directions

On a technological aspect, a collaboration with Cambridge Technology could lead to a more complete GS model including the servo loop. This model, if linear, could be used with optimal control theory taking into consideration acquisition speed and SNR to find a closer solution to the optimal 2D scanning path. In 3D, as described in 4.7, further trajectory precision assessments need to be performed. Both 2 and 3D scanning strategies will then be usable in every standard MPLSM on *in vitro* preparations. However, further work needs to be done to apply them *in vivo* as movement artifact caused by e.g the heart beat of the animal could disrupt the acquisition. A potential solution to this problem would be to use an FPGA to have an almost instantaneous online image movement correction algorithm. These solu-

tions are very low cost and have the potential to bring every standard commercial MPLSM to high performances regarding functional calcium imaging.

If these scanning strategies become standard for imaging 100's of cells with a regular MPLSM, they can not compete with new optical developments of scanless microscopes. Temporal focusing for instance, enables through temporal manipulation of the laser pulse, the creation of on axis light sheets. This technique when coupled to a fast z-focus optical element like an ETL or a piezo actuator can achieves unprecedented functional calcium imaging volume rates of 1000's of cells [Schrödel et al., 2013, Jiang et al., 2015]. This method however does not allow much flexibility when only specific ROIs e.g somas, dendrites need to be imaged or stimulated. The recent development of Computer Generated Holography (CGH) allows to 'scuplt' the light so that entire ROIs can be illuminated simultaneously. This imaging technique uses Spatial Light Modulators (SLM) to manipulate the phase profile of the pulsed laser. These SLMs are typically based of liquid crystal on silicon and achieve a refreshing rate of 10 to 100 Hz of successive different imaged patterns. The improvement of the refreshing rate to change imaged or stimulated patterns with CGH is in development e.g *Hoy et al. 2015* report switching rates of 1 kHz satisfying the timescale of single APs [Christopher, 2015]. This new SLM technology from *Hoy et al. 2015* remains to be tested for imaging and optogenetics stimulation in deep scattering brain tissues. CGH also offers high spacial specificity. *Foust et al. 2015* show that they achieved to record fluorescence signal from voltage sensitive dyes with high SNR by restricting the CGH pattern to neurons or dendrites [Foust et al., 2015]. This high spatial specificity together with the possibility of recording or stimulating a large population of neurons simultaneously offers new perspective in functional fluorescence imaging. However, CGH (and this also applies to temporally focused light sheets) only achieve to image or stimulate up until -100 to -300 μm under the surface of brain tissues [Bouchard et al., 2015]. Furthermore, despite its advantages, CGH tends to not be used by every biologist for functional fluorescence imaging as this technique requires very expensive hardware to be added to standard MPLSMs and customized softwares which are still not widespread commercially to be used.

The translation from noisy calcium traces acquired with a standard MPLSM into the

original neuron's spike train has been the subject of many studies. Different signal analyses methods have been used to achieve this goal. Template matching [Onativia et al., 2013], deconvolution [Vogelstein et al., 2009] and approximate bayesian inference [Pnevmatikakis et al., 2016] are all based on generative calcium signal template which assumes a strong correlation between one AP and the signal shape of the associated calcium transient [Theis et al., 2015]. Recently, *Theis et al 2015* developed a new technique to infer spikes from calcium traces based on supervised learning in flexible probabilistic models [Theis et al., 2015]. This study is a first step towards the generalization of functional calcium imaging analyses as it takes into account a relatively large data sets of calcium signals coming from different scanning techniques, different cell types and different fluorophores. Other metrics like the CRB can also be used across data sets in a similar manner. The latter allows to estimate the lower bound of the timing uncertainty between the calcium transient onset and the AP. It can be used on signals coming from different neurons, different dyes and different scanning techniques i.e signals with different sampling frequencies and SNRs. Signals analyses tools on inferring the AP trains from the calcium signals should not be neglected and it should match the development of new imaging techniques as it is a major bottleneck to understand the computational processes occurring in large neural networks.

On a more biological aspect, future *in vitro* analyses can be done with functional calcium imaging in the DG on the microcircuit level. In the continuity of the preliminary results, a complete characterization of DGC spontaneous activity throughout their first month of development in wild type mice can be achieved and would provide further insight into how spontaneous activity plays a role in building the adult dentate granular layer. The same study can be carried out in adult animals to explore how spontaneous activity can impact on the fate of adult newborn GCs. Furthermore, more abstract functionality of the DG can be investigated *in vitro*. Through spatially separated PP input or PP input with variation of similarities, it could be possible to study the calcium functional signal of the granular layer on a mesoscale level with single cell sensitivity and determine whether the circuit is encoding pattern separation processes. The higher level of functionality of the DG can further be compared with aged matched neurodegenerative mouse models to gain some insights into the studied disease.

Bibliography

[Opt, 2014] (2014). *Datasheet: EL-10-30-Series*. Optotune AG.

[Abrous and Wojtowicz, 2015] Abrous, D. N. and Wojtowicz, J. M. (2015). Interaction between Neurogenesis and Hippocampal Memory System: New Vistas. *Cold Spring Harbor perspectives in biology*, 7(6).

[Agmon and Connors, 1991] Agmon, A. and Connors, B. W. (1991). Thalamocortical responses of mouse somatosensory (barrel) cortex in vitro. *Neuroscience*, 41(2-3):365–379.

[Ahrens et al., 2013] Ahrens, M. B., Orger, M. B., Robson, D. N., Li, J. M., and Keller, P. J. (2013). Whole-brain functional imaging at cellular resolution using light-sheet microscopy. *Nature Methods*, 10(5):413–420.

[Arakawa et al., 2017] Arakawa, C. K., Badeau, B. A., Zheng, Y., and DeForest, C. A. (2017). Multicellular Vascularized Engineered Tissues through User-Programmable Biomaterial Photodegradation. *Advanced Materials*, 29(37).

[Ashley and Ridgway, 1968] Ashley, C. and Ridgway, E. (1968). Simultaneous recording of membrane potential, calcium transient and tension in single muscle fibers. *Nature*, 219:1168–1169.

[Ben-Ari et al., 1989] Ben-Ari, Y., Cherubini, E., Corradetti, R., and Gaiarsa, J. L. (1989). Giant synaptic potentials in immature rat CA3 hippocampal neurones. *The Journal of physiology*, 416:303–325.

[Berridge et al., 2000] Berridge, M. J., Lipp, P., and Bootman, M. D. (2000). The versatility and universality of calcium signalling. *Nature reviews. Molecular cell biology*, 1(1):11–21.

[Berron et al., 2016] Berron, D., Schütze, H., Maass, A., Cardenas-Blanco, A., Kuijf, H. J., Kumaran, D., and Düzel, E. (2016). Strong Evidence for Pattern Separation in Human Dentate Gyrus. *The Journal of Neuroscience*, 36(29):7569–7579.

[Bouchard et al., 2015] Bouchard, M. B., Voleti, V., Mendes, C. S., Lacefield, C., Grueber, W. B., Mann, R. S., Bruno, R. M., and Hillman, E. M. C. (2015). Swept confocally-aligned planar excitation (SCAPE) microscopy for high speed volumetric imaging of behaving organisms. *Nat Photonics*, 9(2):113–119.

[Brown et al., 1975] Brown, J. E., Cohen, L. B., De Weer, P., Pinto, L. H., Ross, W. N., and Salzberg, B. M. (1975). Rapid changes in intracellular free calcium concentration. Detection by metallochromic indicator dyes in squid giant axon. *Biophysical journal*, 15(11):1155–60.

[Chan et al., 2010] Chan, V., Zorlutuna, P., Jeong, J. H., Kong, H., and Bashir, R. (2010). Three-dimensional photopatterning of hydrogels using stereolithography for long-term cell encapsulation. *Lab on a Chip*, 10(16):2062.

[Chapman and Robbins, 1951] Chapman, D. G. and Robbins, H. (1951). Minimum Variance Estimation Without Regularity Assumptions. *Ann Math Stat*, 22(4):581–586.

[Chen et al., 2013] Chen, T.-W., Wardill, T. J., Sun, Y., Pulver, S. R., Renninger, S. L., Baohan, A., Schreiter, E. R., Kerr, R. A., Orger, M. B., Jayaraman, V., Looger, L. L., Svoboda, K., and Kim, D. S. (2013). Ultrasensitive fluorescent proteins for imaging neuronal activity. *Nature*, 499(7458):295–300.

[Cheng et al., 2011] Cheng, A., Gonçalves, J. T., Golshani, P., Arisaka, K., and Portera-Cailliau, C. (2011). Simultaneous two-photon calcium imaging at different depths with spatiotemporal multiplexing. *Nat Methods*, 8(2):139–142.

[Chris Xu, 1996] Chris Xu, W. W. W. (1996). Measurement of two-photon excitation cross sections of molecular fluorophores with data from 690 to 1050 nm. *J. Opt. Soc. Am. B*.

[Christopher, 2015] Christopher, H. (2015). In Vivo Neural Imaging SLMs for Conducting 3D Holography inside Living Brains. *Biophotonics*.

[Cossart et al., 2003] Cossart, R., Aronov, D., and Yuste, R. (2003). Attractor dynamics of network UP states in the neocortex. *Nature*, 423(6937):283–288.

[Cruikshank et al., 2002] Cruikshank, S. J., Rose, H. J., and Metherate, R. (2002). Auditory thalamocortical synaptic transmission in vitro. *Journal of neurophysiology*, 87(1):361–384.

[Deforest and Tirrell, 2015] Deforest, C. A. and Tirrell, D. A. (2015). A photoreversible protein-patterning approach for guiding stem cell fate in three-dimensional gels. *Nature Materials*, 14(5):523–531.

[Denk et al., 1990] Denk, W., Strickler, J. H., and Webb, W. W. (1990). Two-photon laser scanning fluorescence microscopy. *Science*, 248(4951):73–76.

[Denny et al., 2014] Denny, C. A., Kheirbek, M. A., Alba, E. L., Tanaka, K. F., Brachman, R. A., Laughman, K. B., Tomm, N. K., Turi, G. F., Losonczy, A., and Hen, R. (2014). Hippocampal memory traces are differentially modulated by experience, time, and adult neurogenesis. *Neuron*, 83(1):189–201.

[Ducros et al., 2013] Ducros, M., Houssen, Y. G., Bradley, J., de Sars, V., and Charpak, S. (2013). Encoded multisite two-photon microscopy. *Proc Natl Acad Sci U S A*, 110(32):13138–13143.

[Economo et al., 2016] Economo, M. N., Clack, N. G., Lavis, L. D., Gerfen, C. R., Svoboda, K., Myers, E. W., and Chandrashekar, J. (2016). A platform for brain-wide imaging and reconstruction of individual neurons. *eLife*, 5(JANUARY2016).

[Foust et al., 2015] Foust, A. J., Zampini, V., Tanese, D., Papagiakoumou, E., and Emiliani, V. (2015). Computer-generated holography enhances voltage dye fluorescence discrimination in adjacent neuronal structures. *Neurophotonics*, 2(2):21007.

[Frye and MacLean, 2016] Frye, C. G. and MacLean, J. N. (2016). Spontaneous activations follow a common developmental course across primary sensory areas in mouse neocortex. *Journal of neurophysiology*, 116(2):431–437.

[Fuchs et al., 2002] Fuchs, E., Jaffe, J., Long, R., and Azam, F. (2002). Thin laser light sheet microscope for microbial oceanography. *Optics express*, 10(2):145–54.

[Gaarskjaer, 1978] Gaarskjaer, F. (1978). Organization of the mossy fiber system of the rat studied in extended hippocampi. I. Terminal area related to number of granule and pyramidal cells. *Journal of Comparative Neurology*, (203):717–735.

[Gerald F. Marshall, 2012] Gerald F. Marshall, G. E. S. (2012). *Handbook of Optical and Laser Scanning*, volume Second Edi.

[Goebel et al., 2007] Goebel, W., Kampa, B. M., and Helmchen, F. (2007). Imaging cellular network dynamics in three dimensions using fast 3D laser scanning. *Nat Methods*, 4(1):73–79.

[Gonçalves et al., 2016] Gonçalves, J. T., Schafer, S. T., and Gage, F. H. (2016). Adult Neurogenesis in the Hippocampus: From Stem Cells to Behavior. *Cell*, 167(4):897–914.

[Gong et al., 2015] Gong, Y., Huang, C., Li, J. Z., Grewe, B. F., Zhang, Y., Eismann, S., and Schnitzer, M. J. (2015). High-speed recording of neural spikes in awake mice and flies with a fluorescent voltage sensor. *Science (New York, N.Y.)*, 350(6266):1361–1366.

[Göppert-Mayer, 1931] Göppert-Mayer, M. (1931). Über Elementarakte mit zwei Quantensprüngen. *Ann. Phys*.

[Grewe et al., 2011] Grewe, B. F., Voigt, F. F., van 't Hoff, M., and Helmchen, F. (2011). Fast two-layer two-photon imaging of neuronal cell populations using an electrically tunable lens. *Biomed Opt Express*, 2(7):2035–2046.

[Grienberger and Konnerth, 2012] Grienberger, C. and Konnerth, A. (2012). Imaging calcium in neurons. *Neuron*, 73(5):862–885.

[Gutierrez, 2016] Gutierrez, R. (2016). The plastic neurotransmitter phenotype of the hippocampal granule cells and of the moss in their messy fibers. *Journal of Chemical Neuroanatomy*, 73:9–20.

[Hamad et al., 2015] Hamad, M. I. K., Krause, M., and Wahle, P. (2015). Improving AM ester calcium dye loading efficiency. *J Neurosci Methods*, 240:48–60.

[Hammersley, 1950] Hammersley, J. (1950). On Estimating Restricted Parameters. *Journal of the Royal Statistical Society*, 12:192–240.

[Hargreaves, 2005] Hargreaves, E. L. (2005). Major Dissociation Between Medial and Lateral Entorhinal Input to Dorsal Hippocampus. *Science*, 308(5729):1792–1794.

[Houser, 2007] Houser, C. R. (2007). Interneurons of the dentate gyrus: an overview of cell types, terminal fields and neurochemical identity.

[Hunsaker et al., 2007] Hunsaker, M. R., Mooy, G. G., Swift, J. S., and Kesner, R. P. (2007). Dissociations of the medial and lateral perforant path projections into dorsal DG, CA3, and CA1 for spatial and nonspatial (visual object) information processing. *Behavioral Neuroscience*, 121(4):742–750.

[Hyde and Strowbridge, 2012] Hyde, R. A. and Strowbridge, B. W. (2012). Mnemonic representations of transient stimuli and temporal sequences in the rodent hippocampus in vitro. *Nature neuroscience*, 15(10):1430–1438.

[Izhikevich, 2003] Izhikevich, E. M. (2003). Simple model of spiking neurons. *IEEE Trans Neural Netw*, 14(6):1569–1572.

[Jiang et al., 2015] Jiang, J., Zhang, D., Walker, S., Gu, C., Ke, Y., Yung, W. H., and Chen, S.-c. (2015). Fast 3-D temporal focusing microscopy using an electrically tunable lens. *Optics Express*, 23(19):24362.

[Kampa et al., 2011] Kampa, B. M., Roth, M. M., Göbel, W., and Helmchen, F. (2011). Representation of visual scenes by local neuronal populations in layer 2/3 of mouse visual cortex. *Front Neural Circuits*, 5:18.

[Katona et al., 2012] Katona, G., Szalay, G., Maák, P., Kaszás, A., Veress, M., Hillier, D., Chiovini, B., Vizi, E. S., Roska, B., and Rózsa, B. (2012). Fast two-photon in vivo imaging with three-dimensional random-access scanning in large tissue volumes. *Nat Methods*, 9(2):201–208.

[Kempermann et al., 1997] Kempermann, G., Kuhn, H. G., and Gage, F. H. (1997). More hippocampal neurons in adult mice living in an enriched environment. *Nature*, 386(6624):493–495.

[Kesner, 2007] Kesner, R. P. (2007). A behavioral analysis of dentate gyrus function. *Progress in Brain Research*, 163:567–576.

[Kloxin et al., 2012] Kloxin, A. M., Lewis, K. J. R., DeForest, C. A., Seedorf, G., Tibbitt, M. W., Balasubramaniam, V., and Anseth, K. S. (2012). Responsive culture platform to examine the influence of microenvironmental geometry on cell function in 3D. *Integrative biology : quantitative biosciences from nano to macro*, 4(12):1540–1549.

[Knöpfel et al., 2015] Knöpfel, T., Gallero-Salas, Y., and Song, C. (2015). Genetically encoded voltage indicators for large scale cortical imaging come of age. *Current opinion in chemical biology*, 27:75–83.

[Kolb and Sharpless, 2003] Kolb, H. C. and Sharpless, K. B. (2003). The growing impact of click chemistry on drug discovery. *Drug discovery today*, 8(24):1128–1137.

[Kovacs, 2008] Kovacs, A. (2008). Scanning strategies for imaging arrays. *Proc. SPIE*, 702007.

[Lee et al., 2008] Lee, S.-H., Moon, J. J., and West, J. L. (2008). Three-dimensional micropatterning of bioactive hydrogels via two-photon laser scanning photolithography for guided 3D cell migration. *Biomaterials*, 29(20):2962–2968.

[Leutgeb et al., 2007] Leutgeb, J. K., Leutgeb, S., Moser, M.-B., and Moser, E. I. (2007). Pattern separation in the dentate gyrus and CA3 of the hippocampus. *Science (New York, N.Y.)*, 315(5814):961–966.

[Lillis et al., 2008] Lillis, K. P., Eng, A., White, J. A., and Mertz, J. (2008). Two-photon imaging of spatially extended neuronal network dynamics with high temporal resolution. *J Neurosci Methods*, 172(2):178–184.

[Liu et al., 2012] Liu, X., Ramirez, S., Pang, P. T., Puryear, C. B., Govindarajan, A., Deisseroth, K., and Tonegawa, S. (2012). Optogenetic stimulation of a hippocampal engram activates fear memory recall. *Nature*, 484(7394):381–385.

[Lopez-Rojas and Kreutz, 2016] Lopez-Rojas, J. and Kreutz, M. R. (2016). Mature granule cells of the dentate gyrus–Passive bystanders or principal performers in hippocampal function? *Neuroscience and biobehavioral reviews*, 64:167–174.

[Lu et al., 2006] Lu, Y., Mapili, G., Suhali, G., Chen, S., and Roy, K. (2006). A digital micromirror device-based system for the microfabrication of complex, spatially patterned tissue engineering scaffolds. *Journal of Biomedical Materials Research - Part A*, 77(2):396–405.

[MacLean et al., 2006] MacLean, J. N., Fenstermaker, V., Watson, B. O., and Yuste, R. (2006). A visual thalamocortical slice. *Nat Methods*, 3(2):129–134.

[Marrone et al., 2011] Marrone, D. F., Adams, A. A., and Satvat, E. (2011). Increased pattern separation in the aged fascia dentata. *Neurobiology of aging*, 32(12):2317.e23—-2317.e32.

[Mauleon et al., 2013] Mauleon, G., Lo, J. F., Peterson, B. L., Fall, C. P., and Eddington, D. T. (2013). Enhanced loading of Fura-2/AM calcium indicator dye in adult rodent brain slices via a microfluidic oxygenator. *Journal of Neuroscience Methods*, 216(2):110–117.

[Neher, 1995] Neher, E. (1995). The use of fura-2 for estimating Ca buffers and Ca fluxes. *Neuropharmacology*, 34(11):1423–1442.

[Neunuebel and Knierim, 2012] Neunuebel, J. P. and Knierim, J. J. (2012). Spatial firing correlates of physiologically distinct cell types of the rat dentate gyrus. *The Journal of neuroscience : the official journal of the Society for Neuroscience*, 32(11):3848–3858.

[Nikolenko et al., 2007] Nikolenko, V., Poskanzer, K. E., and Yuste, R. (2007). Two-photon photostimulation and imaging of neural circuits. *Nat Methods*, 4(11):943–950.

[Nikolenko et al., 2008] Nikolenko, V., Watson, B. O., Araya, R., Woodruff, A., Peterka, D. S., and Yuste, R. (2008). SLM Microscopy: Scanless Two-Photon Imaging and Photostimulation with Spatial Light Modulators. *Frontiers in neural circuits*, 2:5.

[Ninkovic et al., 2007] Ninkovic, J., Mori, T., and Götz, M. (2007). Distinct modes of neuron addition in adult mouse neurogenesis. *The Journal of neuroscience : the official journal of the Society for Neuroscience*, 27(40):10906–10911.

[Obien et al., 2014] Obien, M. E. J., Deligkaris, K., Bullmann, T., Bakkum, D. J., and Frey, U. (2014). Revealing neuronal function through microelectrode array recordings. *Front Neurosci*, 8:423.

[Onativia et al., 2013] Onativia, J., Schultz, S. R., and Dragotti, P. L. (2013). A finite rate of innovation algorithm for fast and accurate spike detection from two-photon calcium imaging. *Journal of Neural Engineering*, 10(4):46017.

[Oron et al., 2005] Oron, D., Tal, E., and Silberberg, Y. (2005). Scanningless depth-resolved microscopy. *Optics Express*, 13(5):1468.

[Otsu et al., 2008] Otsu, Y., Bormuth, V., Wong, J., Mathieu, B., Dugue, G. P., Feltz, A., and Dieudonne, S. (2008). Optical monitoring of neuronal activity at high frame rate with a digital random-access multiphoton (RAMP) microscope. *J Neurosci Methods*, 173(2):259–270.

[Palero et al., 2010] Palero, J., Santos, S. I. C. O., Artigas, D., and Loza-Alvarez, P. (2010). A simple scanless two-photon fluorescence microscope using selective plane illumination. *Optics express*, 18(8):8491–8498.

[Pedroni et al., 2014] Pedroni, A., Minh, D. D., Mallamaci, A., and Cherubini, E. (2014). Electrophysiological characterization of granule cells in the dentate gyrus immediately after birth. *Frontiers in cellular neuroscience*, 8:44.

[Per Andersen Richard Morris, 2007] Per Andersen Richard Morris, D. A. T. B. J. O. (2007). *The Hippocampus Book*.

[Pilz et al., 2016] Pilz, G.-A., Carta, S., Stäuble, A., Ayaz, A., Jessberger, S., and Helmchen, F. (2016). Functional Imaging of Dentate Granule Cells in the Adult Mouse Hippocampus. *The Journal of neuroscience : the official journal of the Society for Neuroscience*, 36(28):7407–7414.

[Pnevmatikakis et al., 2016] Pnevmatikakis, E. A., Soudry, D., Gao, Y., Machado, T. A., Merel, J., Pfau, D., Reardon, T., Mu, Y., Lacefield, C., Yang, W., Ahrens, M., Bruno, R., Jessell, T. M., Peterka, D. S., Yuste, R., and Paninski, L. (2016). Simultaneous Denoising, Deconvolution, and Demixing of Calcium Imaging Data. *Neuron*, 89(2):299.

[Podgorski and Ranganathan, 2016] Podgorski, K. and Ranganathan, G. (2016). Brain heating induced by near-infrared lasers during multiphoton microscopy. *Journal of Neurophysiology*, 116(3):1012–1023.

[Pologruto et al., 2003] Pologruto, T. A., Sabatini, B. L., and Svoboda, K. (2003). ScanImage: flexible software for operating laser scanning microscopes. *Biomed Eng Online*, 2:13.

[Poucet, 1989] Poucet, B. (1989). Object exploration, habituation, and response to a spatial change in rats following septal or medial frontal cortical damage. *Behavioral neuroscience*, 103(5):1009–16.

[Quirin et al., 2014] Quirin, S., Jackson, J., Peterka, D. S., and Yuste, R. (2014). Simultaneous imaging of neural activity in three dimensions. *Front Neural Circuits*, 8:29.

[Rapp and Gallagher, 1996] Rapp, P. R. and Gallagher, M. (1996). Preserved neuron number in the hippocampus of aged rats with spatial learning deficits. *Proceedings of the National Academy of Sciences*, 93(18):9926–9930.

[Redondo et al., 2014] Redondo, R. L., Kim, J., Arons, A. L., Ramirez, S., Liu, X., and Tonegawa, S. (2014). Bidirectional switch of the valence associated with a hippocampal contextual memory engram. *Nature*, 513(7518):426–430.

[Reynolds et al., 2015] Reynolds, S., Oñativia, J., Copeland, C. S., Schultz, S. R., and Dragotti, P. L. (2015). Spike detection using FRI methods and protein calcium sensors: Performance analysis and comparisons. In *Proc. Int. Conf. Sampling Theory and Applications (SampTA)*, pages 533–537.

[Rochefort et al., 2009] Rochefort, N. L., Garaschuk, O., Milos, R.-I., Narushima, M., Marandi, N., Pichler, B., Kovalchuk, Y., and Konnerth, A. (2009). Sparsification of neuronal activity in the visual cortex at eye-opening. *Proceedings of the National Academy of Sciences of the United States of America*, 106(35):15049–15054.

[Ryan et al., 2015] Ryan, T. J., Roy, D. S., Pignatelli, M., Arons, A., and Tonegawa, S. (2015). Engram cells retain memory under retrograde amnesia. *Science*, 348(6238):1007–1013.

[Sadovsky et al., 2011] Sadovsky, A. J., Kruskal, P. B., Kimmel, J. M., Ostmeyer, J., Neubauer, F. B., and MacLean, J. N. (2011). Heuristically optimal path scanning for high-speed multiphoton circuit imaging. *J Neurophysiol*, 106(3):1591–1598.

[Sakamoto et al., 2014] Sakamoto, M., Kageyama, R., and Imayoshi, I. (2014). The functional significance of newly born neurons integrated into olfactory bulb circuits. *Frontiers in neuroscience*, 8:121.

[Santoro, 2013] Santoro, A. (2013). Reassessing pattern separation in the dentate gyrus. *Frontiers in behavioral neuroscience*, 7:96.

[Sato et al., 2007] Sato, T. R., Gray, N. W., Mainen, Z. F., and Svoboda, K. (2007). The functional microarchitecture of the mouse barrel cortex. *PLoS biology*, 5(7):e189.

[Scharfman, 1994] Scharfman, H. E. (1994). Evidence from simultaneous intracellular recordings in rat hippocampal slices that area CA3 pyramidal cells innervate dentate hilar mossy cells. *Journal of neurophysiology*, 72(5):2167–80.

[Scharfman, 1995] Scharfman, H. E. (1995). Electrophysiological evidence that dentate hilar mossy cells are excitatory and innervate both granule cells and interneurons. *Journal of Neurophysiology*, 74(1):179–194.

[Scharfman, 2007] Scharfman, H. E., editor (2007). *The Dentate Gyrus: A comprehensive guide to structure, function, and clinical implications*, volume 163.

[Scharfman and Myers, 2013] Scharfman, H. E. and Myers, C. E. (2013). Hilar mossy cells of the dentate gyrus: a historical perspective. *Frontiers in Neural Circuits*, 6.

[Schlessinger et al., 1975] Schlessinger, A. R., Cowan, W. M., and Gottlieb, D. I. (1975). An autoradiographic study of the time of origin and the pattern of granule cell migration in the dentate gyrus of the rat. *The Journal of comparative neurology*, 159(2):149–175.

[Schrödel et al., 2013] Schrödel, T., Prevedel, R., Aumayr, K., Zimmer, M., and Vaziri, A. (2013). Brain-wide 3D imaging of neuronal activity in Caenorhabditis elegans with sculpted light. *Nature Methods*, 10(10):1013–1020.

[Schuck et al., 2014] Schuck, R., Annecchino, L. A., and Schultz, S. R. (2014). Scaling up multiphoton neural scanning: the SSA algorithm. *Conf Proc IEEE Eng Med Biol Soc*, 2014:2837–2840.

[Schuck et al., 2015] Schuck, R., Quicke, P., Copeland, C., Garasto, S., Annecchino, L. A., Hwang, J. K., and Schultz, S. R. (2015). Rapid three dimensional two photon neural population scanning. *Conf Proc IEEE Eng Med Biol Soc*, 2015:5867–5870.

[Schultz et al., 2017] Schultz, S. R., Copeland, C. S., Foust, A. J., Quicke, P., and Schuck, R. (2017). Advances in Two-Photon Scanning and Scanless Microscopy Technologies for Functional Neural Circuit Imaging. *Proceedings of the IEEE*, 105(1):139–157.

[Schultz et al., 2009] Schultz, S. R., Kitamura, K., Post-Uiterweer, A., Krupic, J., and Häusser, M. (2009). Spatial pattern coding of sensory information by climbing fiber-evoked calcium signals in networks of neighboring cerebellar Purkinje cells. *The Journal of neuroscience : the official journal of the Society for Neuroscience*, 29(25):8005–8015.

[Schwartz and Coleman, 1981] Schwartz, S. P. and Coleman, P. D. (1981). Neurons of origin of the perforant path. *Experimental neurology*, 74(1):305–312.

[Sederberg et al., 2015] Sederberg, A. J., Palmer, S. E., and MacLean, J. N. (2015). Decoding thalamic afferent input using microcircuit spiking activity. *Journal of neurophysiology*, 113(7):2921–2933.

[Seol et al., 2013] Seol, Y. J., Park, D. Y., Park, J. Y., Kim, S. W., Park, S. J., and Cho, D. W. (2013). A new method of fabricating robust freeform 3D ceramic scaffolds for bone tissue regeneration. *Biotechnology and Bioengineering*, 110(5):1444–1455.

[Siegel et al., 2012] Siegel, F., Heimel, J. A., Peters, J., and Lohmann, C. (2012). Peripheral and central inputs shape network dynamics in the developing visual cortex in vivo. *Current biology : CB*, 22(3):253–258.

[Sofroniew et al., 2016] Sofroniew, N. J., Flickinger, D., King, J., and Svoboda, K. (2016). A large field of view two-photon mesoscope with subcellular resolution for in vivo imaging. *eLife*, 5(JUN2016).

[Sohya et al., 2007] Sohya, K., Kameyama, K., Yanagawa, Y., Obata, K., and Tsumoto, T. (2007). GABAergic neurons are less selective to stimulus orientation than excitatory neurons in layer II/III of visual cortex, as revealed by in vivo functional Ca2+ imaging in transgenic mice. *The Journal of neuroscience : the official journal of the Society for Neuroscience*, 27(8):2145–2149.

[Son et al., 2015] Son, Y., Lee, H. J., Kim, J., Shin, H., Choi, N., Lee, C. J., Yoon, E.-S., Yoon, E., Wise, K. D., Kim, T. G., and Cho, I.-J. (2015). In vivo optical modulation of neural signals using monolithically integrated two-dimensional neural probe arrays. *Sci Rep*, 5:15466.

[Soriano and Frotscher, 1994] Soriano, E. and Frotscher, M. (1994). Mossy cells of the rat fascia dentata are glutamate-immunoreactive. *Hippocampus*, 4(1):65–69.

[Stosiek et al., 2003] Stosiek, C., Garaschuk, O., Holthoff, K., and Konnerth, A. (2003). In vivo two-photon calcium imaging of neuronal networks. *Proc Natl Acad Sci U S A*, 100(12):7319–7324.

[Tada et al., 2014] Tada, M., Takeuchi, A., Hashizume, M., Kitamura, K., and Kano, M. (2014). A highly sensitive fluorescent indicator dye for calcium imaging of neural activity in vitro and in vivo. *Eur J Neurosci*, 39(11):1720–1728.

[Tan et al., 1999] Tan, Y. P., Llano, I., Hopt, A., Würriehausen, F., and Neher, E. (1999). Fast scanning and efficient photodetection in a simple two-photon microscope. *J Neurosci Methods*, 92(1-2):123–135.

[Theis et al., 2015] Theis, L., Berens, P., Froudarakis, E., Reimer, J., Roman-Roson, M., Baden, T., Euler, T., Tolias, A., and Bethge, M. (2015). Supervised learning sets benchmark for robust spike detection from calcium imaging signals. *bioRxiv*, page 010777.

[Tian et al., 2009] Tian, L., Hires, S. A., Mao, T., Huber, D., Chiappe, M. E., Chalasani, S. H., Petreanu, L., Akerboom, J., McKinney, S. A., Schreiter, E. R., Bargmann, C. I., Jayaraman, V., Svoboda, K., and Looger, L. L. (2009). Imaging neural activity in worms, flies and mice with improved GCaMP calcium indicators. *Nature Methods*, 6(12):875–881.

[Ting et al., 2014] Ting, J. T., Daigle, T. L., Chen, Q., and Feng, G. (2014). Acute brain slice methods for adult and aging animals: application of targeted patch clamp analysis and optogenetics. *Methods in molecular biology (Clifton, N.J.)*, 1183:221–242.

[Tischbirek et al., 2015] Tischbirek, C., Birkner, A., Jia, H., Sakmann, B., and Konnerth, A. (2015). Deep two-photon brain imaging with a red-shifted fluorometric Ca ¡sup¿2+¡/sup¿ indicator. *Proceedings of the National Academy of Sciences*, 112(36):11377–11382.

[Tomer et al., 2014] Tomer, R., Ye, L., Hsueh, B., and Deisseroth, K. (2014). Advanced CLARITY for rapid and high-resolution imaging of intact tissues. *Nature Protocols*, 9(7):1682–1697.

[Tonegawa et al., 2015] Tonegawa, S., Liu, X., Ramirez, S., and Redondo, R. (2015). Memory Engram Cells Have Come of Age.

[Toni et al., 2008] Toni, N., Laplagne, D. A., Zhao, C., Lombardi, G., Ribak, C. E., Gage, F. H., and Schinder, A. F. (2008). Neurons born in the adult dentate gyrus form functional synapses with target cells. *Nature Neuroscience*, 11(8):901–907.

[Treves et al., 2008] Treves, A., Tashiro, A., Witter, M. P., and Moser, E. I. (2008). What is the mammalian dentate gyrus good for? *Neuroscience*, 154(4):1155–1172.

[Tsien et al., 1985] Tsien, R. Y., Rink, T. J., and Poenie, M. (1985). Measurement of cytosolic free Ca2+ in individual small cells using fluorescence microscopy with dual excitation wavelengths. *Cell calcium*, 6(1-2):145–157.

[van Groen et al., 2003] van Groen, T., Miettinen, P., and Kadish, I. (2003). The entorhinal cortex of the mouse: Organization of the projection to the hippocampal formation.

[Vogelstein et al., 2009] Vogelstein, J. T., Watson, B. O., Packer, A. M., Yuste, R., Jedynak, B., and Paninskik, L. (2009). Spike inference from calcium imaging using sequential Monte Carlo methods. *Biophysical Journal*, 97(2):636–655.

[Wang et al., 2015] Wang, G., Wyskiel, D. R., Yang, W., Wang, Y., Milbern, L. C., Lalanne, T., Jiang, X., Shen, Y., Sun, Q.-Q., and Zhu, J. J. (2015). An optogenetics- and imaging-assisted simultaneous multiple patch-clamp recording system for decoding complex neural circuits. *Nat Protoc*, 10(3):397–412.

[Welkenhuysen et al., 2016] Welkenhuysen, M., Hoffman, L., Luo, Z., De Proft, A., Van den Haute, C., Baekelandt, V., Debyser, Z., Gielen, G., Puers, R., and Braeken, D. (2016). An integrated multi-electrode-optrode array for in vitro optogenetics. *Sci Rep*, 6:20353.

[West and Gundersen, 1990] West, M. J. and Gundersen, H. J. G. (1990). Unbiased stereological estimation of the number of neurons in the human hippocampus. *Journal of Comparative Neurology*, 296(1):1–22.

[Wilt et al., 2013] Wilt, B. A., Fitzgerald, J. E., and Schnitzer, M. J. (2013). Photon shot noise limits on optical detection of neuronal spikes and estimation of spike timing. *Biophysical Journal*, 104(1):51–62.

[Witter, 2007] Witter, M. P. (2007). The perforant path: projections from the entorhinal cortex to the dentate gyrus. *Progress in Brain Research*, 163:43–61.

[Witter et al., 1989] Witter, M. P., Groenewegen, H. J., Lopes da Silva, F. H., and Lohman, A. H. M. (1989). Functional organization of the extrinsic and intrinsic circuitry of the parahippocampal region. *Progress in Neurobiology*, 33(3):161–253.

[Wokosin et al., 2004] Wokosin, D. L., Loughrey, C. M., and Smith, G. L. (2004). Characterization of a range of fura dyes with two-photon excitation. *Biophysical journal*, 86(3):1726–1738.

[Yu et al., 2013] Yu, E. P., Dengler, C. G., Frausto, S. F., Putt, M. E., Yue, C., Takano, H., and Coulter, D. A. (2013). Protracted postnatal development of sparse, specific dentate granule cell activation in the mouse hippocampus. *The Journal of neuroscience : the official journal of the Society for Neuroscience*, 33(7):2947–2960.

[Zorlutuna et al., 2011] Zorlutuna, P., Jeong, J. H., Kong, H., and Bashir, R. (2011). Stereolithography-based hydrogel microenvironments to examine cellular interactions. *Advanced Functional Materials*, 21(19):3642–3651.

[Zylberberg et al., 2016] Zylberberg, J., Hyde, R. A., and Strowbridge, B. W. (2016). Dynamics of robust pattern separability in the hippocampal dentate gyrus. *Hippocampus*, 26(5):623–632.